Modeling of Turbulent Sooting Flames

by

Shao Teng Chong

A dissertation submitted in partial fulfillment
of the requirements for the degree of
Doctor of Philosophy
(Mechanical Engineering)
in The University of Michigan
2018

Doctoral Committee:

Professor Venkat Raman (Chair)
Assistant Professor Jesse Capecelatro
Assistant Professor Mirko Gamba
Professor Katsuo Kurabayashi

"If I have seen further it is by standing on the shoulders of giants" - *Isaac Newton*

ACKNOWLEDGEMENTS

I would like to express my utmost gratitude to my thesis advisor, Prof. Venkat Raman for his support, guidance, mentorship, patience, and advice during this journey. I could not have had a better advisor for this journey. I also wish to dedicate a special thanks to Prof. Michael Mueller (Princeton University) and Prof. Hong G. Im (King Abdullah University of Science and Technology) for their support, discussions and reviews. This journey would have been less fruitful and interesting without their collaboration. I also would like to thank my thesis committee members, Prof. Katsuo Kurabayashi, Prof. Jesse Capecelatro, and Prof. Mirko Gamba for their helpful comments and suggestions on this thesis.

Any doctoral experience would be incomplete without their fellow graduate students. I would like to thank each and every lab member in the Advanced Propulsion Concepts Lab for the shared experiences, especially Heeseok Koo, Malik Hassanaly, Wang Han, Yihao Tang and Stephen Voelkel for their support during the early years.

I also wish to thank my family for their encouragement and patience through this endeavour. A special thanks to Sudarat Lee for her support, love and partnership throughout this period.

Last but not least, I would like to acknowledge the financial support from National Aeronautics and Space Administration (NASA), Clean Combustion Research Center (CCRC) in King Abdullah University of Science and Technology (KAUST), Department of Mechanical Engineering and Department of Aerospace Engineering in the University of Michigan.

TABLE OF CONTENTS

CHAPTER

LIST OF FIGURES

LIST OF TABLES

ABSTRACT

Modeling multiphase particles in turbulent fluid environment is a challenging task. To accurately describe the size distribution, a large number of scalars need to be transported at each time-step. Add to that the heat release and species mass fraction changes from nonlinear combustion chemistry reactions, and you have a tightly coupled set of equations that describe the (i) turbulence, (ii) chemistry, and (iii) soot particle interactions (physical agglomeration and surface chemistry reactions). Uncertainty in any one of these models will inadvertently introduce errors of up to a few orders of magnitude in predicted soot quantities. The objective of this thesis is to investigate the effect of turbulence and chemistry on soot evolution with respect to different soot aerosol models and to develop accurate models for simulating soot evolution in aircraft combustors. To investigate the effect of small scale turbulence time-scales on soot evolution, a partially-stirred reactor (PaSR) configuration is used and coupled with soot models from semi-empirical to detailed statistical models. Differences in soot property predictions including soot particle diameter and number density among the soot models are highlighted. The soot models will then be used to simulate the turbulent sooting flame in an aircraft swirl combustor to determine the large scale soot-turbulence-chemistry interactions. Highlights of this study include the differences in location of bulk soot mass production in the combustor using different soot models. A realistic aircraft combustor operating condition is simulated using a state-of-the-art minimally dissipative turbulent combustion solver and soot method of moments to investigate pressure scaling and soot evolution in different operating conditions. A separate hydrodynamic scaling is introduced to the pressure scaling, in addition to thermochemical scaling from previous studies. Finally, a Fourier analysis of soot evolution in the combustor will be discussed. A lower sooting frequency mode is found in the combustor, separate from the dominant fluid flow frequency mode that could affect statistical data collection for soot properties in turbulent sooting flame simulations.

CHAPTER I

Introduction

1.1 Motivation

Soot, or more commonly recognized as the black smoke emitted from vehicle tail pipe, is composed of carbon particles of different mass, sizes, and fractal dimensions. It is the product of incomplete combustion between hydrocarbon fuels and oxygen and represents combustion inefficiency from an engineering standpoint. Sources of soot varies from candle flame and bunsen burner to medium scale combustion devices like internal combustion engines to large scale gas turbine combustors to natural phenomena like forest fires. Effects of soot are largely undesirable. Besides producing smog that impairs vision and decreasing fuel efficiency in combustion devices, recent health studies (*Donaldson et al.* (2005); *Lighty et al.* (2000)) have found high correlations between size of soot particles and lung cancer. Due to these environmental and health concerns, emissions of soot and any aerosol particulates from automobile and aircraft engines are regulated by the government. As the health effects are increasingly being highlighted, tighter control has been imposed on the size of particles emitted from these combustion devices e.g. the European Environment Agency has imposed more stringent laws over the years on PM2.5 (sub 2.5 μm fine particles) particulate matters, soot included (*UNION et al.* (2008)). Thus, it has become increasingly important to not only be able to identify efficient combustion and design combustion devices to operate at these conditions, but to be able to design these engineering devices soon.

To realize these future low emission combustion devices, the use of simulation in accurately predicting soot and in reducing design turnover time is evident. And to achieve that, high fidelity models will be required. The three most important models consist of turbulence model to predict the flow field, combustion model to predict the change in thermodynamic properties, and soot model to predict the particle size distribution. Despite rapid parallel development in each of these fields, the current models are not consistent enough in predicting soot in turbulent flames, especially in the important domain of predicting soot particle sizes and number density. In a recent Sandia target flame (*Zhang et al.* (2011)) burning pure ethylene and air, it is shown how sensitive soot prediction is to changes in model (isf (2016)).

The objective of this dissertation is to develop high-fidelity soot models that will contribute to the simulation and understanding of soot evolution in an aircraft swirl combustor. To that end, more exhaustive studies are required in the fields of soot modeling, the interactions between soot, chemistry, and turbulence, and the understanding of how soot evolves in an aircraft combustor. The author has developed a soot model, done comparative analysis on different soot models, and from realistic simulations, contributed to the deeper understanding of soot evolution in an aircraft combustor.

1.2 State of the Art in Modeling Soot

Soot modeling has blossomed circa 1980s and has continued to develop from semi-empirical model consisting of simple chemical kinetic rates to numerical simulation of particle bin sizes to Monte Carlo stochastic simulations to the widely used method of moments flavors of today. Although the models differ by methodology, rate of reactions, computational expense, ease of implementation, and ultimately the predicted soot properties, the cornerstone of soot evolution from the small particles to larger particles and their chemical processes are fundamentally the same.

Figure 1.1 shows this soot evolution in a simple turbulent non-premixed jet flame. Soot nuclei is assumed to be incepted from precursor species wherein there are two schools of thinking: (i) collision of two Polycyclic Aromatic Hydrocarbons (PAH) dimers (*Schuetz and Frenklach* (2002)), or (ii) formed from acetylene species directly into soot carbon particles (*Harris and Weiner* (1983)). These soot nuclei then goes through multiple chemical and physical processes that either grow into larger particles or destroyed through oxidation. There are multiple processes to grow into larger particles: condensation of PAH species onto the soot nuclei surface, chemical addition of acetylene (C_2H_2) to the surface of the nuclei via H-abstraction, C_2H_2 addition (HACA) reaction (*Frenklach and Wang* (1991b)), and via coagulation and agglomeration of smaller particles into larger particles.

The following subsections describe the most important components required to model soot evolution including the combustion mechanism, soot precursor model, soot nanoparticle evolution formulation, and soot chemistry description. These components are sufficient for a simple 0-D flame but ultimately need more complex turbulent combustion models to simulate a large scale turbulent sooting flame. The turbulent combustion modeling formulations will be discussed in detail in Section 1.3 and Section 1.4.

1.2.1 Gas Phase Combustion

Soot formation starts from the combustion process and this thesis will cover only the gas-phase combustion although solid (coal) and droplet (liquid hydrocarbon fuel) combustion are also common sources of soot formation.

In the field of combustion, gas phase combustion kinetic mechanisms govern the thermodynamic properties of the simulation. Prior to soot formation, following the structure of Fig. 1.1, formation of precursor species like acetylene and PAHs, as well

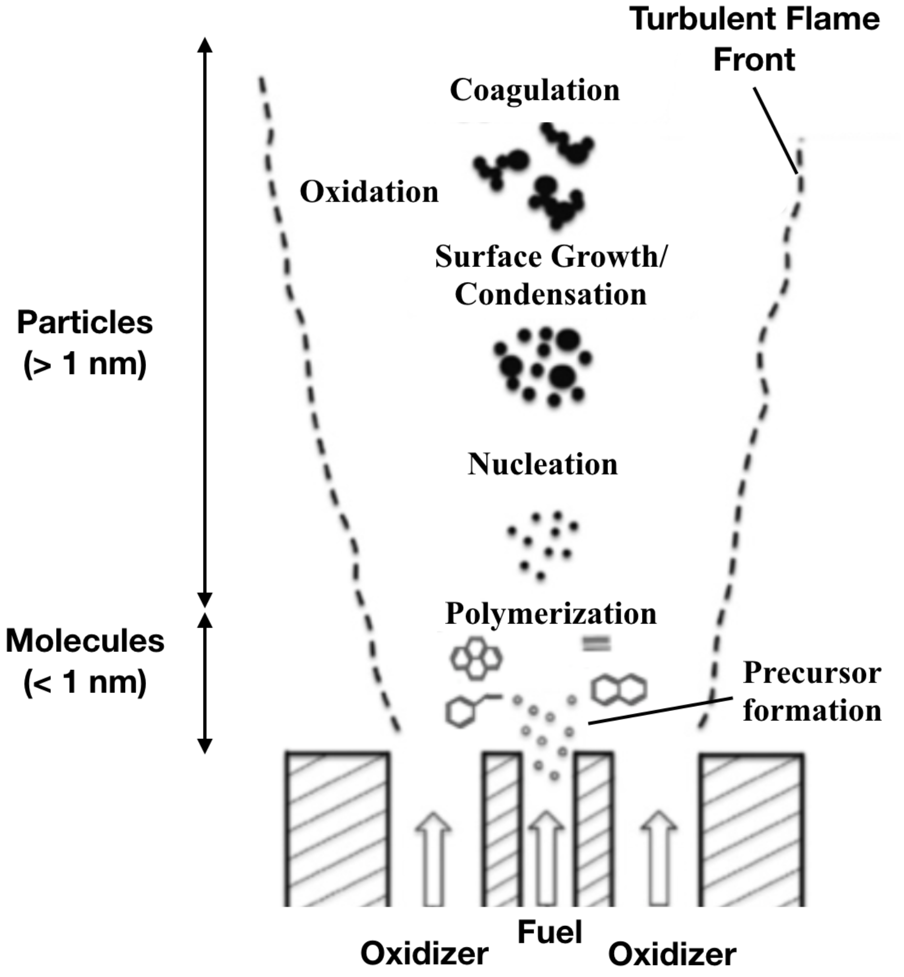

Figure 1.1: Evolution of soot in a turbulent sooting flame from formation of presursors like acetylene (C_2H_2) and PAHs to large agglomerated particles. Oxidation reaction runs parallel to the other growth reactions in shrinking particle size and ultimately in completely oxidizing the particles to combustion gaseous products. Figure adapted from *Sung* (2011).

as oxidation agents like O_2 and OH radicals are described by the kinetic rates in the mechanism used. Further, temperature is also determined by the species composition and its enthalpy computed directly from chemical mechanisms. *Mueller and Raman* (2014) have shown that small errors in temperature mismatch with experiments can lead to significant errors in soot predictions.

The fuels used in aircraft engines and automobile vehicles consist of a multitude of molecular components. Among these species are linear alkanes (n-heptane, C_7H_{16}), branched alkanes (iso-octane, C_8H_{19}), aromatics (benzene, C_6H_6), toluene (C_7H_8), and naphthalene (C_8H_{10}). Mapping the reaction mechanism of all these species down to common combustion products like CO_2 and H_2O is very challenging because the entire decomposition pathway for every component is not yet fully known. As such, typical fuels are represented by surrogates (*Zhang et al.* (2007)). Simple blends of these species are used in the mechanism to reproduce certain physical properties like distillation curve and density and thermochemical properties like ignition delay, laminar flame speed, temperature and species profiles. Despite a collection of existing combustion mechanisms *Smith et al.* (2012); *Wang et al.* (2007), one of the earliest mechanism developed for soot precursor species prediction is by *Blanquart et al.* (2009). This mechanism covers the decomposition of methane and ethylene to larger hydrocarbon surrogates like n-heptane, iso-octane, benzene and toluene for high temperature premixed and diffusion flames. The mechanism is also supplemented with pathways for the formation of PAH up to cyclo[cd]pyrene, important precursor species for the formation of soot. In comparisons with laminar premixed and counterflow diffusion flames, the main species and soot precursors all compare favorably with experimental data although more data on aromatic species could be useful in further validating the mechanism. The extended work on investigating the aromatic species is performed by *Narayanaswamy et al.* (2010). Revised reaction rates for substituted aromatics such as toluene and m-xylene are taken from literature data or derived from lower aromatics. Although this detailed mechanism is validated against plug flow reactor data, ignition delay times, shock tubes, and laminar flame velocities, more validation of overall soot precursor species profile such that performed in *Blanquart et al.* (2009) is warranted to assess the performance of the mechanism after the changes to the aromatic species oxidation rates. This mechanism has been used in a multitude of computational studies *Mueller et al.* (2013); *Deng et al.* (2017); *Mueller and Pitsch* (2013, 2012) and has produced good quantitative comparisons with experimental data from jet flames to large scale combustors.

More recently, *Metcalfe et al.* (2013) studied the oxidation of smaller hydrocarbons species (C_1 to C_2) through critical evaluation of literature rates, with minimum tuning or optimization performed. The study uses original experimentally measured values or high-level theoretical molecular dynamics calculations. The mechanism has been validated across a wide range of conditions and devices such as flow reactor, shock tube, jet-stirred reactor, and laminar flame studies. Detailed comparisons with available literature mechanisms like GRI-Mech (*Smith et al.* (2012)) and San Diego mech (san (2011)) are also performed. Using this mechanism, *Selvaraj et al.* (2016) studied the sensitivity of soot formation to various chemical pathways for large PAHs in an ethylene-air premixed sooting flame and found good agreement with experimental data for soot profiles. It was also found that the nucleation process is very sensitive to choice of PAH precursors and the consideration of larger PAHs beyond pyrene is critical for accurate prediction of soot formation.

In this dissertation, these existing kinetic mechanisms are used directly in the simulations without alteration to study the chemistry and thermodynamical effects on soot formation and oxidation.

1.2.2 Soot Precursor Description

After describing the combustion modeling that determines the thermodynamics and species mass fractions in the domain, soot nuclei inception is mainly described based on either (i) acetylene-based or (ii) PAH-based models. The choice of model has a significant effect on soot formation. The acetylene-based model was first developed by *Leung et al.* (1991) where acetylene (C_2H_2) is the prime indicate species for soot formation. Soot nuclei is assumed to form at a size of 100 carbon atoms from acetylene molecules. Comparisons with the counterflow diffusion flame experimental data of *Vandsburger et al.* (1984) is good but generated a lot of questions about the suitability of using acetylene species as precursor. Further, the soot number density prediction is less satisfactory although soot volume fraction is predicted relatively well in each cases. The acetylene-based model also predicts worse soot volume fraction for more oxygen-enriched flames. Parallel experimental studies by *Smyth et al.* (1985) at the time also cast light on the suitability of acetylene where they found soot inception zone occurring at high temperature edge of a region with high concentration of PAHs.

Later studies by *Schuetz and Frenklach* (2002) investigated the binary collision of pyrene molecules (dimerization process) using molecular dynamics (MD) at 1600 K, within the temperature for soot nucleation in most flames and found that the lifetimes and collisional frequency were physically possible and a development of the internal rotor between the two pyrene molecules stabilizes the forming dimer. This study fundamentally extends the view that aromatic dimers formed from PAH species can survive long enough to evolve into soot nuclei particles. The first modeling of a jet flame using this PAH description was *Frenklach and Wang* (1991a) where the full model from fuel pyrolysis to PAH formation to planar growth, coagulation, surface growth and oxidation following that of Fig. 1.1 was developed. When experimental temperature profiles were imposed on the simulation of ethylene-O_2-argon flame, good comparison with experimental data is found for soot number density and particle diameter, previously not seen in the acetylene-based models.

1.2.3 Soot Nanoparticle Physical Description

From the particle size distribution (PSD) point of view, these soot particles range from the small nuclei (often spherical in size) to moderate sized particles that went through mass addition to large fractal particles of tens of micrometers. To ascribe a variable such as volume or mass to track the size and describe these fractal patterns is not accurate. Another bivariate parameter such as surface area (*Blanquart and Pitsch* (2009b)) is typically needed to describe the non-linear relationship between volume and surface area.

From early experimental measurements (*Zhao et al.* (2005)) using the scanning mobility particle sizer (SMPS), the soot particle size distribution function (PSDF) or number density function (NDF) is often bimodal. The first mode consists of small particles of size close to the incepted soot nuclei. This first mode can be thought of as the direct consequence of nucleation from PAH or C_2H_2. The second mode is the larger particles formed from mass addition reactions on the first mode or coagulation of particles of different sizes to form large fractal agglomerates. This important observation can simplify soot modeling greatly if assumptions were to be made about the general distribution of soot for all flames.

The evolution of soot NDF is theoretically described by the Population Balance Equation (PBE) from *Friedlander* (2000) (Chapter 11, Eq. 11.4) shown in Eq. 1.1.

$$\frac{dN_i}{dt} + \frac{du_k N_i}{dx_k} = \frac{d}{dx_k}\big(0.55\frac{\nu}{T}\frac{dT}{dx_k}N_i\big) + \frac{dN_{coag}}{dt} + \frac{dN_{grow}}{dt} - \frac{dN_{ox}}{dt} \tag{1.1}$$

It is an evolution of the Smoluchowski coagulation equation (*Von Smoluchowski* (1917)) that takes into account the time and position through the general convective diffusion equation. The left hand side terms are the time and space (convection) evolution of the NDF for particle size i. The terms on the right are the thermophoresis term, coagulation source term, growth source term and oxidation sink term respectively. These terms will be described in detail in Section 1.2.4. Particle diffusion is neglected due to the high Schmidt number assumption for the large soot particles in this dissertation. The process that increases the dimensionality of the PBE is particle coagulation described in Eq. 1.2 for particle i.

$$\frac{dN_{coag}}{dt} = \frac{1}{2}\sum_{j=1}^{i-1} \beta_{j,i-j} N_j N_{i-j} - \sum_{j=1}^{\infty} \beta_{i,j} N_i N_j \tag{1.2}$$

where $i = 2 \rightarrow \infty$. The first term on the right hand side is the formation of the particle sized i from the coalescence of particle j and particle $i-j$ while the second term is the sink term due to collision with other particles of size $j = 1$ to ∞ to form other particle sizes. A physically realistic dependence of the collision coefficient, β on all the ranges of particle sizes makes it impossible to obtain a closed form solution. To obtain an approximation to the PBE (without transporting every size range in the PSD), multiple strategies have been developed but most of them revolve around the field of statistical modeling.

The most intuitive model is the sectional method (*Gelbard and Seinfeld* (1980); *Hall et al.* (1997)) where the particles are discretized into a range of bin sizes and the number of particles in each bin is tracked and solved for. Essentially, N_i in Eq. 1.1 represents a discrete logarithmic range in the PSDF and a source term for each size range is derived from nucleation, surface growth, and coagulation. Accuracy of this method is dependent on a number of factors like the range of size each bin represents (number of bins in a fixed size range) and methods for dealing with particle aggregation (*Smooke et al.* (2005)). Further, the exponential increase in computational cost for the use of more than one variable to track the NDF is prohibitive and unfeasible for large scale simulations.

The second model is the Monte Carlo (MC) method (*Balthasar and Kraft* (2003)), a stochastic model used widely in the field of optimization but has received support in the field of aerosol science for its ability to converge to the exact PBE at large number of soot particles used (N), and to simulate systems with large number of coupled degrees of freedom. Thus, MC method can be used for multivariate NDF descriptions without significantly increasing the computational cost. Subsequently, MC is the most accurate method so far to obtain soot NDF. However, the fundamental cost for a stochastic simulation is already higher than that of sectional method and the other methods discussed below. In MC method, the first step is to calculate the rates of different particle events i.e. inception, coagulation, condensation, surface growth and oxidation. Using these rates, the size of the individual time steps or the waiting time is determined according to an exponentially distributed random variable. One of the events is chosen probabilistically relative to their rates. Depending on which of the events has been selected, the appropriate number of particles needed to perform this event is chosen according to the particles individual rates. State of the particle system is updated and a new timestep is determined. The cycle is repeated until the final simulation time. Depending on the number of notional particles used and N, the cost for MC can get prohibitive very quickly. Also, MC is known to be difficult to be coupled to gas phase chemistry (*Celnik et al.* (2007)) (no sink term in gas phase for species consumed). Thus, MC method is so far limited to 0-D and 1-D flames for model validation purposes.

1.2.3.1 Semi-empirical model (SEMI)

The third model is the semi-empirical model (*Tesner et al.* (1971)), which is one of the earliest and simplest method for simulating soot. One of the earliest and most widely-used model (*Leung et al.* (1991)) transports two additional equations for soot mass fraction and soot number density. Closure for these two equations are obtained from four chemical reaction rates describing the nucleation, surface growth, oxidation, and agglomeration. Although the ease of implementation and low computational cost is very attractive as a first approximation for any turbulent sooting flame simulation, a few assumptions are too simplified e.g. inception species, spherical particle shape, surface growth dependence on square root of surface area, and soot oxidation only reduces particle size but not the number density directly.

SEMI method makes general assumptions about soot particle shape, precursor species and surface area in modeling soot formation. Firstly, SEMI model assumes that soot particles are spherical. Secondly, acetylene (C_2H_2) species is the soot precursor directly forming the incipient soot. Thirdly, the number of active sites on the soot particle is proportional to the square root of the total surface area available. Lastly, O_2 is the only species responsible for oxidizing soot particle, as opposed to OH and other radicals being used in the detailed model below, and that soot oxidation does not affect soot particle number density directly.

Two additional transport equations are needed for the SEMI method: (i) soot (solid carbon) mass fraction, Y_i (Eq. 1.3), and (ii) soot particle number density, N (Eq. 1.4).

$$\frac{dY_i}{dt} + \frac{du_k Y_i}{dx_k} = \frac{d}{dx_k}\big(0.55\frac{\nu}{T}\frac{dT}{dx_k}Y_i\big) + \frac{dY_{growth}}{dt} - \frac{dY_{ox}}{dt} \tag{1.3}$$

$$\frac{dN}{dt} + \frac{du_k N}{dx_k} = \frac{d}{dx_k}\big(0.55\frac{\nu}{T}\frac{dT}{dx_k}N\big) + \frac{dN_{nucl}}{dt} - \frac{dN_{agg}}{dt} \tag{1.4}$$

where oxidation is assumed to affect only the soot mass fraction, not the number density so soot burnout of the smallest soot particles is not modeled in this method. The only number density sink term is via agglomeration which is modeled by normal square dependence (*Leung et al.* (1991)).

Source terms describing soot mass increase/depletion are described by the nucleation term (Eq. 1.5), surface growth term (Eq. 1.6), and the oxidation term (Eq. 1.7), while source terms for particle number density is described by the agglomeration term

(Eq. 1.8). The authors are aware of the amount of parameter tuning required for this model to more accurately describe soot formation but the purpose of this paper is to study the prediction of existing soot models, thus the reaction rate source term formulations and rate constants are used as is from the original paper (*Leung et al.* (1991)).

$$C_2H_2 \rightarrow 2C(s) + H_2 \tag{1.5}$$

$$C_2H_2 + nC(s) \rightarrow (n+2)C(s) + H_2 \tag{1.6}$$

$$C(s) + \frac{1}{2}O_2 \rightarrow CO \tag{1.7}$$

$$nC(s) \rightarrow C_n(s) \tag{1.8}$$

1.2.3.2 Method of Moments

The fourth model is the Method of Moment (MOM). In MOM, the NDF (N_i in Eq. 1.1) is summarized into a moment form (Eq. 1.9) and the moments solved for (*Frenklach and Harrris* (1986)).

$$M_x = \sum_{i=0}^{\infty} w_i \xi_i^x \tag{1.9}$$

where w is the weight, ξ is the abscissa of the moments, and x is the order of the moment. In modeling the PSD of soot, w is the number density of the distribution while ξ is the tracked coordinates like volume, surface area and number of activated H-sites. These tracked coordinates increase the dimensionality of the moment equation and increases the number of moments transported. The number of moment order determines the accuracy of the model with higher orders being more accurate. This is analogous to tracking more discrete particle sizes. However, for this dissertation, the highest order tracked is order two ($x = 2$). This assumption is supported by the fact that soot PSD is bimodal. Due to the nature of moment method, the full NDF is lost during the moment transport. In principle, knowledge of all the moments is equivalent to knowing the NDF itself but in most practical applications, the properties one considers are fully determined by just the first few moments. This makes MOM the most efficient and feasible approach for coupling with 3-D complex simulations.

During a simulation, the moments, M_x are transported along with the velocity and scalars according to Eq 1.10.

$$\frac{dM_x}{dt} + \frac{du_k M_x}{dx_k} = \frac{d}{dx_k}\big(0.55\frac{\nu}{T}\frac{dT}{dx_k}M_x\big) + \dot{M}_x \tag{1.10}$$

where $\dot{M}_x$ is the moment source term for soot processes described in Section 1.2.4 below. It's general formulation is shown in Eq. 1.11.

$$\dot{M}_x = \sum_{i=0}^{\infty} \dot{w}_i \xi_i^x \tag{1.11}$$

The mathematical difficulty of the method of moments lies in obtaining closure of the moment source terms, $\dot{M}_x$. The source terms depend on a larger set of moments than that is transported. For example, in the coagulation source term, $\dot{M}_{coag}$, there exists fractional order moments derived from the collisional frequency term, $\beta_{i,j}$ which cannot be expressed in terms of sums and products of transported moments. To obtain closure, several methods have been developed including the Method of Moments with Interpolative Closure (MOMIC) and the Quadrature Method of Moments (QMOM) variants that directly tracks the weights and abscissas of the moments. The bimodal soot distribution has made QMOM a feasible and attractive method due to its intuitive nature of tracking the peaks in the NDF. However, the moment inversion to obtain the weights and absicssas can be resource intensive. The different variants of QMOM includes Direct Quadrature Method of Moments (DQMOM), Hybrid Method of Moments (HMOM), Extended Quadrature Method of Moments (EQMOM) and Extended Conditional Quadrature Method of Moments (ECQMOM). Each method has its own moment closure strategy described below.

All the soot particle dynamics model implemented in this study follows the bivariate joint Volume-Surface (VS) description by *Mueller et al.* (2009) shown in Eq. 1.12.

$$M_{x,y} = \sum_i N_i V_i^x S_i^y \tag{1.12}$$

where N, V, and S are the number density, volume, and surface area respectively. x and y are the order of moment, M, for volume and surface area respectively.

1.2.3.3 Method of Moments with Interpolative Closure (MOMIC)

MOMIC (*Frenklach* (2002)) is the earliest MOM closure method developed based on closure by logarithmic interpolation from the whole-order moments (available at each integration step) for the fractional order moments introduced by the non-additive nature of the collision coefficient term. Higher accuracy is obtained by separating the interpolation of positive order and negative order moments. The primary advantage of MOMIC is its numerical economy. Also, the present formulation of MOMIC cannot handle rigorously particle oxidation (when surface oxidation is at the verge of removing all particle material).

For the Method of Moments with Interpolative Closure (MOMIC) (*Frenklach* (2002); *Frenklach and Harrris* (1986)), the fractional-order moments (resulting mostly from coagulation β coefficients) are computed from polynomial interpolation of the logarithm of whole-order moments transported at each timestep as shown in Eq. 1.13.

$$M_{x,y} = exp\left(\sum_{r=0}^{R}\sum_{k=0}^{r} a_{r,k}x^k y^{r-k}\right) \tag{1.13}$$

where R is the order of polynomial interpolation, where for this study, is a constant at $R = 2$, similar to most realistic 3D simulations, for the best balance between computational expense and model accuracy. $a_{r,k}$ are constants determined from the set of known moments and inversion of the linear system. For further details of bivaraite MOMIC and its source term formulations, the reader is referred to the original article (*Mueller et al.* (2009)). The set of moments used for this study are: $M_{0,0}$, $M_{1,0}$, $M_{0,1}$, $M_{2,0}$, $M_{1,1}$, $M_{0,2}$.

1.2.3.4 Direct Quadrature Method of Moments (DQMOM)

In DQMOM (*Marchisio and Fox* (2005)), the weight and abscissas (e.g. volume, surface area) of the delta functions are directly transported, unlike MOMIC or the traditional QMOM (*McGraw* (1997)) where the moments are transported. There is a resource intensive matrix inversion involved in DQMOM, using Produce-Difference Algorithm, to obtain the source terms for the weights and abscissas from the moment source terms. The matrix system is ill-conditioned if any two of the delta functions (location of abscissas) are situated close to each other. This is common in flames where most of the cell domains have little to no soot. Thus, DQMOM is resource intensive but the most accurate of QMOM methods for transporting the delta functions directly. Further, the choice of the set of moments that generate the linear system is nontrivial and affects both accuracy and stability of the code. In general, the higher is the order of the moments, the stiffer is the solution of the linear system. One should avoid to include higher-order moments that do not need to be known with high-accuracy (*Zucca et al.* (2007))

The formulation for DQMOM is naturally different from previous MOMIC equation, as shown in Eq. 1.14.

$$M_{x,y} = \sum_i \omega_i V_i^x S_i^y \tag{1.14}$$

where ω is the weight of the delta function and V and S are abscissas/locations of the delta function (for volume and surface area respectively). In this study, the total number of delta functions, $i = 2$. In DQMOM, the weights and abscissas are solved for directly. Source terms for these weights and abscissas are inverted from moment source terms. However, depending on the set of moments used, the linear system can be ill-conditioned and depending on the matrix condition number, inaccuracies will also result even if the matrix can be inverted as mentioned previously. The optimized set of moments used for this study are as follows: $M_{0,0}$, $M_{1,0}$, $M_{0,1}$, $M_{1/3,0}$, $M_{2/3,0}$, $M_{0,1/2}$.

1.2.3.5 Hybrid Method of Moments (HMOM)

In order to take advantage of the numerical efficiency of MOMIC and to properly handle nuclei mode oxidation, HMOM (*Mueller et al.* (2009); *Mueller* (2012)) is introduced where a delta function is fixed at the nuclei mode (location of abscissas known) and the rest of the NDF approximated via interpolative closure. A total of n MOMIC moments + 1 weight of the first nuclei mode is transported. The computational cost increase over MOMIC is minimal but increases the accuracy of soot prediction from accurate oxidation of nuclei particles and implementation of fragmentation term.

The modified moment equation is given by Eq. 1.15.

$$M_{x,y} = \omega_0 V_0^x S_0^y + exp\left(\sum_{r=0}^{R} \sum_{k=0}^{r} a_{r,k} x^k y^{r-k} \right) \tag{1.15}$$

where ω_0, V_0, and S_0 are the weight of the delta function, volume of nucleated particle, and surface area of nucleated particle respectively. As closure to this model, an additional equation is solved for ω_0 in addition to 6 moments for the larger particles: $M_{0,0}$, $M_{1,0}$, $M_{0,1}$, $M_{2,0}$, $M_{1,1}$, $M_{0,2}$.

1.2.3.6 Conditional Quadrature Method of Moments (CQMOM)

In CQMOM (*Yuan and Fox* (2011)), the NDF is approximated by a set of Dirac delta functions but the surface area, S, is conditioned on the volume, V . This method has demonstrated higher accuracy in predicting surface area change from sintering process in the downstream *Sung et al.* (2014); *Sung* (2011). Further, the computational expense of transporting more delta functions (higher accuracy) is reduced as the number of moments does not increase linearly with the number of delta functions. CQMOM also has the advantage of less ambiguous choice of moments compared to DQMOM. This method is developed for soot in this study and it's evolution compared to other method of moments will be highlighted.

CQMOM formulation is similar to DQMOM but with an additional condition for surface area as shown in Eq. 1.16.

$$M_{x,y} = \sum_{i=1}^{Nv} \sum_{j=1}^{Na} \omega_i \omega_{ij} V_i^x S_{ij}^y \tag{1.16}$$

where Nv and Na are number of volume and surface area nodes respectively. For this study, $Nv = 2$ and $Na = 1$ for a direct comparison with DQMOM. CQMOM has an advantage in terms of the simplicity of its matrix inverse and thus does not pose difficulties in convergence like in DQMOM. The set of moments used for this study are: $M_{0,0}$, $M_{1,0}$, $M_{2,0}$, $M_{3,0}$, $M_{0,1}$, $M_{1,1}$.

1.2.3.7 Extended Quadrature Method of Moments (EQMOM)

In EQMOM (*Yuan et al.* (2012)), the moment equations are closed by reconstructing the soot NDF with a superposition of continuous kernel functions. Instead of the delta functions used in DQMOM, EQMOM uses a continuous kernel function. The moment inversion then consists of finding the non-negative weights and abscissas of the kernel functions and their shape parameter. EQMOM has shown to be able to treat particle removal by oxidation and predicts particle number density accurately using a gamma kernel function (*Wick et al.* (2017a)).

EQMOM formulation follows that of QMOM-based methods but substitutes the delta functions with continuous kernel functions as shown in Eq. 1.17.

$$M_x = \sum_i \omega_i V_i^x exp\Big(\frac{1}{2}k^2\sigma^2\Big) \tag{1.17}$$

the exponential term represents just one of several viable continuous kernel functions where in this case uses a lognormal kernel function with coefficients $exp(1/2k^2\sigma^2)$.

1.2.3.8 Extended Conditional Quadrature Method of Moments (ECQMOM)

ECQMOM (*Salenbauch et al.* (2015)) is the latest QMOM variant that efficiently captures the whole PSD and models the formation of aggregates accurately, taking advantage of CQMOM that is developed for modeling sooting flame specifically in this thesis. ECQMOM is also able to treat particle removal by oxidation and thus predicts better number density of the nuclei mode.

ECQMOM formulation follows mostly that of CQMOM but with the substituted kernel function for the volume abscissa as shown in 1.18.

$$M_{x,y} = \sum_{i=1}^{Nv} \sum_{j=1}^{Na} \omega_i \omega_{ij} m_{V,x}^i S_{ij}^y \tag{1.18}$$

where $m_{V,x}^i$ is the moment that represents the continuous kernel function describing the distribution of volume node. Similar to EQMOM, multiple kernel functions are possible as described in *Wick et al.* (2017a); *Salenbauch et al.* (2015).

1.2.4 Soot Chemistry Description

The description of soot mass addition and morphological evolution processes and its source term formulation are described below for the method of moment models. These models are mostly from soot method-of-moment seminal studies of *Blanquart and Pitsch* (2009a,b); *Mueller* (2012). The same soot chemistry descriptions below are applied to all the soot method-of-moment models in this study for accurate comparison.

1.2.4.1 Nucleation

The first particle is formed from coalescence of two PAH dimers with PAH species assumed to consist of eight species ranging from naphthalene ($C_{10}H_8$) to cyclopenta[cd]pyrene ($C_{18}H_{10}$), based on Table 1 in *Blanquart and Pitsch* (2009a). Source term for the moments is:

$$\dot{M}_{x,y}^{nucl} = \frac{1}{2}\beta_N[Dimer]^2 V_0^x S_0^y \tag{1.19}$$

where $[Dimer]$ is the dimer concentration, β_N is the dimer collision rate, V_0 is the volume of the smallest soot particle, and S_0 is the surface area of the smallest soot particle. x and y are the order of the moments for volume and surface area nodes respectively.

For HMOM, where the first node is fixed and weight of the first node transported, a slightly different source term for the weight of the first node is described below:

$$\dot{N}_0^{nucl} = \frac{1}{2}\beta_N[Dimer]^2 \tag{1.20}$$

1.2.4.2 Coagulation

Coagulation takes into account collisions in the free-molecular, transition, and continuum regimes, depending on the particle Knudsen number, Kn_i (Eq. 1.21), where λ is the mean free path of the gas molecules and d_{Ci} is the diameter of the soot particle.

$$Kn_i = \frac{\lambda}{d_{Ci}} \tag{1.21}$$

Source term for the moments is:

$$\dot{M}_{x,y}^{coag} = \frac{1}{2}\sum_{i,j=0}^{\infty} \beta_{i,j}\Big(V_{i+j}^{x}S_{i+j}^{y} - V_i^{x}S_i^{y} - V_j^{x}S_j^{y}\Big)N_iN_j \tag{1.22}$$

where $\beta_{i,j}$ describes the collision frequency of two soot particles for different regimes described in *Mueller et al.* (2009). V_{i+j} is the volume of the coagulated particle and S_{i+j} is the surface area of the coagulated particle.

When Kn_i is much larger than unity (free molecular regime), the collision frequency is determined from kinetic theory (*Harris and Kennedy* (1988)). An example of the need for a closure term in MOM is Eq. 1.23 of $\beta_{i,j}$ at free-molecular regime where K is a constant, V is volume of the colliding particles and d_C are collision diameters for fractal aggregates, described in detail in *Mueller et al.* (2009). The fractional order terms introduce difficulties to moment source term calculation because this term cannot be written in terms of moments transported.

$$\beta_{i,j} = K\big(\frac{1}{V_i} + \frac{1}{V_j}\big)^{1/2}\big(d_{C_i} + d_{C_j}\big)^2 \tag{1.23}$$

When Kn_i is much smaller than unity (continuum regime), the soot particle i is essentially ”mopping up” smaller particles, with collision of particles limited by their diffusivity. In the transition regime, a harmonic mean between the two limits is found to be a good approximation by *Kazakov and Frenklach* (1998).

For HMOM, small particles in the first mode collide with themselves and larger particles in the second mode to produce a sink term for the weight of the first node, given below:

$$\dot{N}_0^{coag} = -\sum_{i=0}^{\infty} \beta_{i,0} N_i N_0 \tag{1.24}$$

Several collision models are available that describes the evolution of surface area after collision. As particles of different sizes collide, the volume of the new particle is a summation between the particle volumes but the new surface area varies according to studies of *Dobbins et al.* (1998) where small particles are liquid-like spheres while larger (thus older) particles are carbonized solid aggregates incapable of shape change. Three different scenarios are possible:

- Small particle + small particle. Resulting particle is spherical and surface area is given by:

$$S_{0+0} = 144\pi^{1/3} V_0^{2/3} \tag{1.25}$$

- Small particle + large particle. Resulting particle is a coalescence of the small particle on the larger particle with new surface area given by:

$$S_{i+0} = S_i + \delta S \tag{1.26}$$

- Large particle + large particle. Resulting particle is pure aggregation of one particle with the other and new surface area is given by simple summation of the two surface areas.

1.2.4.3 Condensation

Condensation is modeled mainly from PAH dimer collision with soot particles, assuming PAH dimers are at least a factor two smaller than soot particles. Source term for the moments is:

$$\dot{M}_{x,y}^{cond} = \sum_{i=0}^{\infty} \beta_{Ci} \Big(x\frac{\delta V}{V_i} + y\frac{\delta S}{S_i} \Big) [Dimer] V_i^x S_i^y N_i \tag{1.27}$$

where δV is the change in volume from condensation of one PAH dimer and δS is the change in surface area from condensation, modeled from work by *Blanquart and Pitsch* (2009b). β_{Ci} is the collision coefficient of one dimer on soot particle. With competition for dimer concentration in the condensation and nucleation processes, the dimer production from gas-phase combustion is exactly balanced by dimer scavenging from nucleation and condensation.

For HMOM, condensation changes the number of particles in the first mode because of the growth in size that shifts first mode particles into the second (accumulation) mode. The sink term for the weight of the first mode is given by:

$$\dot{N}_0^{cond} = -\beta_{C0} [Dimer] N_i \tag{1.28}$$

Changes in volume from condensation also changes the surface area as condensation is assumed to make soot particles more spherical (larger particle diameter). The relationship between surface area and volume is given by a power law approximation (with fractal dimension of 1.8) shown below (*Blanquart and Pitsch* (2009b)):

$$\frac{\delta S}{S_i} = \frac{\delta V}{V_i} \Big(\frac{2}{3} n_p^{-0.2043} \Big) \tag{1.29}$$

1.2.4.4 Surface growth

Surface growth depends mainly on acetylene, C_2H_2 species concentrations based on the H-abstraction-C_2H_2-addition (HACA) mechanism (*Frenklach and Wang* (1991b)). Source term for the moments is:

$$\dot{M}_{x,y}^{sg} = \sum_{i=0}^{\infty} k_{sg}\chi\Big(x\frac{\delta V}{V_i} + y\frac{\delta S}{S_i}\Big)V_i^x S_i^{y+1} N_i \tag{1.30}$$

where k_{sg} is the surface growth rate described in more detail in 1.1 and $\chi = 1.7x10^{-19}m^{-2}$ is the constant number of active sites per unit particle area.

Reaction	A	n	Ea	Reference
$Soot - H + H \leftrightarrow Soot - * + H_2$	1.08×10^8 8.68×10^4	1.80 2.36	68.42 25.46	1/6 x *Mebel et al.* (1997)
$Soot - * + C_2H_2 \rightarrow Soot - H$	2.52×10^9	1.10	17.13	2 x *Tokmakov and Lin* (2004)

Table 1.1: Two significant HACA surface growth, k_{sg} kinetic rate reactions parameters. Kinetic reaction follows the modified Arrhenius reaction form of $k = AT^n exp(-Ea/RT)$. Units are in cm, mol, s, K and kJ. Other less prominent reactions can be found in *Blanquart and Pitsch* (2009a,b).

For HMOM, the sink term for the weight of the first node is given below:

$$\dot{N}_0^{sg} = -k_{sg}\chi N_0 S_0 \tag{1.31}$$

Both surface growth and condensation reactions are similar types of soot mass addition with changes in volume and surface area much smaller than the volume and surface area of the original particle. Changes in the surface area follows that prescribed in Eq. 1.29.

1.2.4.5 Oxidation

Oxidation is modeled based on the removal of carbon atoms (changing in particle size) by surface reaction with oxygen or hydroxyl radicals (*Neoh et al.* (1981)). It is essentially the negative form of surface reaction with its own surface reduction rates with oxygen and hydroxyl radicals. Oxidation of soot particles have been a source of contention since the removal of small particles from the population is impossible without knowing explicitly the number of soot nuclei at the first mode. Thus, the introduction of HMOM enabled the oxidation and destruction of these particles. Physically, it is assumed that soot particles are destroyed (volume and surface area) when the soot particles in the first node are oxidized. Technically, the soot particles should shrink to a negligible size before it is completely oxidized but this is an acceptable assumption since the nucleation of soot particle also started from the collision of two gas-phase dimer species. With other method of moments, the oxidation of smallest particles is neglected. The moment source term for HMOM is thus:

$$\dot{M}^{ox}_{x,y} = -k_{ox}\chi x\frac{\delta V}{V_0}V_0^x S_0^{y+1}N_0 - \sum_{i=0}^{\infty} k_{ox}\chi\Big(x\frac{\delta V}{V_i} + y\frac{\delta S}{S_i}\Big)V_i^x S_i^{y+1}N_i \tag{1.32}$$

where the first term on the right is the oxidation of small soot particles and the second term on the right is analogous to the surface growth rate but with k_{ox} as the oxidation reaction rate described in detail in *Blanquart and Pitsch* (2009b). The other methods would only include the second term on the right for oxidation model.

Reaction	A	n	Ea	Reference
$Soot-*+O_2 \rightarrow Soot-*+2CO$	2.20×10^{12}	0	31.38	*Kazakov et al.* (1995)
$Soot-H+OH \rightarrow Soot-H+CO$	Reaction probability = 0.13			*Neoh et al.* (1981)

Table 1.2: Reaction coefficients for surface oxidation in Arrhenius form of $k = AT^n exp(-Ea/RT)$. Units are in cm, mol, s, K and kJ. (*Blanquart and Pitsch* (2009b))

The source term for the weight of the first node in HMOM is modeled as the following:

$$\dot{N}_0^{ox} = -k_{ox}\chi x \frac{\delta V}{V_0} S_0 N_0 + k_{ox}\chi (S_0 + \delta S) N_1 \tag{1.33}$$

where the first term on the right is the destruction of the first mode particles and the second term is the addition to the number of particles in the first mode from oxidation of larger particles.

1.2.5 Soot-Turbulence Interaction

Turbulence affects soot both directly and indirectly. The direct way involves turbulence and eddies transporting soot into or away from flame fronts while the indirect way involves turbulence affecting the local species composition and thermodynamic properties from changing scalar dissipation rate.

The first study using Direct Numerical Simulation (DNS) to investigate the effect of transport on soot is *Lignell et al.* (2007) where a 2D nonpremixed sooting ethylene jet flame is simulated, using a multistep chemistry method and semi-empirical soot model with acetylene as inception species. The study shows how the flame curvature results in transport of soot into or away from the flame and how soot-flame breakthrough occurs when soot thermophoretic diffusion is 5-10 times lower than that of fluid convection and flame displacement velocity. *Lignell et al.* (2008) improved on the previous 2D study by simulating similar flame in 3D, due to the multidimensional effect on flame dynamics. It is found that enhanced turbulent mixing has a first order effect on soot transport toward the flame, essentially increasing soot mass as soot is transported toward the flame.

Later study of n-heptane/air nonpremixed flame by *Bisetti et al.* (2012) using more detailed PAH inception model with method of moments, coupled with multistep reduced chemistry mechanism, found that PAH is sensitive to scalar dissipation rate, in opposite to acetylene species, which is much less sensitive to scalar dissipation rate. Thus, any acetylene-based model will misrepresent the turbulent mixing effect on soot due to differences in species Damkohler number. Further, soot traveling towards the flame is oxidized, and aggregates displaced away from the flame grow primarily by condensation of PAH on the particle surface. In addition to that, the morphology of the soot aggregates is found to depend on the location of soot in mixture fraction space. Aggregates with the largest primary particles populate the mixture fraction region close to peak soot growth. On the contrary, the aggregates with the largest number of primary particles are located much downstream of the fuel. The results show that soot is oxidized quickly moving towards the flame while soot moving away from the flame has long residence times for PAH condensation process to occur. Work by *Mueller et al.* (2013) shows that in a high residence time bluff-body ethylene flame, highest source of soot mass addition is not PAH condensation, but acetylene-based surface growth reactions. However, the area location of soot mass addition via PAH condensation is much larger than that of surface growth which mainly exists at the region close to the oxidizer side. This observation leads to further questions of how soot source terms evolve with residence time, scalar dissipation rate, and mixture fraction. This dissertation will develop a 0-D platform to study each of these individual aspects.

1.3 Turbulent Combustion Modeling

This section describes the starting point for a computational investigation into fluid turbulence and combustion phenomena, uncoupled from soot modeling. The governing equations for gaseous combustion is described in Section 1.3.1. Then Section 1.3.2 describes the filtering equations for LES modeling of flow turbulence. Finally, Section 1.3.3 describes the chemistry model for the combustion process.

1.3.1 Equations for Gaseous Combustion

A working set of conservation equations governing gaseous combustion are summarized below. They are valid for ideal gas mixtures in local thermo-equilibrium and chemical nonequilibrium (*Pierce* (2001); *Poinsot and Veynante* (2001)).

Continuity:

$$\frac{\partial \rho}{\partial t} + \nabla \cdot (\rho \mathbf{u}) = 0 \tag{1.34}$$

Momentum:

$$\frac{\partial \rho \mathbf{u}}{\partial t} + \nabla \cdot (\rho \mathbf{u}\mathbf{u}) = -\nabla p + \nabla \cdot \big[2\mu\big(\mathbf{S} - \frac{1}{3}\mathbf{I}\nabla \cdot \mathbf{u}\big)\big] \tag{1.35}$$

where a low-Mach number set of neglected phenomena are assumed for this dissertation. This includes acoustic interactions and compressibility, viscous heating, bulk viscosity, body forces, and diffusion from pressure gradient.

The low-Mach number assumption essentially decouples the thermodynamic variables like density, temperature and enthalpy from pressure variations. Only the constant background pressure, p_0 is entered into the thermodynamic equation of state (Eq.1.36).

$$p_0 = \rho \sum_i \frac{y_i}{M_i} RT \tag{1.36}$$

Scalars:

$$\frac{\partial \rho \phi}{\partial t} + \nabla \cdot (\rho \mathbf{u} \phi) = \nabla \cdot \big(\rho \alpha \nabla \phi\big) + \rho \dot{w} \tag{1.37}$$

where ϕ can be any transported scalar including total enthalpy, defect enthalpy, mixture fraction, progress-variable, and species mass fractions. α and $\dot{w}$ are diffusion property and production rates obtained from the combustion model described in Section 1.3.3. ρ and μ used throughout these set of equations are also obtained from the combustion model.

1.3.2 Large Eddy Simulation

In this dissertation, the reacting flow equations in Section 1.3.1 are solved using large eddy simulation (LES). In LES, the large scales of motion are numerically simulated while the small, unresolved scales and their interaction with the large scale are modeled. The large scale field like velocity, $\widetilde{u}$ is Favre filtered (density-weighted decomposition) as in Eq. 1.38 (*Sagaut* (2006)).

$$\widetilde{u} = \frac{\overline{\rho u}}{\overline{\rho}} \tag{1.38}$$

where the overbar operator is the grid-filtering operation that removes the small scales and leave the resolved (large) scales. $\widetilde{u}$ is related to the full scale quantity, u, via Eq. 1.39.

$$u = \widetilde{u} + u'' \tag{1.39}$$

Applying the decomposition process into the governing equations (Eq. 1.34 - Eq. 1.37) and subjecting the equations to grid filtering (*Pierce* (2001)):

Continuity:

$$\frac{\partial \overline{\rho}}{\partial t} + \nabla \cdot (\overline{\rho}\widetilde{u}) = 0 \tag{1.40}$$

Momentum:

$$\frac{\partial \overline{\rho}\widetilde{u}}{\partial t} + \nabla \cdot (\overline{\rho}\widetilde{u_i}\widetilde{u_j}) = -\nabla \overline{p} + \nabla \cdot \left(2\overline{\mu}\widetilde{S_{ij}}\right) + \nabla t_{ij} \tag{1.41}$$

where $\widetilde{S}_{ij}$ is defined as:

$$\widetilde{S}_{ij} = \frac{1}{2}\left(\widetilde{u}_{i,j} + \widetilde{u}_{j,i}\right) - \frac{1}{3}\partial_{ij}\nabla\widetilde{u}_k \tag{1.42}$$

and t_{ij} is the unclosed residual stress term which is modeled using the dynamic subgrid scale approach of *Moin et al.* (1991) and *Germano et al.* (1991) with eddy viscosity assumption.

Scalars:

$$\frac{\partial\overline{\rho}\widetilde{\phi}}{\partial t} + \nabla\cdot(\overline{\rho}\widetilde{u}_j\widetilde{\phi}) = \nabla\cdot\left(\overline{\rho}\widetilde{\alpha}\nabla\widetilde{\phi}\right) + \overline{\rho}\widetilde{\dot{w}} + \nabla q \tag{1.43}$$

where $\widetilde{\dot{w}}$ and q are the unclosed chemical source terms and residual scalar flux term respectively. The unclosed chemical source terms for combustion will be discussed in Section 1.3.3. The residual scalar flux term is closed using the dynamic subgrid scale approach of *Moin et al.* (1991) and *Germano et al.* (1991) with gradient-diffusion assumption using eddy diffusivity. For conserved scalars (no source term in the scalar transport equation), the computation of Favre filtered quantities are closed with the joint assumed probability density function (PDF) approach using a beta distribution (*Wall et al.* (2000)).

In combustion, the state relations are nonlinear functions and depending on the combustion model, it could be known prior to the simulation itself. These PDF integrals can be computed and stored in lookup tables prior to the simulation and retrieved as functions of the filtered scalars and their variances during simulation.

1.3.3 Radiation Flamelet Progress-variable model

The fundamental platform of combustion modeling for this dissertation is the flamelet model (*Peters* (1984, 2000)) for nonpremixed flame. The turbulent flame is conceptualized as an ensemble of laminar "flamelets" in a strained flow field and could be pre-computed prior to the simulation. The flame structure can be parameterized in terms of a reduced set of variables and these variables transported during the simulation. The thermodynamic variables and other quantities parameterized can be accessed during the simulation using lookup and interpolation method. The method used for this dissertation is extended from the flamelet method to account for PAH species transport (*Mueller* (2012)).

The thermochemical state for combustion in this dissertation is described with the Radiation Flamelet Progress-variable (RFPV) model where the thermochemical state, ξ, is parameterized by the mixture fraction, Z, progress-variable, C, and heat loss parameter, H as shown in Eq. 1.44.

$$\xi = f\big(Z, C, H\big) \tag{1.44}$$

This method is an extension to the original mixture fraction-progress-variable method to account for radiation heat loss from specific reaction species and soot particles (*Ihme and Pitsch* (2008)). The coupling to soot scalars which requires another final set of transported scalars is described in Section 1.4. The transport terms for each of the parameters in RFPV model used in this dissertation are laid out below and is covered in more detail in *Mueller* (2012).

Mixture fraction, Z, is typically a conserved scalar and is defined as the mixedness between fuel (1.0) and oxidizer (0.0). Instead of transporting every species in the chemistry mechanism for large fuels, one scalar is used to define the mixedness, thus reducing the computational time and increases tractability for computing large hydrocarbon fuels. However, for transporting soot related quantities and to take into account the consumption of PAH species (explained below), Z is not a conserved scalar in this dissertation and is defined in Eq. 1.45 (filtered).

$$\frac{\partial \overline{\rho}\widetilde{Z}}{\partial t} + \nabla \cdot \big(\overline{\rho}\widetilde{u}_i\widetilde{Z}\big) = \nabla \cdot \big(\overline{\rho}\widetilde{D_Z}\nabla\widetilde{Z}\big) + \nabla \cdot \big(\overline{\rho}\widetilde{u}_i\widetilde{Z} - \overline{\rho}\widetilde{u_i Z}\big) + \overline{\dot{m}_Z} \tag{1.45}$$

where $\dot{m}_Z$ is the mixture fraction source term mapped in the flamelet table and is defined explicitly in *Mueller* (2012). Note that this transport equation is similar to the general transport equation defined in Eq. 1.37. A limit of unity Lewis number (Le) is assumed for this formulation, indicating that the species and thermodynamics are transported or convected at the same rate without differential diffusion. This assumption holds for the composition of fuels and oxidizers used in this dissertation.

The progress-variable, C term is defined as the sum of mass fractions of the major products in combustion (e.g. CO, H_2O). However, the method used in this dissertation which accounts for removal of PAH species from the composition is written as follows in Eq. 1.46 (filtered)

$$\frac{\partial \overline{\rho}\widetilde{C}}{\partial t} + \nabla \cdot \left(\overline{\rho}\widetilde{u}_i\widetilde{C}\right) = \nabla \cdot \left(\overline{\rho}\widetilde{D_C}\nabla\widetilde{C}\right) + \nabla \cdot \left(\overline{\rho}\widetilde{u}_i\widetilde{C} - \overline{\rho}\widetilde{u_i C}\right) + \frac{\overline{\dot{m}_C}}{C^*} \tag{1.46}$$

where $\dot{m}_C$ is the conventional progress variable source term (*Pierce* (2001)) and C^* is defined as the sum of the mass fractions of CO_2 and H_2O in a hydrocarbon one step oxidation reaction. This is the normalizing term to account for PAH removal. Further, limit of unity Le for progress variable is also assumed in this dissertation.

The heat loss parameter, H, is defined as the enthalpy defect term where when soot or certain species are present, long time-scale radiation effects will affect the thermodynamics of the composition. It is defined in Eq. 1.47 (filtered).

$$\frac{\partial \overline{\rho}\widetilde{H}}{\partial t} + \nabla \cdot \left(\overline{\rho}\widetilde{u}_i\widetilde{H}\right) = \nabla \cdot \left(\overline{\rho}\widetilde{D_H}\nabla\widetilde{H}\right) + \nabla \cdot \left(\overline{\rho}\widetilde{u}_i\widetilde{H} - \overline{\rho}\widetilde{u_i H}\right) + \overline{\dot{\rho}H} + \overline{\dot{Q}} \tag{1.47}$$

where $\dot{Q}$ is the radiation source term. Again, the limit of unity Le for H is assumed.

In parallel to the transport of scalars during the simulation, pre-computations of solutions to flamelet equations for the flamelet table mapping to the parameters described above is required. The system of one-dimensional unsteady equations for different scalar dissipation rate is described in detail in *Mueller* (2012) (Chap 3.1.2) and the exact formulation is used to derive the source terms to Eq. 1.45 - Eq. 1.47.

1.4 Coupling of Soot Model to Turbulent Combustion Model

To couple soot-related quantities to turbulent combustion models described in the previous section, two more sets of transport equations need to be considered. The first is the lumped PAH mass fraction equation to account for the consumption of PAH species sensitive to scalar dissipation rate. The other is the moment (or weight and abscissa depending on method of moment) transport equation already explicitly described in Eq. 1.10.

$$\frac{\partial \overline{\rho} \widetilde{Y_{PAH}}}{\partial t} + \nabla \cdot \left(\overline{\rho} \widetilde{u}_i \widetilde{Y_{PAH}} \right) = \nabla \cdot \left(\overline{\rho} \widetilde{D_{Y_{PAH}}} \nabla \widetilde{Y_{PAH}} \right) + \nabla \cdot \left(\overline{\rho} \widetilde{u}_i \widetilde{Y_{PAH}} - \overline{\rho} \widetilde{u_i Y_{PAH}} \right) + \overline{\dot{m}_{Y_{PAH}}} \tag{1.48}$$

where the source term for PAH species, $\overline{\dot{m}_{Y_{PAH}}}$, is obtained following the work of *Ihme and Pitsch* (2008) for NO species using scale-similarity assumption. This dissertation uses the same closure model to that of *Mueller* (2012).

The transport of filtered moment equation is described in Eq. 1.49.

$$\frac{\partial \overline{M_{x,y}}}{\partial t} + \nabla \cdot \left(\widetilde{u}_i \overline{M_{x,y}} \right) = \nabla \cdot \left(\widetilde{u}_i \overline{M_{x,y}} - \overline{u_i M_{x,y}} \right) + \overline{\dot{M}}_{x,y} \tag{1.49}$$

where $\overline{\dot{M}}_{x,y}$ is described in detail in Section 1.2.4 and generated from the flamelet calculations to be looked up during simulation. Similar presumed PDF approach for thermochemical and soot variables are used as described in Section 1.3.2. An important aspect is the soot subfilter PDF model and this dissertation uses the subfilter intermittency model described in *Mueller* (2012) where ω is used with a PDF function to compute the intermittency of subgrid scale soot.

1.5 Large Eddy Simulation of Soot in Aircraft Combustors

With increase in operating pressures of aircraft combustors, it is expected that there will be an accompanying increase in particulate emissions (*Karatas and Gülder* (2012)). Although modern combustors operate at globally lean equivalence ratios, locally inefficient turbulent mixing can lead to fuel-rich pockets that promote particulate formation. Understanding the role of such mixing processes and the effect of pressure increase on soot emissions is critical for the development of next generation gas turbines. In this context, detailed computational modeling is a useful tool. However, developing predictive computational models for soot is recognized as a formidable challenge (*Wang* (2011); *Mueller* (2012)). Due to the high Reynolds number turbulent flow within an aircraft combustor, soot formation is intricately linked to the turbulence-chemistry interaction associated with both fuel oxidation and soot evolution processes. Although significant progress has been made in the modeling of soot formation in flames (*Charest et al.* (2011b); *Raman and Fox* (2016)), application of these tools to realistic gas turbine flows and direct comparison with experiments remains sparse.

It is now accepted that the use of large eddy simulation (LES) is necessary to capture the turbulent mixing driven combustion processes that govern aircraft-type combustors (*Pitsch* (2006)). In particular, LES has been applied to model gas-phase combustion in a variety of aircraft combustor geometries, with very good success in the prediction of the overall flow characteristics (*Mahesh et al.* (2004); *Mueller and Pitsch* (2013); *Poinsot and Veynante* (2001); *Mare et al.* (2004); *Koo et al.* (2017)). In many of these applications, the use of tabulated flamelet approaches has been shown to be accurate for operating conditions far away from blowout or other extinction phenomena (*Koo et al.* (2015, 2016b); *Mueller and Pitsch* (2013); *Ham et al.* (2003)). For this reason, in this dissertation, LES with flamelet approach is used to model the turbulent combustion process. The simulation of soot formation is itself a complex problem. This includes the chemical and physical models that govern gas-phase precursor and particulate-phase evolution (*Frenklach and Wang* (1991b); *Wang and Frenklach* (1997); *Mueller* (2012)), as well as the computational description of the nanoparticle population balance (*Frenklach and Harrris* (1986); *Marchisio and Fox* (2005); *Mueller et al.* (2009); *Raman and Fox* (2016)). Aided by increasing computational power, detailed models as well as the framework for such comprehensive simulations have been developed (*Lindstedt and Louloudi* (2005); *Donde et al.* (2013); *Mueller* (2012); *Xuan and Blanquart* (2015)). This method incorporates detailed chemical kinetics for the fuel oxidation and precursor formation, turbulence-chemistry interaction using a presumed-PDF approach (*Pierce and Moin* (2004)), and nanoparticle evolution through the method-of-moments (*Mueller et al.* (2009)).

Over the last decade, validation studies that utilize high-fidelity experimental data have emerged for sooting flames. The International Sooting Flames Workshop (ISF) (isf (2016)) provides one such central forum for model validation. An analysis of results presented there and elsewhere (*Xuan and Blanquart* (2015); *Mueller et al.* (2013); *Donde et al.* (2013); *El-Asrag and Menon* (2009); *Lindstedt and Louloudi* (2005)) provides interesting insights. Canonical jet flames, which are amongst the simplest turbulent flows that support chemical reactions, are found to be a challenging configuration for soot prediction. While there are numerous literature studies demonstrating the accuracy of LES in predicting gas-phase jet flames (*Pitsch* (2006); *Raman and Pitsch* (2006); *Kempf et al.* (2006)), similar computational models fail to predict soot concentrations spectacularly, often providing volume fractions that are orders of magnitude lower (or higher) compared to experiments (isf (2016)). Part of this discrepancy is due to the high sensitivity of soot formation to gas-phase thermochemical composition. For instance, *Mueller and Raman* (2014) have shown that even small errors in temperature mismatch with experiments can lead to significant errors in soot predictions. Further, models for soot evolution are often formulated based on data from laminar flames, which may not be representative of the conditions seen in a turbulent flame. This includes the range of strain rates, as well as the spatial and temporal variations in the thermochemical composition of the gas-phase, which introduces a history-dependent evolution of the soot particles.

Since different physical and chemical processes dictate soot formation, the relative importance as well as accuracy determine predictive capability. Temperature perturbations resulted in downstream soot volume fraction errors of 30% in turbulent nonpremixed piloted jet flames (*Mueller and Raman* (2014)), however this was insufficient to explain the discrepancies with experimental data. Other sources of error in turbulent combustion modeling or chemistry mechanism are likely responsible as well. In jet flames burning ethylene fuel, models that employ PAH-based precursor chemistry vastly underpredict soot volume fraction (isf (2016)). On the other hand, semi-empirical models (*Leung et al.* (1991)) that rely on acetylene-based nucleation predict much higher soot mass (*Lindstedt and Louloudi* (2005)). Since PAH concentrations are highly sensitive to strain rates, it is possible that either inaccurate precursor chemistry or errors in models for small-scale dissipation/strain rates leads to this discrepancy. On the contrary, bluff-body stabilized flames are well represented even by PAH-based models, where surface growth by an acetylene-addition mechanism dominates (*Frenklach and Wang* (1991b); *Wang and Frenklach* (1997); *Mueller et al.* (2013)). Consequently, there is some uncertainty in the cause of model discrepancy.

Since aircraft engines form one class of end application for these models, it is imperative to test predictive capability in near-realistic conditions. The DLR model aircraft combustor experiments (*Geigle et al.* (2014)) provide high-fidelity measurements such as three-component flow field, temperature, and soot volume fraction statistics, ideal for testing detailed computational models. In particular, the combustor allows secondary air injection, which emulates dilution jets in rich-quench-lean type aircraft combustors. This combustor configuration has been previously simulated using unsteady Reynolds-Averaged Navier Stokes (URANS) approach (*Eberle et al.* (2014, 2015)) and LES techniques (*Koo et al.* (2016b); *Wick et al.* (2017b)). The URANS study used a semi-empirical soot model, combined with finite chemistry, sectional description of PAH, along with conventional turbulence models, and was able to capture the location of soot formation. The LES calculations showed similar fidelity, capturing the gas-phase flow field and soot locations quite accurately. Still, the LES approach overpredicted soot volume fraction by a factor ranging from 2 to an order of magnitude.

One of the focus of this dissertation is to simulate the DLR configuration at higher operating pressures of 3 and 5 bar. For each of these conditions, simulations with and without sidejet injection were considered. The focus is on understanding the relative importance of different physical and chemical processes that lead to soot generation, evolution, and destruction.

1.6 Executive Summary

A brief summary of the (i) novelty, (ii) methodology, and (iii) findings for each contribution is provided below.

- **Soot-Turbulence-Chemistry Interactions in Partially-Stirred Reactor**: To study the small scale soot evolution in one computational cell, (i) which has not been investigated before in literature, (ii) a new 0-D platform is developed where different fluid time-scales can be enforced, and coupled to different soot models. In **Chapter II**, (iii) it is found that all detailed PAH-based soot detailed models scale similarly to mixing and residence time in predicting soot volume fraction. When other soot properties are concerned, different method of moment closure methods predict different soot particle diameter and number densities. Chemistry mechanism also plays an important effect on soot prediction as soot precursor species mass fractions are affected. The effect of scalar dissipation rate on soot precursor species like acetylene and PAHs also directly affect soot prediction and its scaling.

  - S. T. Chong, W. Han, Z. Chen, P. Selvaraj, M. E. Mueller, H. G. Im, V. Raman, *On method of moments and chemistry in modeling soot formation for high pressure turbulent non-premixed combustion*, In preparation (2018)

- **Large Eddy Simulation of Turbulent Sooting Flame in Aircraft Combustor**: From 0-D computation to complex configurations, the simulation of turbulent sooting flames requires a host of models. Two of the most important aspects are: chemical kinetics and soot statistical model. (i) Sensitivity of these two aspects to soot formation in a complex combustor is not yet available, using the same turbulent combustion platform. (ii) Two different chemistry mechanism and three different soot statistical approaches are compared, using the recently developed in-house turbulent combustion solver. In **Chapter II**, (iii) simulations show that the acetylene-based soot inception model produces very high soot volume fraction, with soot volume fraction highest in the inner recirculation zone. The two PAH-based advanced soot models lead to soot generation in the shear layers. Comparing between the method of moments, differences in prediction of soot number density and particle diameter are also seen, consistent with results seen using the 0-D platform.

  - S. T. Chong, V. Raman, M. E. Mueller, P. Selvaraj, H. G. Im, *Effect of soot model, moment method, and chemical kinetics on soot formation in a model aircraft combustor*, Proc. Combust. Inst. (2018)

  - M. Hassanaly, H. Koo, C. F. Lietz, S. T. Chong, V. Raman, *A minimally-dissipative low-mach number solver for complex reacting flows in openfoam*, Comp. Fluids 162 (2018) pp. 11-25

- **Hydrodynamic Scaling on Soot in Pressurized Turbulent Sooting Flame**: Simulations and predictions for soot in an aircraft combustor is expensive and rare in the literature. (i) In-depth analysis of soot formation and evolution in these realistic configurations, using the current state-of-the-art turbulence, chemistry, and soot models were not available. (ii) A minimally-dissipative turbulent combustion solver with Hybrid Method of Moment (HMOM) soot statistical model is used to simulate a model aircraft combustor with sidejet air injection. In **Chapter III**, (iii) it is found that despite good soot volume fraction predictions in the shear jet location, soot is underpredicted spatially especially in the inner recirculation zone and downstream of the combustor. Lagrangian particle analysis also revealed the entrainment of soot particles into the inner recirculation zone, increasing the residence time and leading to increased soot volume fraction. With pressure increase, there is also a hydrodynamic scaling mode identified, along with nominal pressure scaling for soot production in an aircraft combustor.

  - S. T. Chong, M. Hassanaly, H. Koo, M. E. Mueller, V. Raman, K. P. Geigle, *Large eddy simulation of pressure and dilution-jet effects on soot formation in a model aircraft swirl combustor*, Combust. Flame 192 (2018) pp. 452-472

- **Fourier Analysis of Turbulent Sooting Flame**: Soot is a slow process both chemically and physically. (i) However, the comparison of differences in time scale in a realistic configuration is not yet performed. In **Chapter IV**, (ii) a Fourier analysis for turbulent sooting flame in a model aircraft combustor is performed. (iii) It is found that there is a separate, lower frequency soot mode to the dominant flow mode that controls the accumulation/dispersion cycle for the bulk of soot mass generated in the combustor.

- S. T. Chong, V. Raman, M. E. Mueller, H. G. Im, *The role of recirculation zones in soot formation in aircraft combustors*, in: ASME Turbo Expo 2018, GT2018-76217

CHAPTER II

Soot-Turbulence-Chemistry Interactions

2.1 Small Scale Soot-Turbulence-Chemistry Interactions

As described in Chapter 1.2.5, results from DNS studies can help with studies of soot-turbulence-chemistry interactions but the computational cost is prohibitive. Further questions on the individual effects of residence time, scalar dissipation rate, chemistry mechanism, and mixture fraction on soot evolution are still unanswered. This chapter's objective is to bridge these gaps by introducing a 0-D tool that enforces turbulent time scales. With this tool, the effects of varying residence and mixing times to soot formation and how sensitive soot prediction is to chemistry mechanism, mixing models, pressure and soot models are investigated. First, the 0-D tool (Partially-stirred reactor) and the chemistry mechanisms are introduced then the models are validated with data from laminar burner-stabilized flame configuration. Results are then analyzed for changes in residence time, soot dynamic model, chemistry mechanism, mixing models and pressure increase. A pressure scaling of soot volume, conditioned on mixing time is also discussed. Finally, a summary of findings is outlined.

2.2 Methodology

2.2.1 Partially-Stirred Reactor

An in-house Partially-Stirred Reactor (PaSR) (*Correa* (1993); *Chen* (1997)) Fortran-based code with coupled soot module is the main tool in this study. It is analogous of one cell in a complex simulation where the velocity time scales are enforced through two parameters: residence time and mixing time. The joint scalar PDF transport equation is evolved for N-ensemble particles. This is a degenerate form of the joint velocity-scalar PDF equation by *Pope* (1985) whereby only species, enthalpy, and soot moment ODE equations are solved for via time-stepping in each particle. The resulting pdf equation is shown in Eq. 2.1 (*Chen* (1997)).

$$\begin{aligned}\frac{\partial \widetilde{P}_{\overline{\phi}}(\overline{\psi},t)}{\partial t} = & -\sum_{\alpha=1}^{k} \frac{\partial}{\partial \psi_\alpha}\{S_\alpha(\overline{\psi})\widetilde{P}_{\overline{\phi}}(\overline{\psi},t)\} \\ & + \frac{1}{\tau_{res}}\{\widetilde{P}_{\overline{\phi},in}(\overline{\psi}) - \widetilde{P}_{\overline{\phi}}(\overline{\psi},t)\} \\ & - \sum_{\alpha=1,\beta=1}^{k} \frac{\partial^2}{\partial \psi_\alpha \partial \psi_\beta}\{\langle \epsilon_{\alpha\beta} | \overline{\phi} = \overline{\psi}\rangle \widetilde{P}_{\overline{\phi}}(\overline{\psi},t)\}\end{aligned} \tag{2.1}$$

where ψ and ϕ are the sample space and random variable respectively and $\widetilde{P}_{\overline{\phi}}(\overline{\psi},t)$ the joint PDF. S_α is the source term from combustion reaction. The first two terms on the right hand side represent the effects of chemical source term from combustion and in-and-outflow respectively. τ_{res} is defined as the ratio between the total mass in the reactor and the mass flow rate at the exit, which are constants. The last term on the right hand side is the effect of micro-scale mixing on the pdf which requires modeling. Mixing between the notional particles is modeled by a linear deterministic relaxation to the mean (Interaction-by-Exchange-with-the-Mean (IEM)) model (*Correa* (1993)). It has been used in numerous occasions in the literature and the fields of mean and variance of conserved scalar compared favorably with Raman data from a bluff body nonpremixed turbulent flame (*Raman and Pitsch* (2006)). The equation describing

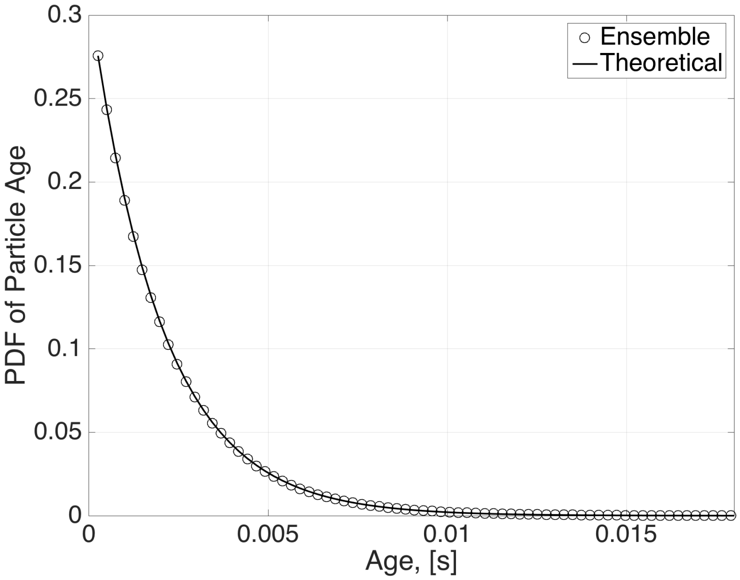

Figure 2.1: Comparison of theoretical and ensemble pdf of particle age for 1600 notional particles in this study. Residence time = 2ms, Mixing time = 0.1ms.

the IEM model is in Eq. 2.2. (*Dopazo* (1975))

$$-\sum_{\alpha=1,\beta=1}^{k} \frac{\partial^2}{\partial\psi_\alpha\partial\psi_\beta}\left\{\langle\epsilon_{\alpha\beta}|\overline{\phi}=\overline{\psi}\rangle\widetilde{P}_{\overline{\phi}}(\overline{\psi},t)\right\} = \frac{\partial}{\partial\psi_\alpha}\left[\frac{(\overline{\psi}-\widetilde{\overline{\phi}})}{2\tau_{mix}}\widetilde{P}_{\overline{\phi}}(\overline{\psi},t)\right] \tag{2.2}$$

where τ_{mix} is the mixing time.

To validate the PaSR solver, a comparison of the ensemble pdf particle age with theoretical exponential particle age is plotted in Fig. 2.1. For particle outflow that goes through a random selection process, the theoretical pdf of particle age is expected to be described by Eq. 2.3

$$P(\alpha) = \left[exp(-\alpha/\tau_{res})\right]/\tau_{res} \tag{2.3}$$

where α is the particle age. As shown, the ensemble pdf agrees very well with the theoretical values and any discrepancies are caused by finiteness of the sample size. For this study, 1600 notional particles are being used, with prior convergence studies taking 800, 1600, 8000, and 16000 particles into account. 1600 particles gives us the most optimal compromise between accuracy and computational time. Similar agreement is obtained for cases with differing mixing times. This provides an additional convergence check on the algorithm for the PaSR solver.

2.2.2 Chemistry mechanism

The two chemistry mechanism and thermodynamic models used in this study are selected based on the popularity and accuracy of predicting soot precursors and will hereafter be referred to as (i) Stanford mechanism, and (ii) KAUST mechanism.

Stanford mechanism is a reduced mechanism based on the detailed mechanism developed by *Blanquart et al.* (2009). The original mechanism contains 149 species and 1651 forward and backward reactions and has been validated with experimental data up to 25 bar pressure on ignition delay, laminar burning velocities, laminar premixed flame, and counterflow diffusion flames to accurately predict important soot precursors (eg. C_2H_2, C_4H_6) and PAHs up to cyclo[cd]pyrene. The reduced mechanism is from *Bisetti et al.* (2012) with 47 species and 279 reactions. The reduction process via multi-step approach takes into account important PAH species like naphthalene as the rate-limiting step in the formation of larger PAHs. Naphthalene is considered as the smallest aromatic species to forming dimers and species larger than naphthalene and their reactions are taken out of the detailed mechanism. Further reduction via Direct Relation Graph with Error Propagation (DRGEP) (*Pepiot-Desjardins and Pitsch* (2008)) and chemical lumping is done to cut the chemistry model down. The final reduced mechanism is validated against laminar burning velocity, rich premixed and diffusion flames to predict soot precursors and the results are in excellent agreement with experimental data.

The KAUST mechanism is also a reduced mechanism based on the original mechanism by *Metcalfe et al.* (2013), containing 397 species. The detailed mechanism has been validated using flow reactor, shock tube and jet-stirred reactor for C1-C2 hydrocarbon and oxygenated fuels. The detailed mechanism (*Selvaraj et al.* (2016)) has been reduced via Directed Relation Graph method with Expert Knowledge (DRG-X) and sensitivity analysis to 99 species and 1128 reactions. The mechanism has PAH species till coronene, which is a seven-ring structure. The target parameters for the reduction include auto-ignition delay, extinction time in perfectly stirred reactors (PSR), and concentrations of important PAH species from pyrene to coronene. The reduced mechanism agrees extremely well with the detailed mechanism for these parameters from 0.1 to 10 atm pressure and equivalence ratio of 0.5 to 5.0 for ethylene/air opposed flames as shown in *Selvaraj et al.* (2016).

2.2.3 Mixing models

Molecular mixing models for PDF methods to simulate turbulent nonpremixed reactive flows are critical to prescribe the evolution of notional particles in composition space. In this study, three mixing models are compared: (i) Interaction by Exchange with the Mean (IEM) (*Dopazo* (1975); *Dopazo and O'Brien* (1974)), (ii) Modified Curl (MC) (*Janicka et al.* (1979)), and (iii) Euclidean Minimum Spanning Tree (EMST) (*Subramaniam and Pope* (1998)).

For the IEM model, each particle mix with the Favre mean of the particle ensemble. Therefor, an ODE of $\overline{\phi}$ is solved with Eq. 2.2 as the RHS. Regarding the simplicity and efficiency, the IEM model is widely applied in PDF simulations. However, it preserves the shape of the PDF and cannot guarantee the local mixing. The MC model randomly picks several pairs of particles from the ensemble to conduct mixing between pairs. Due to the random pairing, MC does not mix particles locally in the composition space, similar with IEM. For instance, it allows unphysical mixing between fuel and oxidizer particles in high Da non-premixed flames. For the EMST

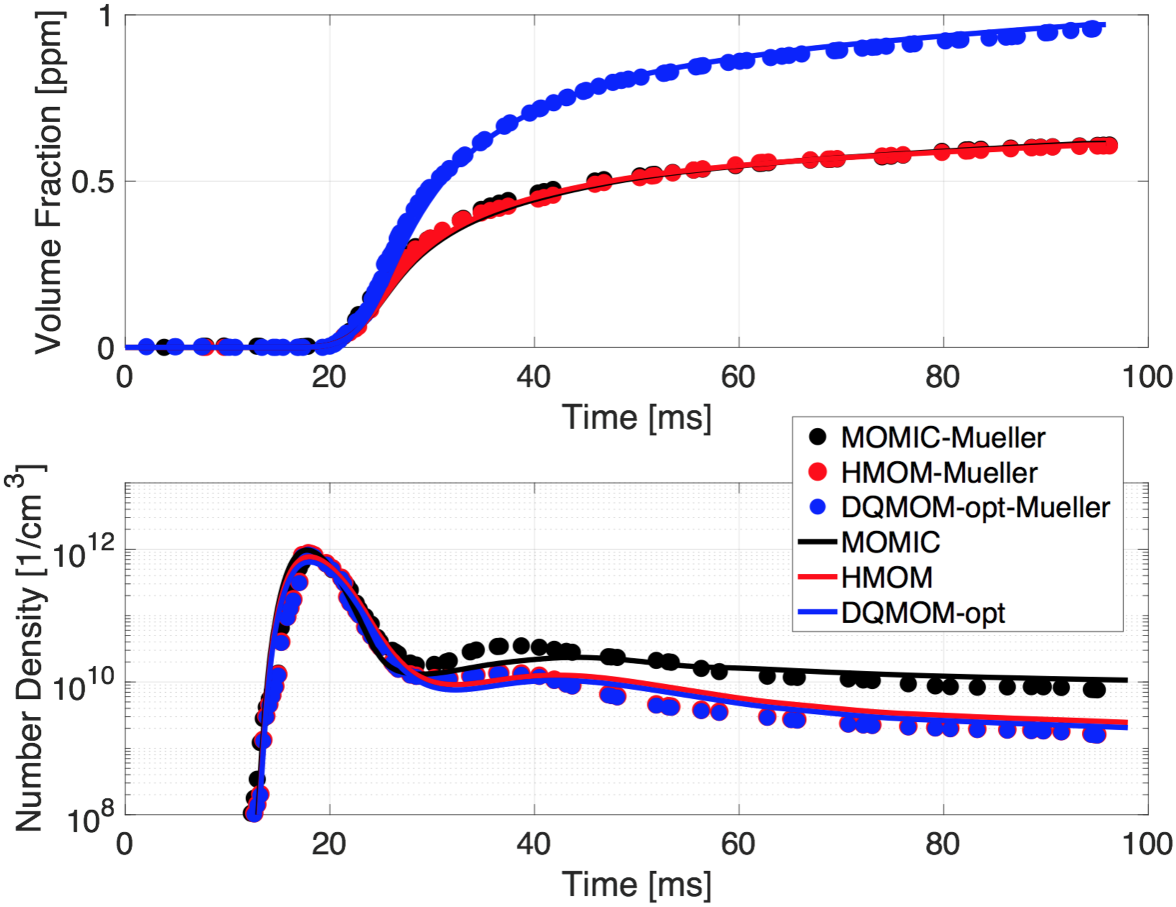

Figure 2.2: Comparisons of soot volume fraction and number density for particle-dynamics models used in this study (line) to similar models in *Mueller et al.* (2009) (scatter) for the laminar premixed ethylene burner-stabilized flame by *Xu et al.* (1997). DQMOM-opt is the optimized set of moments used in this study. A pure aggregation collision model is used for MOMIC and HMOM.

model, particles are mixed along the edges of an Euclidean minimum spanning tree constructed in the composition space. Because of the local mixing, EMST is shown to be more superior to the other two models for simulating diffusion flames (*Subramaniam and Pope* (1998)) despite the higher computational cost involved. In this study, the effects of differences in the pdf of mixture fraction to soot volume fraction produced are investigated.

2.2.4 Model validation

An ethylene laminar premixed burner-stabilized flame configuration by *Xu et al.* (1997) is used in this study for soot model validation. Comparisons with soot particle-dynamic model data in previous study (*Mueller et al.* (2009)) are used to validate the models used in this study. The comparison is made for the case with fuel to air equivalence ratio, $\phi = 2.64$, C/O ratio = 0.88, with ambient pressure and temperature for the mixture at burner exit. Pre-computed 1-D laminar flame speed and species mass fractions with *Blanquart et al.* (2009) mechanism using FlameMaster code (*Pitsch* (1998)) is coupled to a lagrangian 0-D code with the soot models. Pure aggregation collision model is used and oxidation is neglected in this validation study to compare the validity of the soot particle-dynamics models.

Figure 2.2 shows good comparisons for soot volume fraction and number density with literature model data. Considering the cell size clustering at the flame front location, good agreement seen at the flame front with peak soot number density is very encouraging.

2.3 Results

The PaSR studies reported below use ethylene (C_2H_4) as fuel with air introduced through a second inlet. The equivalence ratio is $\phi = 1.0$ with starting conditions of air at temperature of 2000 K to ignite the mixture initially. The mixing and combustion process are allowed to converge with time and ensemble average is taken over the total number of notional particles. The residence time is varied from 0.2 ms to 20 ms to see the frequency effect of one total mass change of fuel/air mixture affects soot formation. To examine the effect of mixing time or analogously, the scalar dissipation rate on soot formation, the mixing time is varied from 0.01 ms to 0.4 ms for a constant residence time at 2 ms (residence time to mixing time ratio of 200 to 5). This study is conducted for three different pressures at 1, 2, and 5 bar, aligning with realistic conditions in combustors, to study sensitivities of soot to scalar dissipation rate with increasing pressure. The same study is repeated for two chemical mechanisms and five different soot particle dynamic models described in Section 2.2.2 and 1.2 respectively. Further, the differences in soot properties are also studied under different mixing models, important to future use of PDF method in turbulent combustion soot modeling. Lastly, the evolution of soot and soot precursor species with scalar dissipation rate is also investigated, conditioned on lean and rich mixture fractions.

2.3.1 Residence time effect

The first effect studied is residence time, analogous to the velocity of the flow and one total mass change-over time in a volume cell. Figure 2.3 shows that with increasing residence time, soot volume fraction increases. This is consistent with literature where recirculation-dominated flows like bluff-body flames (*Mueller et al.* (2013); *Deng et al.* (2017)) reported factors higher soot volume near the bluff-body where residence time is higher.

The detailed soot models show similar behaviour and scaling to residence time. The acetylene-based SEMI model is less sensitive to residence time. At lower residence time, SEMI model is expected to produce approximately six orders of magnitude lower soot volume. In contrast, at higher residence time, the differences between the

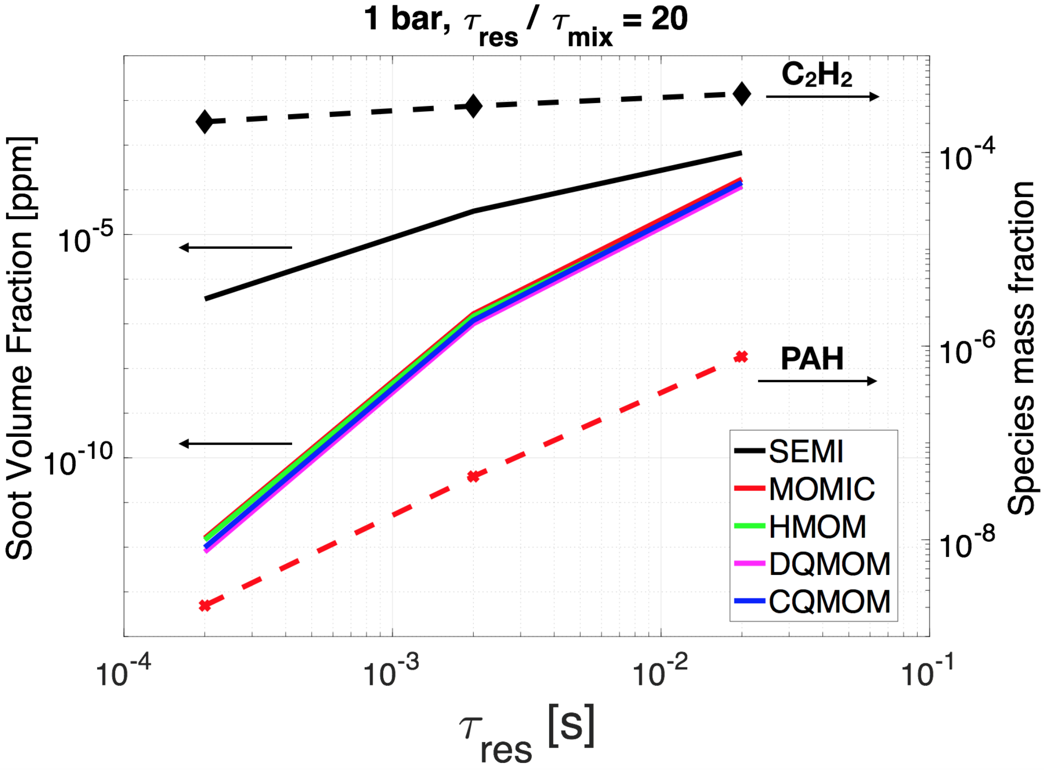

Figure 2.3: Comparison of soot volume fraction and species mass fractions for various soot particle-dynamic models with increasing residence time at 1 bar pressure. Constant ratio of $\tau_{res}/\tau_{mix} = 20$ and Stanford chemistry mechanism are used. SEMI and detailed soot models are sensitive to increase in C_2H_2 and PAH species mass fractions respectively with residence time.

detailed and acetylene-based models reduce to approximately an order of magnitude at 20 ms maximum residence time. This scaling can be attributed to the sensitivity of soot precursor species like acetylene (C_2H_2) and PAHs to residence time as shown in Fig. 2.3. As acetylene (C_2H_2) is less sensitive to changes in residence time compared to PAH, the soot volume fraction using SEMI model is subsequently less sensitive to residence time and vice-versa for detailed soot models with PAH as soot precursors.

2.3.2 Soot dynamic model effect

Soot statistical models have been in continuous development and improvement (*Leung et al.* (1991); *Frenklach* (2002); *Frenklach and Harrris* (1986); *Marchisio and Fox* (2005); *Mueller et al.* (2009); *Yuan and Fox* (2011)). In this study, where similar chemistry source terms: nucleation, coagulation, condensation, surface growth, and oxidation, are used (except SEMI) and the only varying factor is the moment closure, these detailed-chemistry soot statistical models behave similarly in terms of soot volume fraction with mixing time as shown in Fig. 2.4. Slight differences do occur at small mixing times where the source term is stiffer due to small mixing and reaction times.

Comparing detailed model to acetylene-based SEMI model where soot source terms are computed from a set of kinetic rates (Eq. 1.5 - Eq. 1.8), the SEMI model is shown to produce orders of magnitude higher soot volume fraction at small mixing times. It also produces a constant high number of soot particles compared to detailed models regardless of mixing time. This points to the less sensitive nature of acetylene-based models to scalar dissipation rate in predicting number of soot particles.

A larger difference is seen when comparing the soot number density and average particle diameter for detailed soot models in Fig. 2.4(b). MOMIC predicts larger soot particle diameter and lower number of soot particles at large mixing times (low scalar dissipation rate), relative to the other detailed models. However, the soot volume

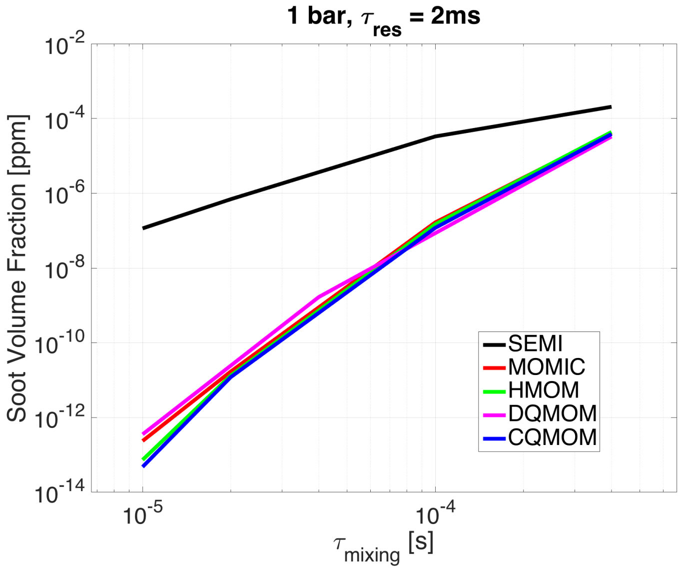

(a) Volume Fraction

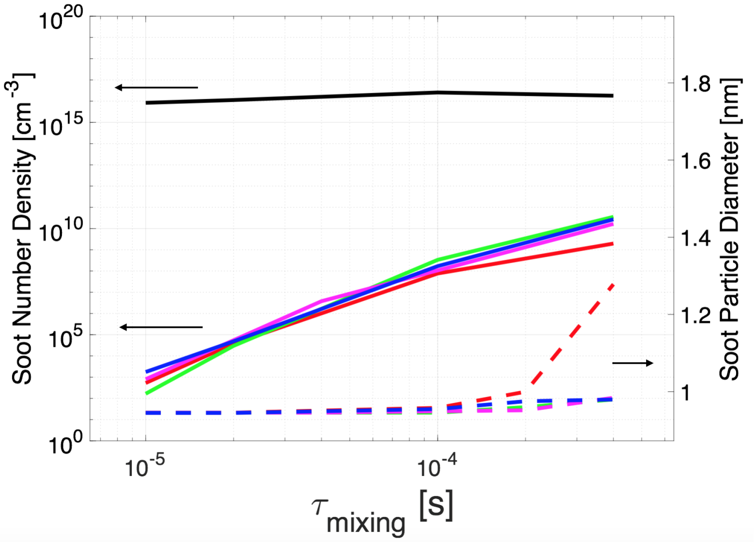

(b) Number Density

Figure 2.4: Comparisons of (a) soot volume fraction, (b) number density and particle diameter for different particle-dynamics models with increasing mixing time (decreasing scalar dissipation rate) at 1 bar and constant $\tau_{res} = 2$ ms, using Stanford mechanism. Nucleated particle has diameter of 0.95 nm. MOMIC predicts larger soot particle diameter and lower soot number density at larger mixing times, relative to DQMOM.

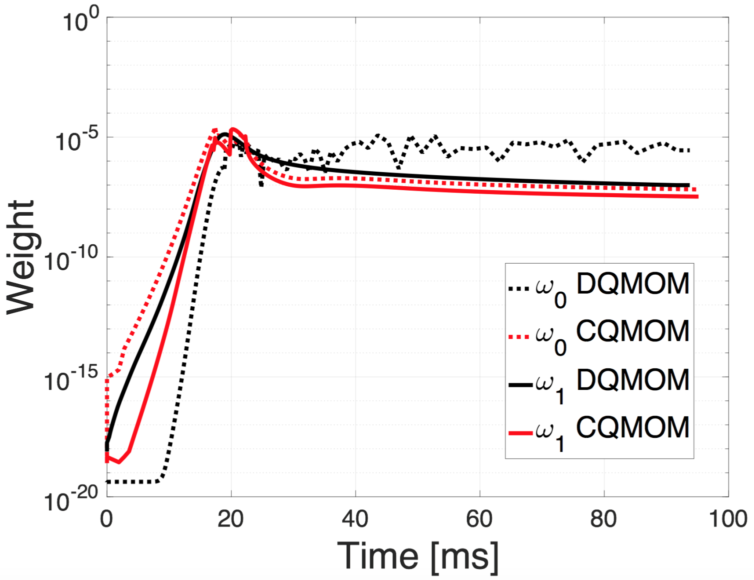

(a) Weight

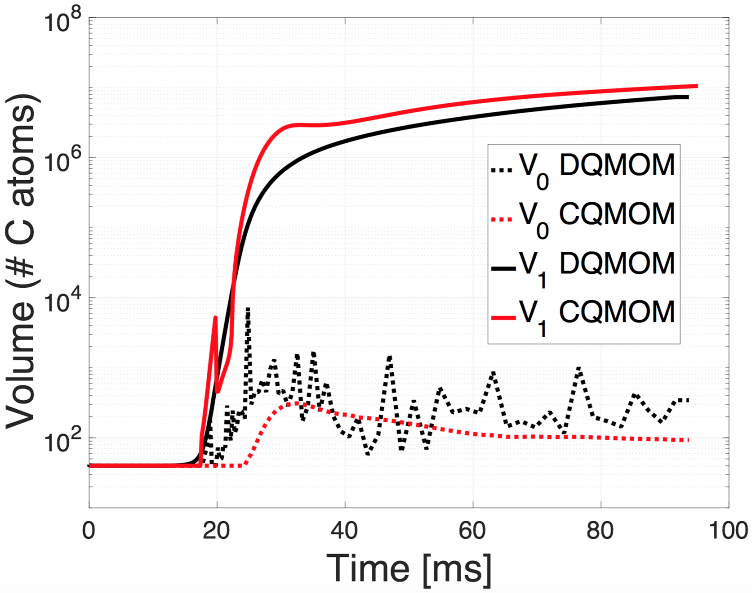

(b) Volume

Figure 2.5: Evolution of (a) weight (ω), and (b) volume (V) abscissas for DQMOM and CQMOM using similar temperature and species mass fraction profiles for a 1-D laminar premixed flame. CQMOM produces larger number of small nucleated particles during the initial stage and subsequently predicts larger sized particles downstream.

fraction from MOMIC is similar to the other detailed models. In other words, the different moment closure methods predict different particle size distributions that produce similar volume fractions. If particle size distribution is important and in complex geometries with substantial downstream regions where the prediction of soot particle size at the inlet will heavily influence coagulation and soot surface chemistry (growth and oxidation) at the downstream, the statistical model of HMOM, DQMOM or CQMOM should be considered for their ability to predict the small nucleated particles.

Despite predicting similar soot properties between DQMOM and CQMOM, the two statistical models that employ similar quadrature based method, the evolution of the weights and abscissas is compared in Fig. 2.5. ω_0 and V_0 corresponds to the weight and volume abscissa of the nuclei mode in the soot distribution while ω_1 and V_1 corresponds to the accumulation mode. Based on similar thermal profile and mixing frequencies for both models, CQMOM is shown to predict higher weight for nuclei particles initially (¡20 ms). At the downstream region, DQMOM predicts higher weight for nuclei particles. In terms of particle volume, DQMOM predicts larger nuclei particles and smaller accumulation mode particles compared to CQMOM. However, despite the slight differences, both DQMOM and CQMOM predict similar soot volume fractions.

Analyzing soot source terms in Fig. 2.6, similar to soot volume fraction and number densities, the detailed models scale similarly to mixing time. No significant deviation is found among the detailed models. Once again, SEMI model is relatively less sensitive to mixing time compared to detailed models, especially for nucleation. This shows that for the same flame configuration with increasing jet velocity and Reynolds number, SEMI model will produce a relatively constant number of soot particles but has a decreasing soot volume from lower surface growth rate.

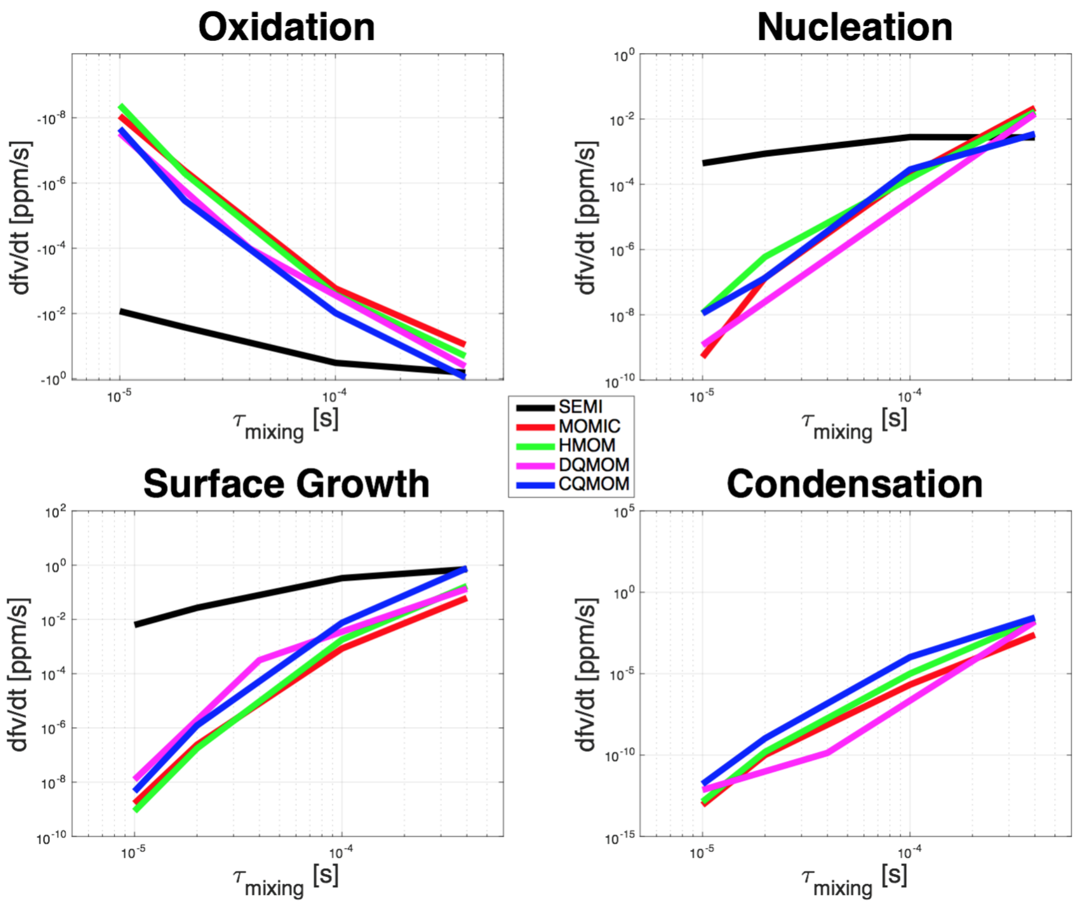

Figure 2.6: Comparison of soot volume fraction source terms for different particle-dynamic models with increasing mixing time at 1 bar and constant $\tau_{res} =$ 2 ms, using Stanford mechanism. Note that SEMI model is an acetylene-based model that does not include PAH condensation.

2.3.3 Chemistry mechanism effect

Among the variables in this study, chemistry mechanism has the most significant effect on soot prediction for the widely used detailed models. Soot volume fraction and number density increase in Fig. 2.7 when KAUST mechanism is used with the detailed models, compared to using Stanford mechanism. This is mainly due to the higher concentration of PAH at higher mixture fraction region shown in Fig. 2.8(a). The reason for the higher PAH mass fraction is due to the difference in number of PAH species considered from Naphthalene to pyrene in Stanford mechanism and from Naphthalene to coronene in KAUST mechanism. With higher PAH mass fraction, dimer production and PAH collision rates increase, subsequently increasing soot nucleation and condensation rates.

The opposite effect is observed with SEMI model. Using Stanford mechanism, SEMI model produces moderately higher soot volume fraction because of the higher concentration of acetylene in the same mixture fraction region (Fig. 2.8(b)). Despite the higher acetylene mass fraction, SEMI model produces constant soot number density, pointing to the consumption of acetylene in surface growth only. This study shows the sensitivity of the detailed model and SEMI model to PAH and acetylene mass fractions.

2.3.4 Pressure effect and scaling

Pressure increase is known to increase soot formation in laminar flames (*Charest et al.* (2011a); *Kailasanathan et al.* (2013); *Vargas and Gülder* (2017)). Recent International Sooting Flame (ISF) workshop pressurized target flame also showed soot volume increase from 3 bar to 5 bar in a model aero-combustor (*Geigle et al.* (2014, 2015)). However, scaling of soot with pressure is fundamentally difficult due to hydrodynamic effects on flame structure. Using PaSR, the hydrodynamic effect is separated from the chemistry effect and individually varied to see the effect on soot formation.

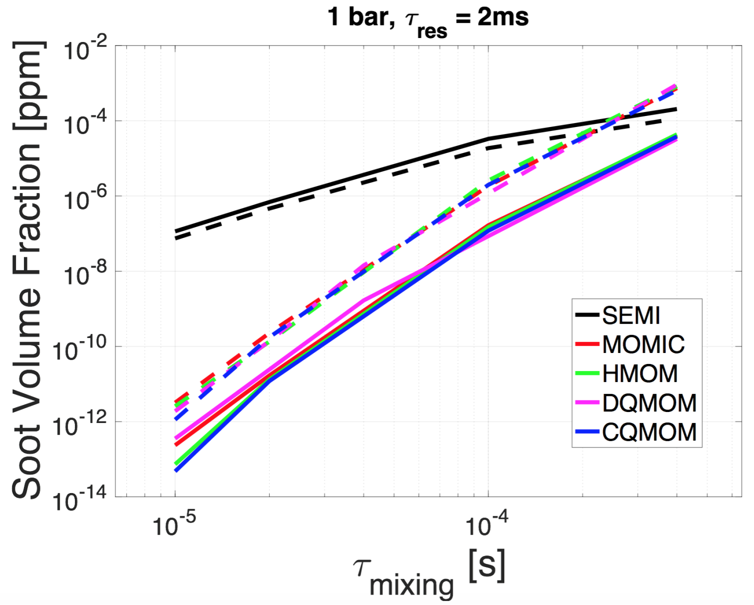

(a) Volume Fraction

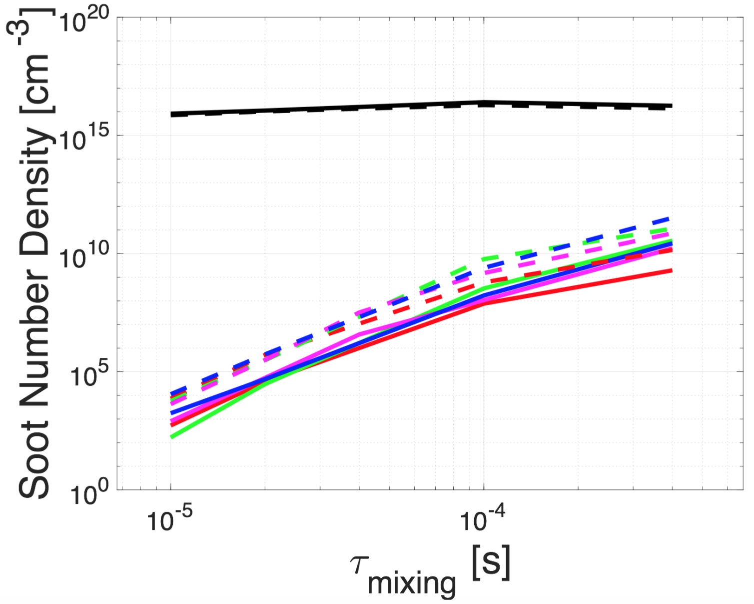

(b) Number Density

Figure 2.7: Comparisons of (a) soot volume fraction and (b) number density for Stanford (—) and KAUST (- - -) mechanisms with increasing mixing time (decreasing scalar dissipation rate) at 1 bar and constant $\tau_{res} = 2$ ms.

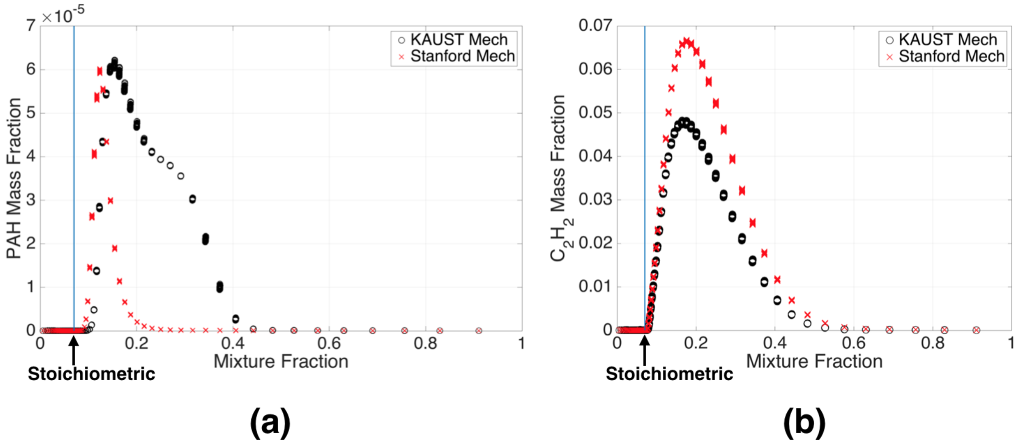

Figure 2.8: Comparison of (a) PAH (naphthalene) and (b) C_2H_2 mass fractions for KAUST and Stanford mechanisms with mixture fraction at 1 bar, $\tau_{res} = 2$ ms and $\tau_{mix} = 0.1$ ms.

Figure 2.9 shows the increase in soot volume fraction and number density with increase in pressure from 1 to 5 bar for both the detailed and acetylene-based models. This increase can be attributed to the increase in PAH mass fraction with pressure in Fig. 2.10.

However, this increase scales differently depending on soot dynamic models, with DQMOM producing higher number density and volume fraction at small mixing times as pressure increases. This is due to numerical stiffness in matrix inversion introduced by the large increase in PAH at small mixing times with increasing pressure. This numerical difficulty can be solved by using another set of moments with a lower condition number. Previous study (*Zucca et al.* (2007)) has reported strategies for selection of DQMOM moment sets to reduce numerical difficulties. For this study, a constant set of optimized moment set is used for consistency.

In a power law fit of soot volume fraction to τ_{mixing}, detailed models have an average $\tau_{mixing}^{5.3}$ scaling at 1 bar to $\tau_{mixing}^{4.6}$ at 2 bar to $\tau_{mixing}^{3.9}$ at 5 bar. SEMI model is relatively insensitive to pressure increase, with soot number density staying constant and volume fraction increasing moderately compared to detailed models. The power

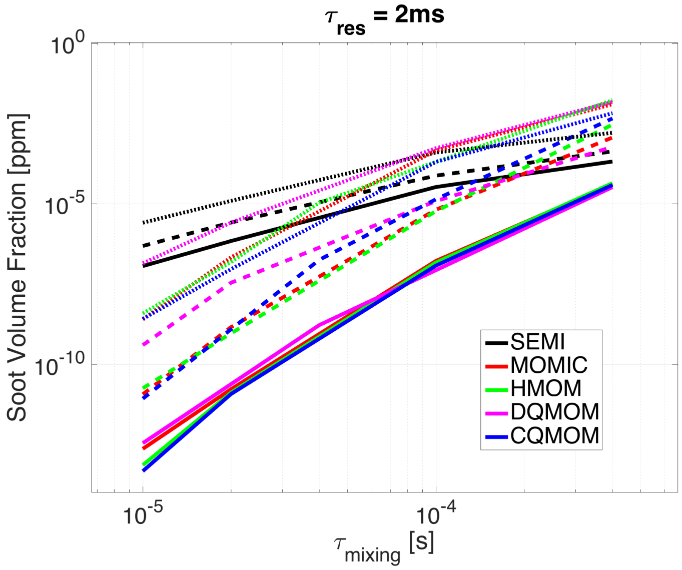

(a) Volume Fraction

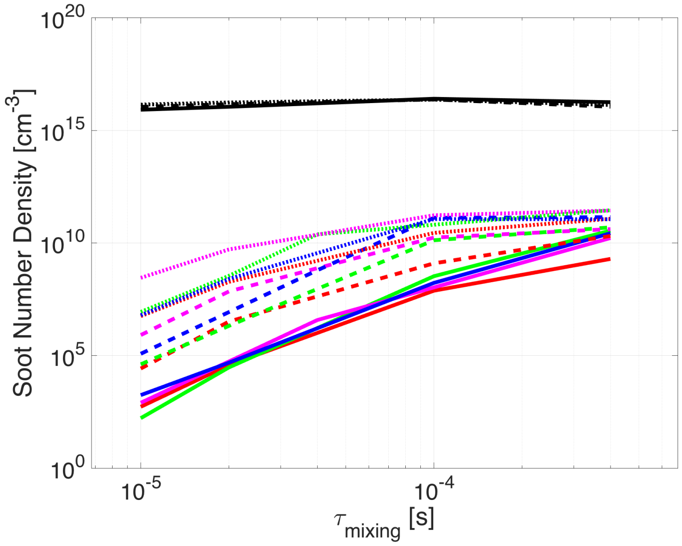

(b) Number Density

Figure 2.9: Comparisons of (a) soot volume fraction and (b) number density for 1 bar (—), 2 bar (- - -), and 5 bar (······) with increasing mixing time (decreasing scalar dissipation rate) using Stanford mechanism at constant $\tau_{res} = 2$ ms.

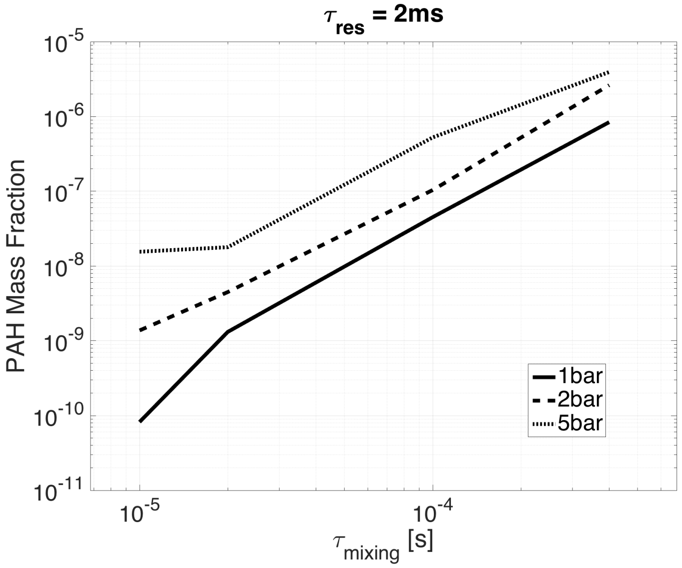

Figure 2.10: Comparison of PAH (naphthalene) mass fraction with increasing pressure at different mixing times. Stanford mechanism is used, with constant $\tau_{res} = 2$ ms.

law fit scaling is relatively moderate for SEMI with $\tau_{mixing}^{2.1}$ scaling at 1 bar to $\tau_{mixing}^{1.9}$ at 2 bar to $\tau_{mixing}^{1.8}$ at 5 bar.

The mixing time is directly correlated to the "unmixedness" of the scalar field through Eq. 2.4 (*Chen* (1997)), a description of the level of scalar mixing in the convection time scale (τ_{res}). "Unmixedness" is thus inversely correlated to the scalar dissipation rate, χ, with smaller mixing time resulting in higher scalar dissipation rate and vice-versa.

$$unmixedness = \frac{1}{1 + \frac{\tau_{res}}{3\tau_{mixing}}} \tag{2.4}$$

Using the above relationship, power law scaling of the soot models show that soot volume fraction becomes less sensitive to scalar dissipation rate as pressure increases from 1 to 5 bar.

2.3.5 Mixing model effect

As mixing models that determine the mixture fraction distribution among the particles differ, Fig. 2.11 shows significant differences in the soot volume fraction. Only MOMIC soot model is used in this study to illustrate the differences in mixing model. MC model significantly underpredicts soot volume fraction compared to IEM and EMST models. At small mixing times, MC model can reproduce soot volume fraction of the more accurate EMST model while IEM model predicts higher soot volume fraction. However, at larger mixing times (smaller $\frac{\tau_{res}}{\tau_{mix}}$ ratios), the difference in soot volume fraction between IEM and EMST model is diminished. The cause for this trend in soot volume fraction is seen in the prediction of temperature for the different mixing models as shown in Fig. 2.11 (b). MC model predicts higher temperatures at all mixing times compared to IEM and EMST models. Initially, at small mixing times where the particles are more well-mixed, EMST model predicts temperature close to MC model. As mixing time increases, the deviation between temperatures for MC model and IEM and EMST models increases to 200 K maximum.

Figure 2.12 illustrate the differences in the temperature - mixture fraction distribution for different mixing models, similar to the distribution described in *Ren and Pope* (2004). For the IEM model, the particles do not all lie close to the equilibrium line, like particles in the EMST model. This inaccuracy in the IEM model is undesired, however, it is a good compromise compared to particles in the MC model that has cold fuel and oxidizer mixing to produce particles that lie inside the reaction zone enclosure. This unphysical behavior of the MC model results in higher temperature predicted and lower soot volume fraction compared to the more accurate EMST and IEM models.

Figure 2.13 shows the effect of different mixing models on the soot volume fraction conditioned on mixture fractions. As a result of the temperature and species mass fraction distribution differences from these three mixing models, the soot volume fractions exhibit large variations with time. The notional particles undergo micro-mixing process at a constant timestep of 0.1 ms, starting from the same initial conditions. The IEM model shows soot volume fraction decreases as the mixture fraction is distributed through the mixing process, eventually reaching a steady state value as shown in Fig. 2.11. The EMST model exhibits a different trend to the IEM model where the particles reach steady state much faster than the IEM model and the higher mixture fraction region soot volume fraction for the EMST model increasing with time. The lower temperature at the mixture fraction below stoichiometric (0.064) for the IEM model produces a bump in the soot volume fraction in Fig. 2.13. This is different to the EMST model where there is no local minima at the stoichiometric mixture fraction region. Comparing EMST and IEM models, the IEM model has a higher soot volume fraction at the fuel lean region that might have an overall effect on simulations of fuel lean-type configurations.

2.3.6 Evolution of soot with scalar dissipation rate

The steady-state soot analysis is important for understanding soot production rate at each operating condition and mixing rates. However, the transient soot and species evolution from the same initial condition can show how soot changes with time before it reaches steady-state. This is particularly useful for mixing-layer cases of high Reynolds number where fuel-rich pockets exist and are transported through a cell with small mixing times.

In Fig. 2.14, from the same initial condition of $\phi = 2.0$, as time progresses from 2 ms to 4 ms to 6 ms, the soot volume fraction and number density (conditioned on mixture fraction) decreases, using the IEM mixing model. Two mixture fractions of lean (Z = 0.06) and rich (Z = 0.25) are shown. This trend shows the mixing process re-distributing the fuel/air mixture, increasing soot oxidation, and is better illustrated in Fig. 2.13 with the IEM mixing model. The EMST model exhibits an opposite trend

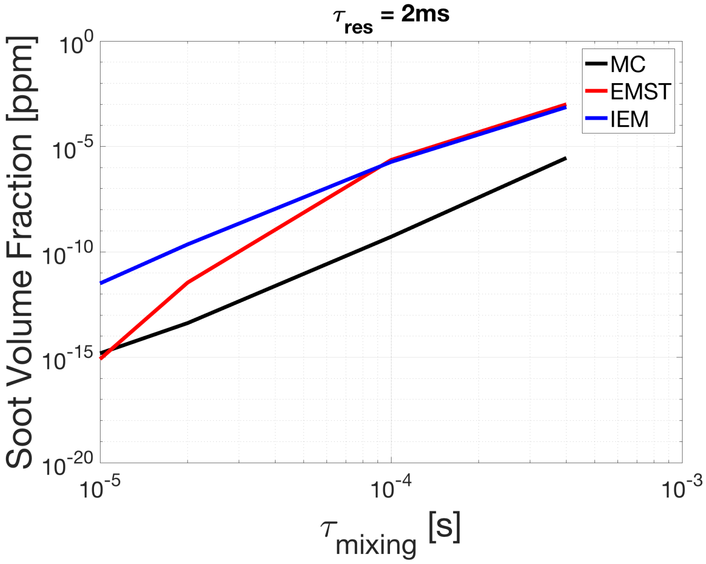

(a) Soot volume fraction

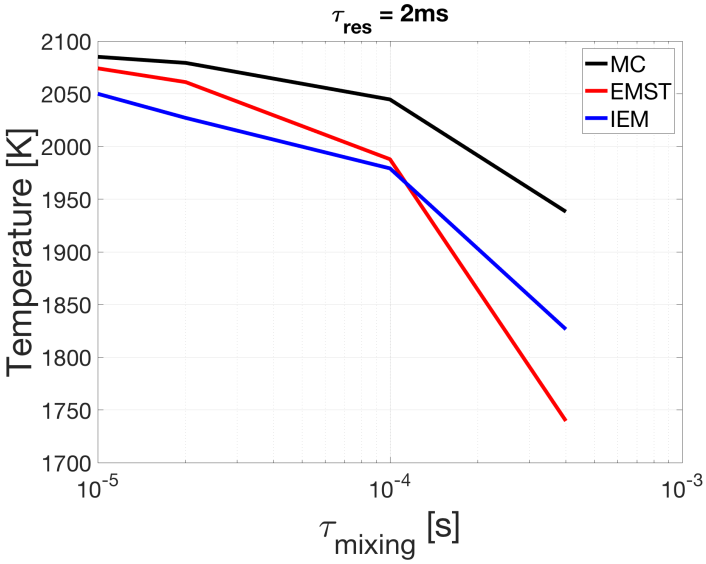

(b) Temperature

Figure 2.11: Comparison of (a) soot volume fraction, and (b) temperature with increasing mixing time at 1 bar pressure for different mixing models Kaust mechanism and MOMIC soot models are used, with constant $\tau_{res} = 2$ ms.

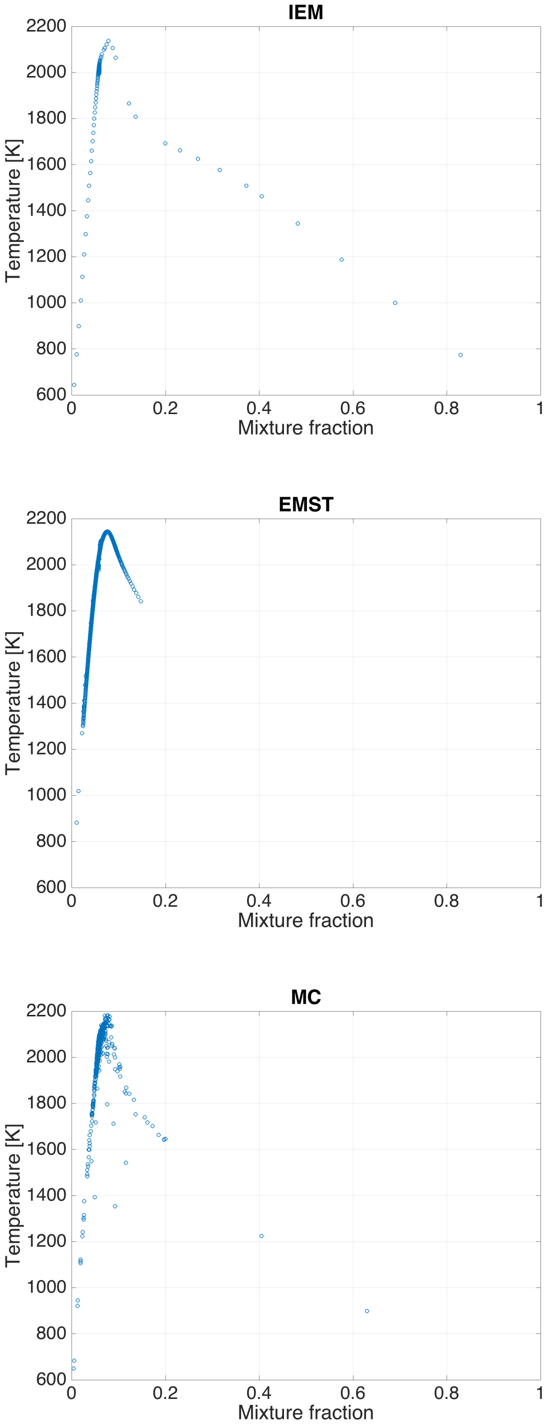

Figure 2.12: Comparisons of temperature - mixture fraction distribution of particles for different mixing models at $\tau_{res} = 2ms$ and $\frac{\tau_{res}}{\tau_{mix}} = 20$.

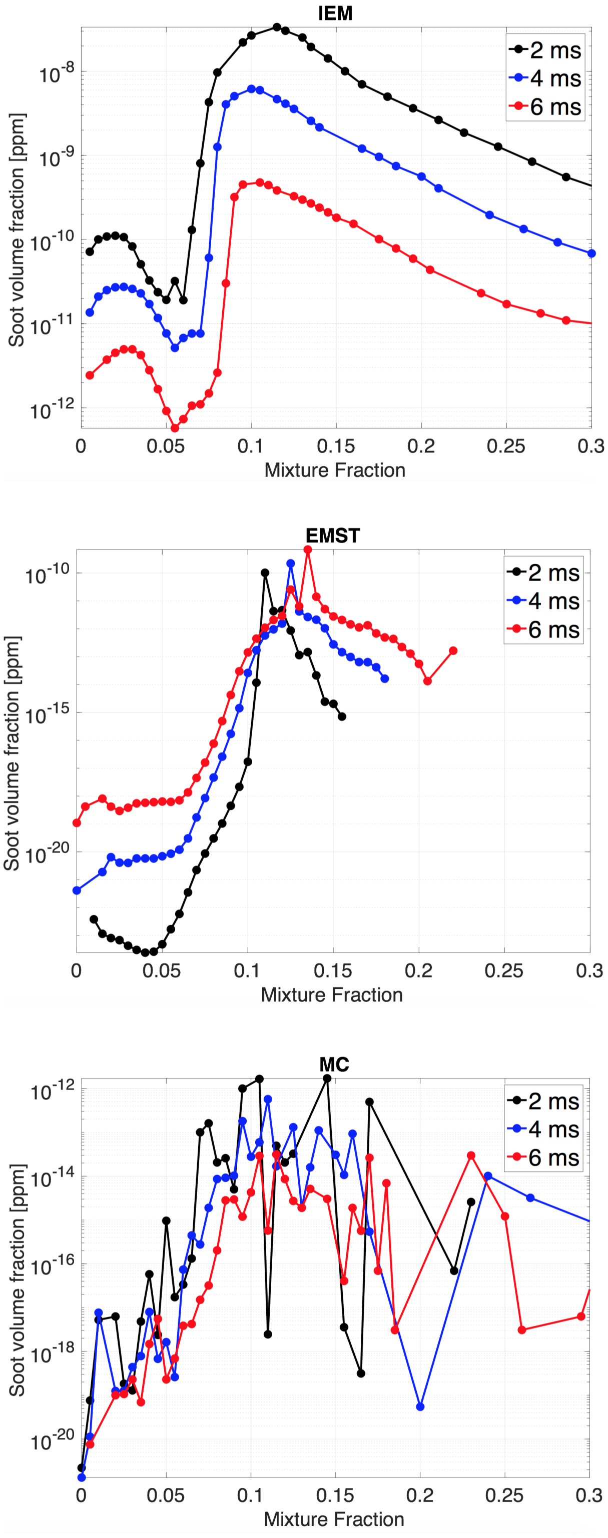

Figure 2.13: Comparisons of soot volume fraction (conditioned on mixture fraction) distribution of particles for different times and mixing models at $\tau_{res} = 2ms$ and $\frac{\tau_{res}}{\tau mix} = 20$, $\phi = 2.0$, MOMIC, with Kaust mechanism.

to the IEM model in that soot volume fraction is produced in a small quantity initially and increases as time progresses. In this regard, turbulent combustion simulations involving complex flows and high equivalence ratio operating conditions (e.g. swirl combustors, *Chong et al.* (2018a)) utilizing the PDF method will be subjected heavily to this difference in mixing model.

Looking at the time evolution of species mass fraction conditioned on mixture fraction in Fig. 2.15, acetylene (C_2H_2) is shown to be less affected by scalar dissipation rate compared to naphthalene ($C_{10}H_8$), which is a PAH species used as the soot precursor in this study. This strong effect by scalar dissipation rate on PAH species is already extensively studied (*Attili et al.* (2014); *Bisetti et al.* (2012)) using DNS and represents a common challenge in the soot modeling community. However, this study shows that without expending significant computational resources, similar highly accurate finite rate calculations can be conducted and extended to a large range of scalar dissipation rates.

2.4 Summary

The effects of chemistry and soot models on soot predictions are studied with PaSR for ethylene/air configuration at stoichiometric condition with different mixing and residence times for 1, 2, and 5 bar pressures. Two chemistry mechanisms and five soot models (acetylene-based and detailed PAH-based models) are comprehensively assessed. Three turbulence mixing models are studied to determine the effect of the pdf of mixture fraction on soot. Last but not least, transient effect on soot prediction and precursor species evolution is also assessed. It is found that:

1. PAH-based detailed soot models scale similarly to soot quantities, in general, with mixing and residence time.

2. Soot statistical model is more important if properties other than soot volume

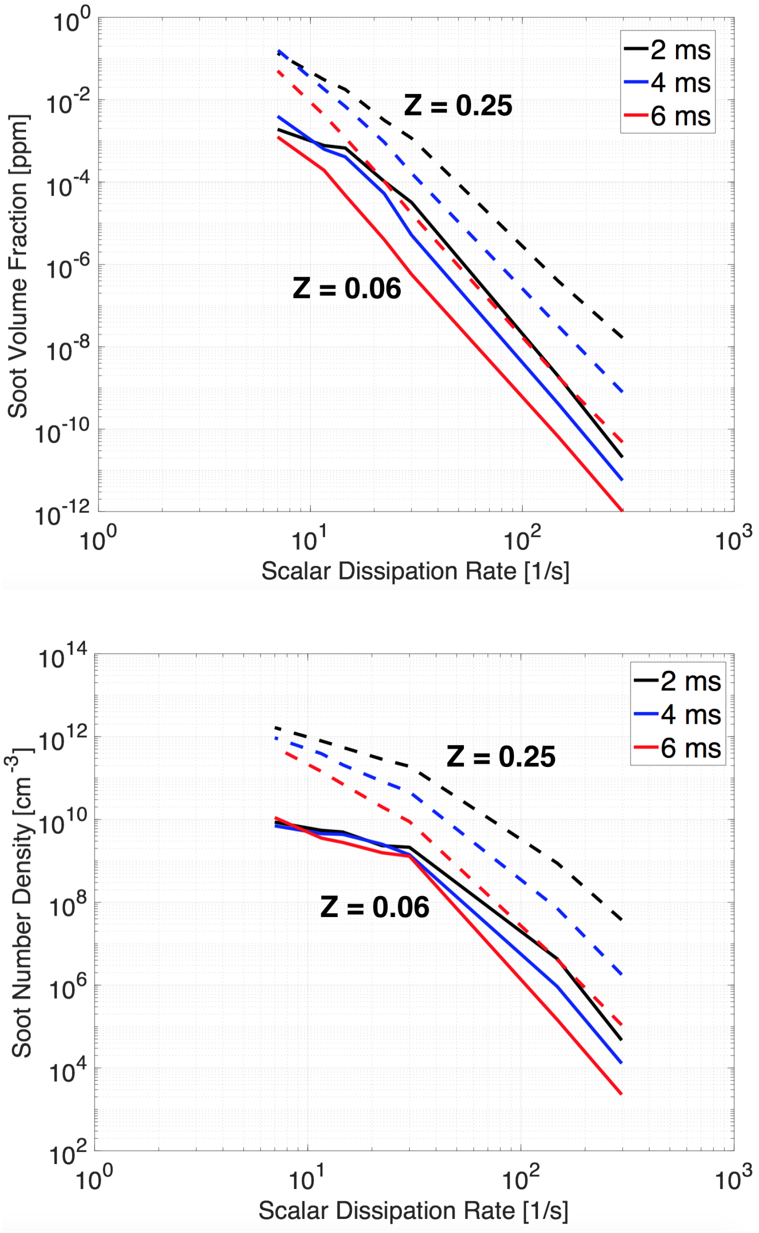

Figure 2.14: Comparisons of soot volume fraction and soot number density (conditioned on mixture fraction = 0.06 and 0.25) for different times and scalar dissipation rate. $\tau_{res} = 2ms$ and $\frac{\tau_{res}}{\tau mix} = 20$, $\phi = 2.0$, MOMIC, with Kaust mechanism, IEM mixing model.

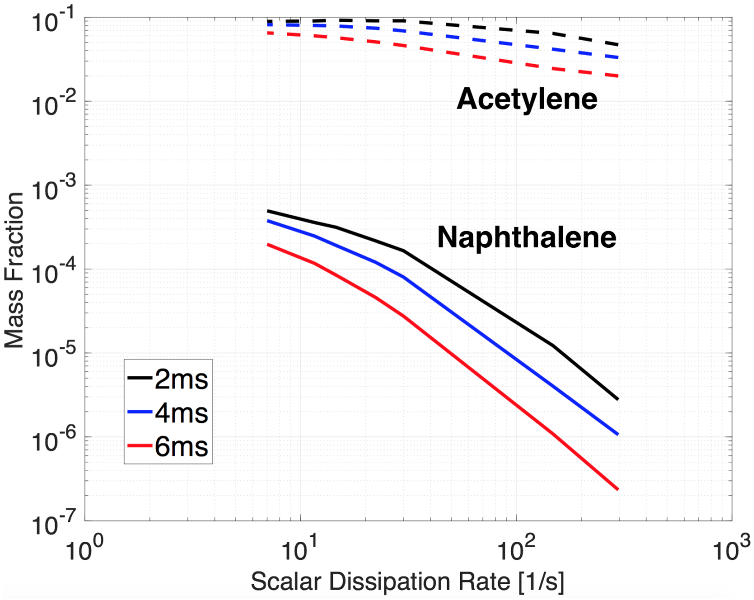

Figure 2.15: Comparisons of species mass fractions (conditioned on mixture fraction = 0.25) for different acetylene and naphthalene at different scalar dissipation rates. $\tau_{res} = 2ms$ and $\frac{\tau_{res}}{\tau_{mix}} = 20$, $\phi = 2.0$, MOMIC, with Kaust mechanism, IEM mixing model.

fraction is needed because MOMIC predicts larger particle diameters at lower number density but produces similar volume fraction compared to the other statistical models.

3. Comparison between the two quadrature-based method of moments (CQMOM and DQMOM) also shows slight differences between the two methods in the evolution of weight and abscissas despite predicting similar soot properties.

4. KAUST mechanism consistently predicts higher soot volume fraction and number density regardless of soot dynamic model and pressure, due to higher PAH concentrations.

5. From power law scaling of soot volume fraction to mixing time, the detailed soot models show that soot volume fraction is less sensitive to scalar dissipation rate as pressure increases from 1 to 5 bar.

6. Soot volume fraction using SEMI model is less sensitive to mixing and residence

time compared to detailed soot models. Soot number density for SEMI model is relatively constant with mixing time, mechanism, and pressure changes.

7. MC mixing model is shown to significantly underpredict soot volume fraction for a large range of mixing times due to the unphysical behavior of mixture fraction PDF.

8. IEM mixing model produces much lower soot volume fraction at stoichiometric mixture fraction, in contrast to the EMST and MC mixing models, mainly due to differences in temperature and species concentrations for the different mixing models.

2.5 Large Scale Soot-Turbulence-Chemistry Interactions

Section 2.1 studies the soot-turbulence-chemistry interactions at a smaller scale that imposes turbulence time scales with the ability to switch chemistry mechanisms and soot model with ease. With this background, the goal of this section is to understand the sensitivity of soot predictions to the choice of chemistry model and moment approach for a 3D large scale simulation - a model aircraft combustor. It is of interest to investigate how the different soot chemistry models perform in turbulent flame simulations involving more complex flow-chemistry interactions. The study is based on the DLR ethylene/air combustor (*Geigle et al.* (2015)), which is comparable in design to a rich-quench-lean (RQL) type combustor used for aircraft propulsion. This combustor has also been studied using specific methods in the past (*Eberle et al.* (2014); *Wick et al.* (2017b); *Chong et al.* (2018a); *Koo et al.* (2017)), which will provide additional bases for comparison. Here, three different soot inception models and three different soot description approaches are compared with experimental data. In modeling complex combustors, LES has been shown to be accurate for predicting the reacting flow field (*Mueller and Pitsch* (2013); *Raman and*

Fox (2016)). With this basis for turbulence modeling, three additional components are required for modeling soot evolution: a) a turbulent combustion model to describe the interactions between turbulence, gas-phase chemistry, and molecular transport; b) a chemical kinetics model that links gas-phase combustion and soot precursor evolution to soot evolution through nucleation, condensation and surface growth; and c) a soot population balance model and solution methodology that allows nanoparticles to be represented in a computationally tractable manner. Prior studies have shown that for flames that are not close to extinction, different combustion models produce comparable results (*Donde et al.* (2013); *Raman and Pitsch* (2005)). Therefore, the focus here will be on the latter two modeling components mentioned above (*Chong et al.* (2018c)).

2.6 Configuration and Computational Approach

2.6.1 DLR experimental combustor

The model swirl combustor configuration used in this study is based on the high-pressure combustor of *Geigle et al.* (2015). A planar slice of the geometry and the computational mesh are shown in Fig. 2.16. A total of 12 million control volumes are present in the computational domain. The cross-sectional area of the square combustor is 68 × 68 mm^2, with a height of 120 mm. The inflow consists of three concentric nozzles: two air inlets with swirling velocity and 60 annular straight-channel fuel (C_2H_4) inlets (0.5 × 0.4 mm^2 each), located in between the two air inlets. A constricted nozzle of diameter 40 mm serves as the combustor outlet.

In this study, the specific case in Table 2.1 is simulated. The global equivalence ratio is 1.2, and the slight fuel rich condition could produce high volumes of soot if fuel-air mixing is inefficient. Therefore, the soot particles observed are generated due to local mixing inefficiencies. Further details about the configuration, computational domain, grid refinement process, and the statistical averaging process can be found in *Geigle et al.* (2015); *Chong et al.* (2018a); *Koo et al.* (2017); *Chong et al.* (2018b).

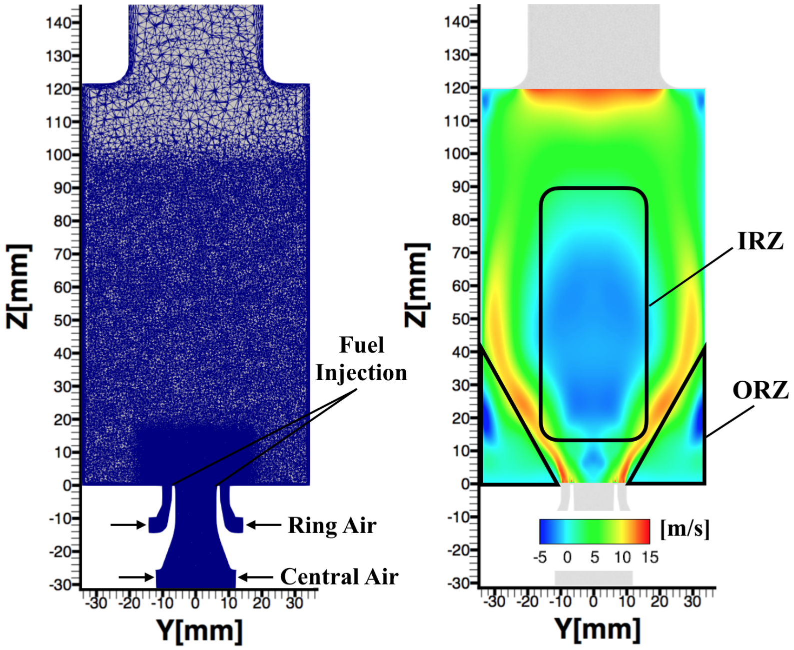

Figure 2.16: (Left) DLR combustor geometry center cut-plane and mesh refinement with fuel and air inlets indicated. (Right) Time-averaged axial velocity with inner recirculation zone (IRZ) and outer recirculation zone (ORZ) indicated.

Pressure (bar)	Q_{fuel} (slpm)	$Q_{central\ air}$ (slpm)	$Q_{ring\ air}$ (slpm)	ϕ
3	39.3	140.8	328.5	1.2

Table 2.1: Flow parameters and operating conditions for the simulated case. Flow rates referenced at 1.013 bar and 273 K.

2.6.2 LES approach for sooting flames in complex geometries

To simulate turbulent combustion, the LES approach is combined with the radiation flamelet/progress variable (RFPV) approach with a heat loss parameter, H, which accounts for radiation effects from the gas species and soot particles (*Mueller and Pitsch* (2012)). Further details on the implementation are provided in Section 1.3.

These models are implemented in OpenFOAM (ope (2017)), with modifications to ensure minimal energy dissipation and higher-order temporal accuracy (*Hassanaly* *et al.* (2018)). This solver has previously been applied to simulating complex reacting flows (*Chong et al.* (2018a); *Koo et al.* (2016a)). Dynamic models were used for all subfilter quantities (*Moin et al.* (1991)).

In this study, two variations in model components are considered: the chemical kinetics mechanism and the soot statistical description, the latter also having a variation in the soot inception model. The different models are described below.

2.6.2.1 Chemical kinetics for soot formation

The two chemistry mechanisms are selected based on the accuracy of predicting soot precursors: (a) *Narayanaswamy et al.* (2010) (NBP hereinafter), and (b) KAUST-Aramco PAH Mech.1.0 (*Metcalfe et al.* (2013)) (KAM1.0 hereinafter). Both mechanisms include detailed PAH chemistry. The NBP mechanism includes PAH chemistry up to four aromatic rings (pyrene), and the KAM1.0 mechanism includes PAH chemistry up to seven aromatic rings (coronene). Both mechanisms have been validated against canonical laminar flames (*Blanquart et al.* (2009); *Mueller et al.* (2009); *Selvaraj et al.* (2016)).

2.6.2.2 Soot statistical description

To statistically model the soot NDF, three statistical approaches are considered, all based on methods of moments: a) semi-empirical, b) Hybrid Method of Moments (HMOM) and c) Conditional Quadrature Method of Moments (CQMOM). These models are explained in Section 1.2

2.6.3 Simulation cases

Based on the above description, six different simulations were conducted for the DLR combustor operating at 3 bar pressure. A set of three simulations using semi-empirical, HMOM, and CQMOM approaches for the NBP mechanism and another set of the same statistical models with the KAM1.0 mechanism. The simulations were run for 20 flow-through times until the soot statistics converged. The source terms for the semi-empirical model were based on the acetylene concentration from the individual kinetic mechanisms used. A flamelet library with necessary species mass fractions and source terms was generated for each mechanism and tabulated in $\widetilde{Z}, \widetilde{C}, \widetilde{Z''^2}, \widetilde{H}$ coordinates, where $\widetilde{\cdot}$ refers to the LES filtering operation and $\widetilde{Z''^2}$ refers to the subfilter variance of mixture fraction.

2.7 Results

Figure 2.17 shows the time-averaged temperature, mixture fraction, and PAH concentration for the CQMOM method using the NBP mechanism. Due to the strong swirling inflow, fuel-air mixing is nearly complete within a short distance downstream of the fuel injection ports. Consequently, the temperature field is nearly uniform beyond $Z = 30$ mm. The mixture fraction field shows the presence of two shear layers, with high mixture fraction values confined to these regions that denote the boundaries of the IRZ and ORZ in Fig. 2.16. Moreover, there are small regions of rich mixture fraction further downstream caused by the recirculating flow in the IRZ. The PAH concentrations peak at this location but form a broad high value zone near the base of the combustor. Overall, the agreement for flow field velocity and gas-phase thermodynamic quantities are very good, and has been studied extensively in prior work (*Chong et al.* (2018a)).

The key results of the time-averaged soot volume fraction and number density are shown in Figs. 2.18-2.20. Several observations are noted. The semi-empirical model, with an acetylene-based inception model, predicts much of the soot mass to be in the IRZ, which tends to be slightly fuel rich for this case and supports large concentrations of acetylene but little PAH. Similar large soot volume fractions in the IRZ have been found by *Katta et al.* (2005) using a semi-empirical soot model for

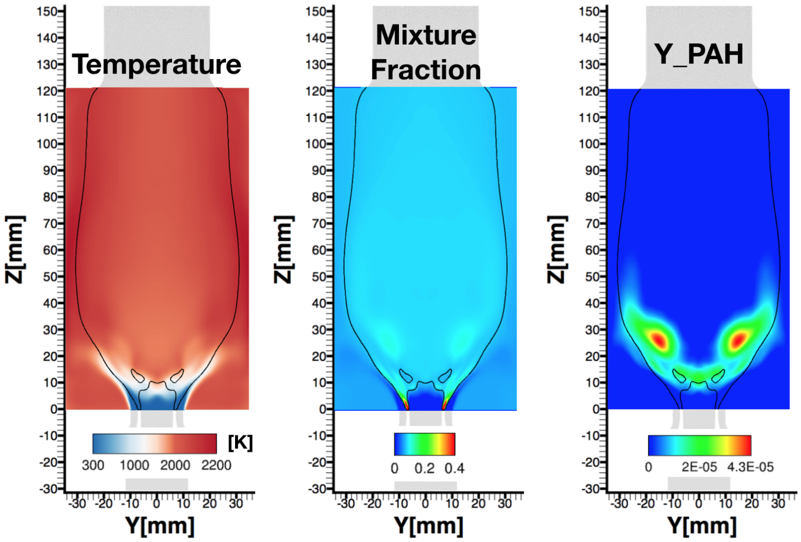

Figure 2.17: Time averaged temperature, mixture fraction, and PAH mass fractions, lined with stoichiometric mixture fraction for the NBP mechanism and CQMOM model.

a swirl combustor at $\phi = 1.15$ and JP-8 fuel. In the IRZ, the semi-empirical model predicts an approximately constant level of soot volume fraction. Conversely, the other soot models utilize PAH-based inception and predict soot formation primarily in the shear layers that separate the IRZ and ORZ. The fuel jets that enter from the annular ring provide this extremely fuel-rich region that supports large PAH concentrations. In addition, since PAH is highly sensitive to strain rate (*Bisetti et al.* (2012)), the soot formation in this shear layer exhibits high intermittency due to turbulence-induced fluctuations in the local strain rate (*Chong et al.* (2018a); *Koo et al.* (2017); *Raman and Fox* (2016)). The soot models differ in the growth pathways and their dependence on mixture fraction. Hence, if the mixture fraction, for which there is no experimental data, is incorrect in the IRZ, then the soot volume fraction could be predicted incorrectly. The oxidation rates are unmodified from values in the literature for both the SEMI and detailed models. However, the presumed subfilter PDF model used with the detailed chemistry model could also lead to overprediction of the oxidation rate in the IRZ (isf (2016)).

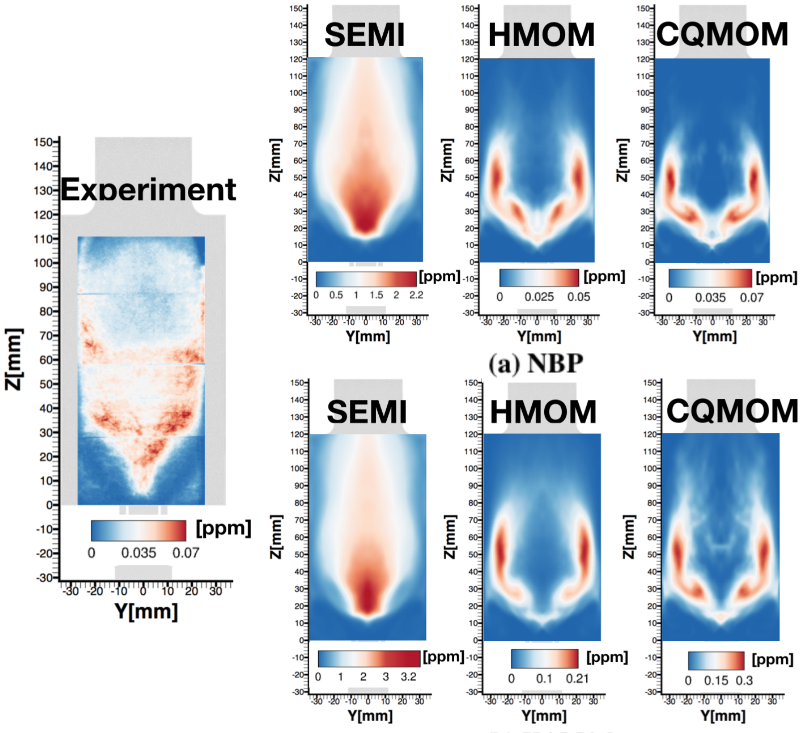

(a) NBP

(b) KAM1.0

Figure 2.18: Time-averaged soot volume fraction contours for the experimental measurement (left) and the different soot and moment description models.

Quantitative comparisons with experimental data are shown in Fig. 2.19, where the radial distribution of the soot volume fraction is shown at three different axial locations. It is evident that the three models yield significant differences. At upstream locations, the experiments show a peak in soot volume in the IRZ, which is consistent with the semi-empirical model, although it is overpredicted by an order of magnitude. At downstream locations, soot peaks are shifted further to the shear layer regions, which is qualitatively reproduced by the PAH-based models. Between the two detailed soot chemistry mechanisms, the use of the KAM1.0 mechanism increases soot volume fraction by approximately a factor of four. However, neither chemical model agrees with the experimental measurements any better than the other, but the KAM1.0 model does provide persistent soot further downstream compared to the NBP model in agreement with the experimental measurements. CQMOM predicts soot volume fractions up to twice as large as HMOM, especially upstream.

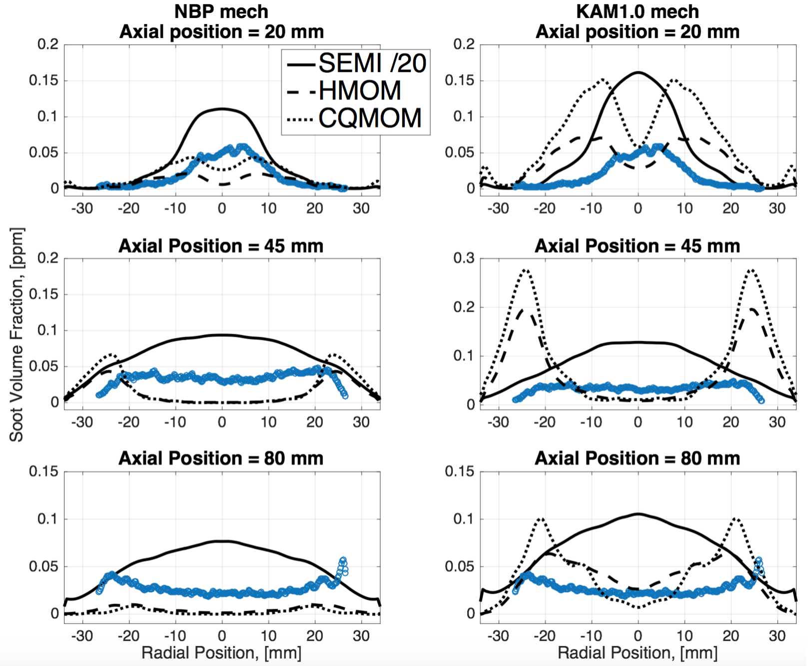

Figure 2.19: Comparisons of time-averaged soot volume fraction with experimental data (blue scatter) for all mechanisms and soot models, at various axial positions in the combustor.

As shown in Fig. 2.18, HMOM and CQMOM produce qualitatively similar soot volume fractions with either mechanism, differing by up to a factor of two. This can be better understood through the number density contours shown in Fig. 2.20. CQMOM predicts number density significantly larger than HMOM. Since the soot inception models are the same, the only explanation for the difference in number density is due to coagulation, with HMOM predicting a faster rate of coagulation. Since coagulation reduces the surface area (*Mueller et al.* (2009)), HMOM has less surface area, less surface growth, and subsequently a smaller volume fraction compared to CQMOM. The semi-empirical model predicts a considerably larger number density than either HMOM or CQMOM consistent with the volume fraction. This indicates that the soot inception rate is much larger for the acetylene-based inception model than the PAH-based inception model.

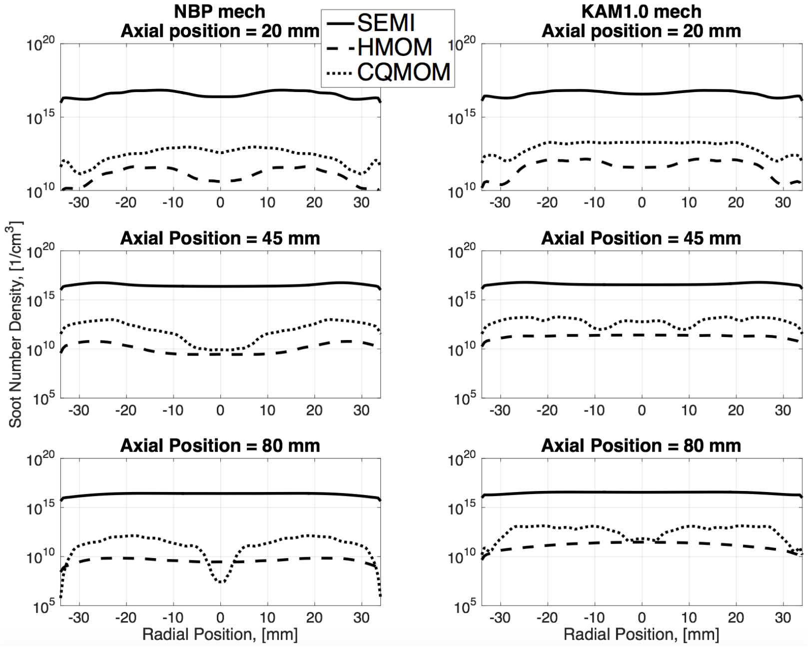

Figure 2.20: Comparisons of time-averaged soot number density for all mechanisms and soot models, at various axial positions in the combustor.

Figure 2.21 shows the comparison of the primary particle diameter for the CQMOM and HMOM models at two different axial locations in the combustor and confirms the observations above. The average primary particle diameter is considerably

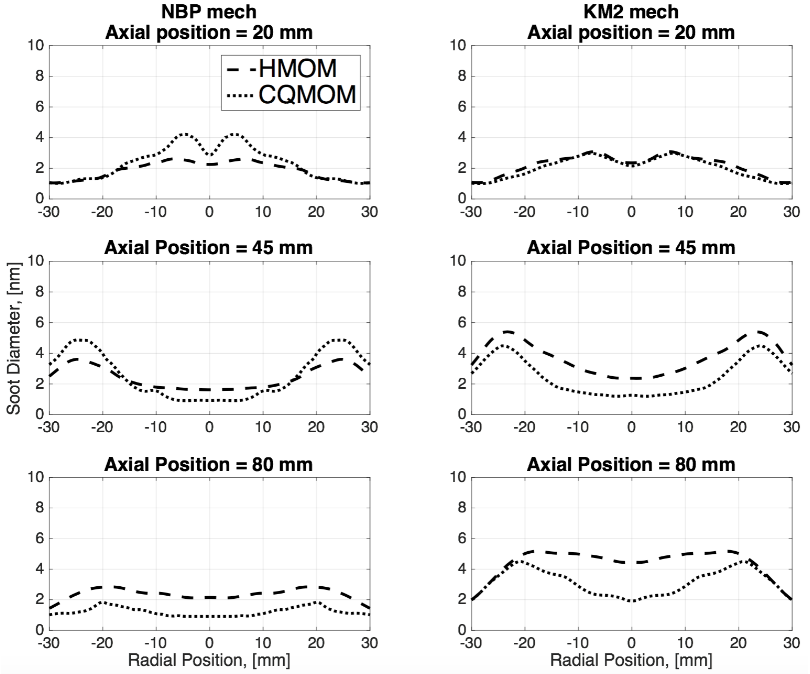

Figure 2.21: Comparison of time-averaged soot primary particle diameter for HMOM and CQMOM models at various axial positions in the combustor.

larger with HMOM, indicating an increased rate of coagulation. This is independent of the chemical mechanism used.

The change in the chemical mechanism from NBP to KAM1.0 consistently increases soot volume fraction for all the soot models considered, consistent with previous studies in laminar flames (*Selvaraj et al.* (2016)). While the qualitative volume fraction profiles are the same, there is 50-200% increase in soot volume fraction. This is consistent with the prediction of acetylene (C_2H_2) concentration and the PAH concentrations, which are higher with KAM1.0 compared to the NBP mechanism. The difference is due presumably to the base chemistry, with KAM1.0 validated for only C_0-C_2 and NBP for C_0-C_8. In addition to the base chemistry, the PAH growth pathways also vary between the mechanisms. In KAM1.0, PAH growth continues beyond pyrene and the growth is largely due to acetylene addition to PAH radicals. In NBP, PAH growth stops at pyrene but includes more detailed pathways including the effects of C_3 (propargyl), C_5 (cyclopentadyenyl), C_7 (benzyl), and C_9 (indenyl) radical species.

To conclude the discussion of these differences, the source terms for the volume moment $M_{1,0}$ are plotted in Fig. 2.22 for the CQMOM simulations. As expected, nucleation dominates near the base of the flow, in the region adjacent to the shear layers within the IRZ. Condensation is similarly distributed. However, surface growth is the most dominant source of soot mass, extending from the shear layer into the IRZ. In fact, even near the base of the flow, higher acetylene concentrations lead to increased surface growth rates. Oxidation is roughly collocated with the surface growth region, on the fuel-lean side of the stoichiometric location that cuts across the shear layer. The two kinetic mechanisms produce vastly different nucleation and condensation rates, differing by an order of magnitude at certain locations. Despite this difference, the dominant role of surface growth reduces the disparity in the final soot volume fractions generated by these mechanisms (Fig. 2.18). Furthermore, the dominance of surface growth, which depends strongly on the soot surface area and coagulation dynamics, indicates that coagulation can be extremely important for dictating the soot volume fraction in turbulent combustion. Therefore, high-fidelity closures for soot-turbulence interactions are required and will have leading-order impacts on the soot volume fraction.

2.8 Summary

LES computations to understand effects of the chemical mechanism and soot statistical model on soot predictions were conducted. Two different kinetic mechanisms (NBP, KAM1.0) and three different statistical approaches (semi-empirical, HMOM, CQMOM) were considered. The simulations yielded the following conclusions for the models considered.

- The use of acetylene-based inceptions leads to significantly higher soot volume fraction compared to the experiments or the PAH-based inception models. How-

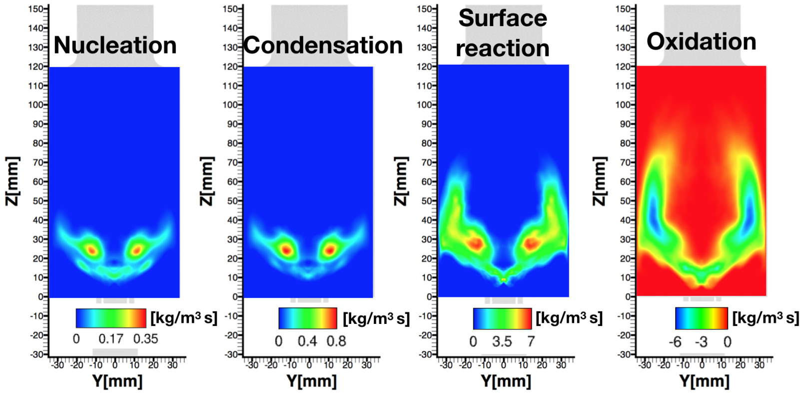

(a) CQMOM/NBP

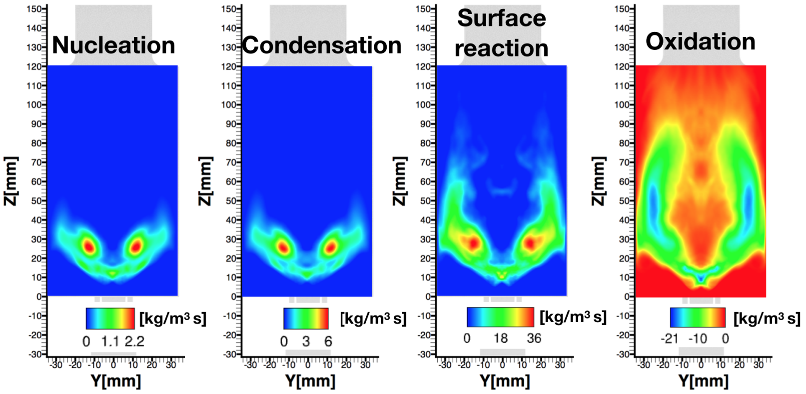

(b) CQMOM/KAM1.0

Figure 2.22: Time-averaged soot source terms using CQMOM approach for the the NBP and KAM1.0 mechanisms.

ever, this approach also generates significant soot mass in the IRZ of the swirl combustor, which is consistent with the experimental data. The PAH-based nucleation models tend to generate soot in the shear layers, where rapid changes in strain rate lead to intermittency in soot inceptions.

- The different statistical approaches generate different soot number density, indicating significant differences in the handling of the NDF. The semi-empirical model produced very high number density and soot mass yield. The CQMOM simulations show significantly higher number density compared to HMOM, although the final soot yield is comparable. The CQMOM particle diameter is correspondingly smaller, and the difference is attributed to a faster rate of coagulation predicted with HMOM.

- The KAM1.0 mechanism produces more soot mass compared to the NBP mechanism for all statistical approaches considered, which is consistent with laminar flame results (*Selvaraj et al.* (2016)). While the nucleation and condensation source terms are much higher with KAM1.0 compared to NBP, the final soot mass fraction changes by less than a factor of two. In the combustor, surface growth through acetylene-driven HACA mechanism dominates over other processes such as nucleation or condensation in adding soot mass. As a result, even with the large variations in these rates for the two kinetic mechanisms, the final soot yields are comparable. However, the dominance of surface growth accentuates differences in the coagulation rates predicted by the statistical models.

This study demonstrates that soot predictions are sensitive to the choice of all models involved, and care must be taken in interpreting the results. From an uncertainty standpoint, the changes in soot predictions with such model changes should be incorporated (*Mueller and Raman* (2014)). Improvements to the statistical approaches that can ensure numerical convergence of the moments approach will be useful for ensuring reliability of the predictions. In this sense, other solution techniques (*Sewerin and Rigopoulos* (2017); *Marchisio and Fox* (2013)) show promise and should be further investigated. From a physics standpoint, the performance of such models in combustors where nucleation/condensation dominate soot mass would be interesting, and the hypothesis is that differences due to chemical mechanisms would be larger but differences due to statistical models smaller.

CHAPTER III

Hydrodynamic Scaling on Soot in Pressurized Turbulent Sooting Flame

3.1 Introduction

The focus of the current study is to simulate the DLR configuration at higher operating pressures of 3 and 5 bar. For each of these conditions, simulations with and without sidejet injection were considered. The objective is to understand the relative importance of different physical and chemical processes that lead to soot generation, evolution, and destruction. The rest of the sections are laid out as follows. First, in Sec. 3.2, the experimental configuration and operating conditions are discussed. Next, in Sec. 3.3, the models and computational tools are described, followed by details of the numerical approach. The results of the simulations and an analysis of the comparison with experiments are provided in Sec. 3.4. Specifically, effects of sidejet and pressure are analyzed and comparisons of current soot scaling with canonical laminar flames (*McCrain and Roberts* (2005)) is performed. Finally, a summary of findings is presented in Sec. 3.5. Details of the fully unstructured mesh with refinement at the inlet and the grid convergence are shown in Appendix 3.4.4. Temporal convergence of flow and soot statistics are presented in Appendix 3.4.5.

3.2 Experimental Configuration

The ethylene-based DLR model aircraft combustor configuration is shown schematically in Figure 3.1, adapted from *Geigle et al.* (2015). The main combustion chamber measures 120 mm in height and has a square section of 68×68 mm^2. The inlet oxidizer air is introduced in two streams, through a central nozzle with a diameter of 12.3 mm and a ring injector with inner and outer diameters of 14.4 mm and 19.8 mm. The inflow consists of an intricate set of swirlers to inject the oxidizer jets with tangential velocities. The fuel ports consist of 60 straight channels (fuel port area = 0.5×0.4 mm^2) which are located between these two oxidizer streams. A set of injector ports are located on the posts at the height of 80 mm that radially introduce secondary air similar to the rich-quench-lean design for aircraft combustors.

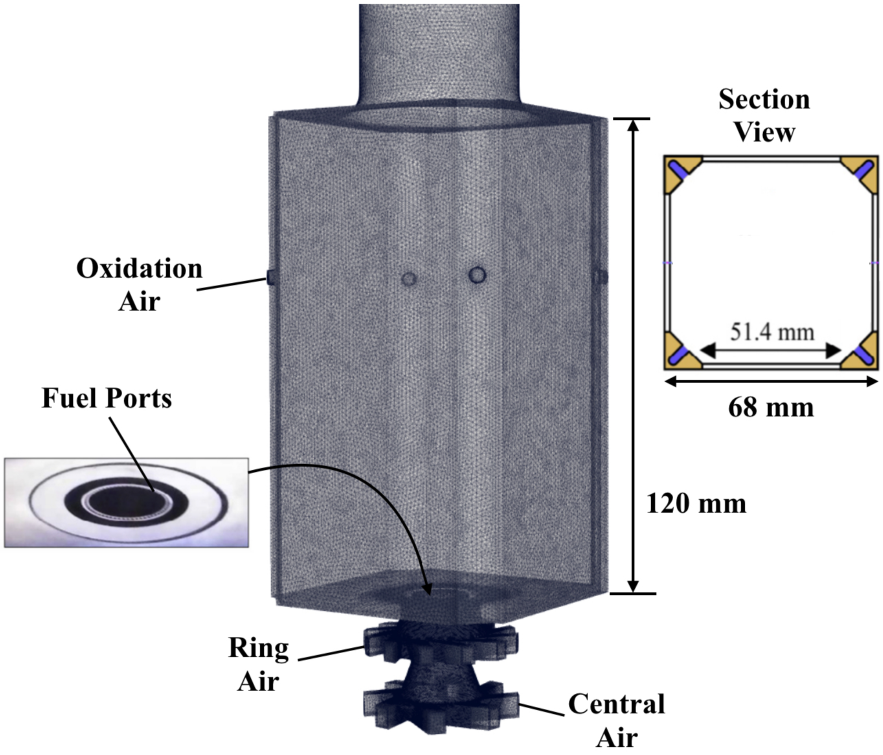

Figure 3.1: Combustor geometry and computational unstructured mesh (12 million cells), inlet nozzle details, and planar cross sections at the height of secondary oxidation air injectors.

Pressure (bar)	$Q_{air,c}$ (slpm)	$Re_{air,c}$	$Q_{air,r}$ (slpm)	$Re_{air,r}$	Q_{fuel} (slpm)	Q_{oxi} (slpm)	Re_{tot}	ϕ_{global}
3	140.8	17,800	328.5	16,500	39.3	0	40,800	1.2
3	140.8	17,800	328.5	16,500	39.3	187.4	40,800	0.86
5	234.2	29,600	546.2	27,500	65.4	0	67,800	1.2
5	234.2	29,600	546.2	27,500	65.4	312.1	67,800	0.86

Table 3.1: Flow parameters and operating conditions for the simulated cases. *air,c* and *air,r* indicate central air and ring air respectively. *oxi* indicates the dilution jet air. ϕ_{global} indicates global equivalence ratio. Standard flow rates are referenced to 1.013 bar and 273 K. ρ_{air} and ρ_{fuel} are 1.18 kg/m^3 and 1.15 kg/m^3 respectively at 1 bar inlet operating conditions. (*Geigle et al.* (2014))

The four different cases discussed in this work correspond to flow conditions provided in Table 3.1. Comparisons of 3 and 5 bar pressures with equivalent inlet fuel and oxidizer velocities are studied in this work. Moreover, comparisons with and without secondary oxidation air are also discussed. The ratio of mass flow rate between the central and ring air inlets was fixed at 3/7. However, the velocities of all the streams are constant for the different pressure cases, which implies that the jet-exit strain rates do not change, but the Reynolds number increases with pressure. This retains the integral time scale that controls residence time in the reactor but reduces the small-scale mixing time scale. Further details about the experimental configuration and measurement techniques are provided in *Geigle et al.* (2014, 2015, 2017). The soot laser-induced incandescence (LII) measurement uncertainty is declared to be 30 %, temperature coherent anti-Stokes Raman scattering (CARS) measurement uncertainty is 5 %, and velocity particle image velocimetry (PIV) measurement uncertainty for the conditions studied are difficult to evaluate because they are strongly dependent on the location in the combustor and (instantaneous) interferences of other effects.

3.3 Model Details

The DLR swirl combustor is simulated using the LES approach. The gas-phase combustion is described using a radiation flamelet/progress variable (RFPV) approach described in Section 1.2.5.

The HMOM approach described in Section 1.2.3.5 is used to solve the bivariate population balance equation.

The LES equations for soot moments and scalar fields are implemented in OpenFOAM (ope (2017)), an operator-based C++ code for solving partial differential equations, which has been applied to a number of combustion systems (*Chapuis et al.* (2013); *Koo et al.* (2016a); *Lietz et al.* (2014b)). However, the baseline codebase had to be substantially modified to ensure accurate evolution of the LES equations. Due to the low speeds within the combustor, a low-Mach number assumption is used, which requires solution of a pressure Poisson equation at each time-step (*Kim et al.* (1987)). It decouples the influence of pressure on the energy field. In the original solver, when primary variables such as mass and momentum are conserved, derived quantities such as kinetic energy may not be conserved in the limit of zero viscosity because it is not evolving according to a conservation equation that is solved. In structured-grid solvers that use staggered positioning of velocity and pressure variables, secondary conservation can be ensured by specific choice of divergence and gradient operators (*Desjardins et al.* (2008); *Ferziger and Peric* (2002); *Mahesh et al.* (2004)). In fully unstructured mesh solvers, such as the one used here, a collocated variable approach is used, which prevents exact secondary conservation of kinetic energy. Minimally dissipative schemes are sought in order to reduce the effect of kinetic energy loss on flow evolution. Here, the variable density scheme of *Morinishi et al.* (1998) is used. The fluxes at the cell faces are computed using a second-order interpolation scheme. The governing equations are solved using a semi-implicit approximation that is second-order in time. This approach directly relates energy conservation to temporal convergence of the numerical scheme. To ensure second-order accuracy, a PISO (pressure-implicit second order) scheme is used (*Issa* (1985)) with at least two inner iterations. These specifications were found to reduce numerical dissipation (*Koo et al.* (2016a)). This variable density solver, umFlameletFoam (*Lietz et al.* (2014b); *Lietz and Raman* (2015); *Koo et al.* (2016a)) is used for all the simulations discussed below and more details can be found in *Hassanaly et al.* (2018).

The flamelet library was constructed separately for each pressure, and soot source terms related to nucleation, surface growth, condensation, and oxidation were parameterized in terms of the rate coefficients and stored (*Mueller and Pitsch* (2012)). The progress variable source term scales approximately as $P^{0.65}$ (P is defined as the pressure), while the dimer production rate, which is a direct indicator of soot nucleation rate, scales approximately as $P^{1.57}$. Other soot related source terms have nearly linear increase with pressure.

3.4 Results and Discussion

In this section, the simulation results for the various cases are discussed. First, the gas-phase flow field is described, followed by description of sooting process in the combustor. Then, gas-phase and soot statistics are compared with experimental results and cause of deviations discussed. Finally, sidejet and pressure effects on soot are analyzed.

3.4.1 Qualitative description of the swirling flow

To understand the overall flow structure in the combustor, instantaneous snapshots from the different simulations are discussed here. For the cases computed at 3 bar pressure with and without sidejets, the flow field information is shown in Figs. 3.2 and 3.3. Similar to rich-quench-lean designs for gas turbines, the combustion zone is aerodynamically stabilized by a swirling flow in the near-field of the injector nozzle

(Fig. 3.2). This creates an inner recirculation zone (IRZ), characterized by negative axial velocities over the center flow injection plane, and an outer recirculation zone (ORZ), located between the shear-layers formed by the fuel injectors and the side walls. When sidejets are present (Fig. 3.3), strong cross-flow mixing is introduced, with the sidejets creating a disruption to the axial flow. The resultant recirculation zone in the middle of the combustor is much stronger compared to the case with no sidejets. In fact, the presence of the sidejets leads to a high velocity zone right next to the side walls, which further isolates the fluid within the IRZ. Similarly, there is a strong acceleration in the axial flow at the exit of the domain, where the constriction of the dump combustor combined with increased flow rate from the sidejets lead to an increase in outflow velocity. While the overall flow structure might look similar, these subtle variations due to the presence of the sidejet, combined with the associated increase in oxidizer mass flow into the combustor, will lead to substantial changes in species and soot profiles (discussed below).

Figure 3.4 shows the instantaneous mixture fraction and temperature plots for 3 bar cases. The swirling inflow significantly augments mixing between the fuel and oxidizer streams. In the case without sidejets, this leads to near uniform mixtures short distance from the inflow. However, there is significant fluctuation in the mixture fraction profile upstream. In particular, it was found that the jets tend to exhibit large scale unsteadiness. Since this jet motion affects soot formation, it is useful to discuss this in more detail. Figure 3.5 shows the instantaneous location of the fuel jet arm at different times. It is seen that during certain time instances, the jet is deflected towards the IRZ, while at other times, the jet is directed away towards the ORZ. This occurs primarily due to the unsteadiness of the recirculation zone itself, which both precesses in the azimuthal direction and undergoes significant size and shape changes throughout the simulation period. The net effect is the dislodging of rich fuel mixtures from the jet into the recirculation zone. Hence, there exists significantly rich

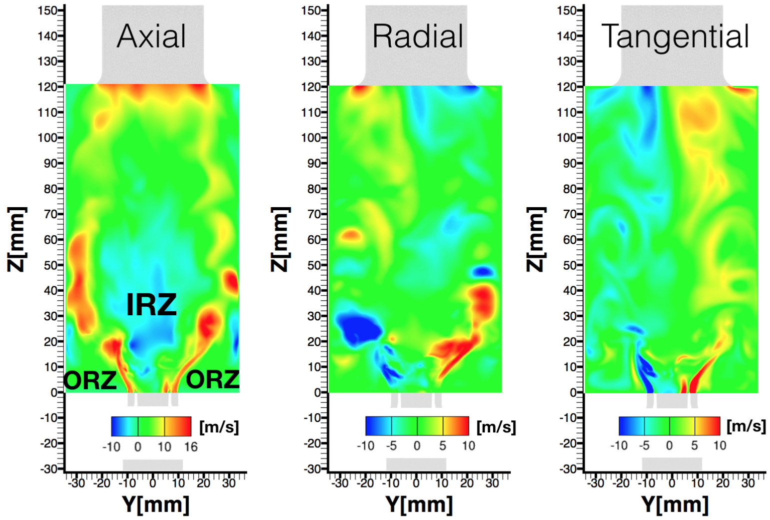

Figure 3.2: Instantaneous velocity contours for 3 bar case without sidejet. Locations of inner recirculation zone (IRZ) and outer recirculation zone (ORZ) are specified.

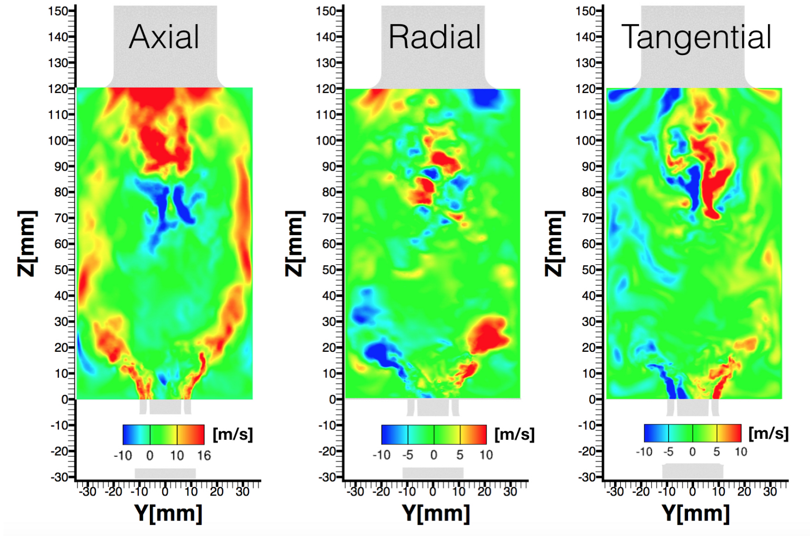

Figure 3.3: Instantaneous velocity contours for 3 bar case with sidejet.

fuel pockets for prolonged times inside the IRZ, where slow recirculating zone with relatively high temperatures and long residence time can promote soot formation.

In the presence of sidejets, the mixture fraction and temperature contours (Fig. 3.4) are more complex. A low temperature zone forms near the sidejet interaction region in the center of the combustor. Moreover, there are pronounced gradients in temperature between the shear layers that isolate the inner and outer recirculation zones and the core of the IRZ. This flow structure illustrates that the secondary oxidation air is not simply transported downstream but is predominantly entrained into the IRZ. In this case, strong temperature gradients persist towards the exit of the combustor. As a result, there exists a relatively low temperature (< 1000 K) region along the axial length of the combustor, while higher temperatures are found near the walls and the shear layers. This suggests a more diffusion-flame like structure as compared to a homogeneous premixed-flame type behavior for the case without sidejets.

Figures 3.6 and 3.7 show time-averaged velocity fields for all the cases considered. The prominent features in the axial profile include the negative velocity recirculation zones and the arms of the shear layer extending the entire axial distance of the combustor. Since the combustor is not cylindrical, there is variation in these profiles for different azimuthal angles, but the general trends hold. Of particular significance is the comparison between the 3 and 5 bar cases. As noted above, the two cases have identical inflow velocity conditions but differ in the fluid density and the Reynolds number of the flow. At 66% higher Reynolds number, the 5 bar case is more turbulent, which leads to a slightly modified IRZ with two symmetric lobes. With sidejets, the IRZ is more compact and centered near the sidejet interaction region at the center of the combustor for the higher pressure case. Tangential velocity profiles show the formation of an enclosure for the IRZ at 3 bar case with sidejet, while the enclosure does not exist at 5 bar.

Figure 3.8 shows time-averaged temperature profiles for all cases. Similar to the

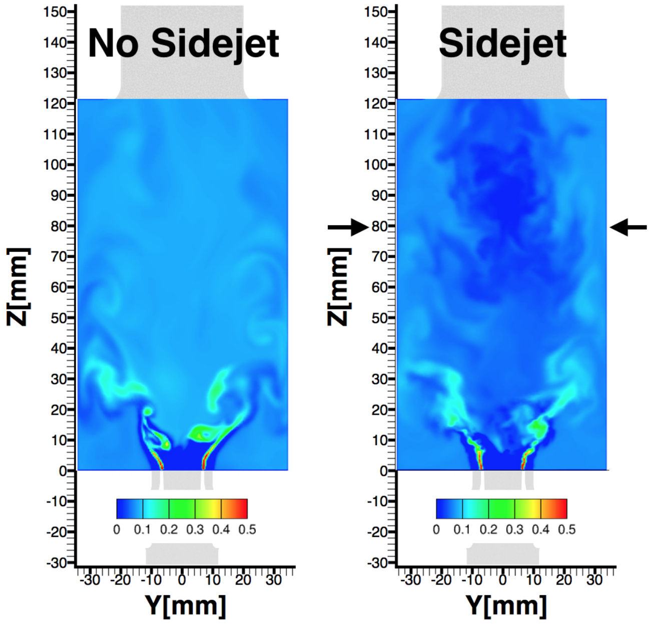

(a) Mixture Fraction

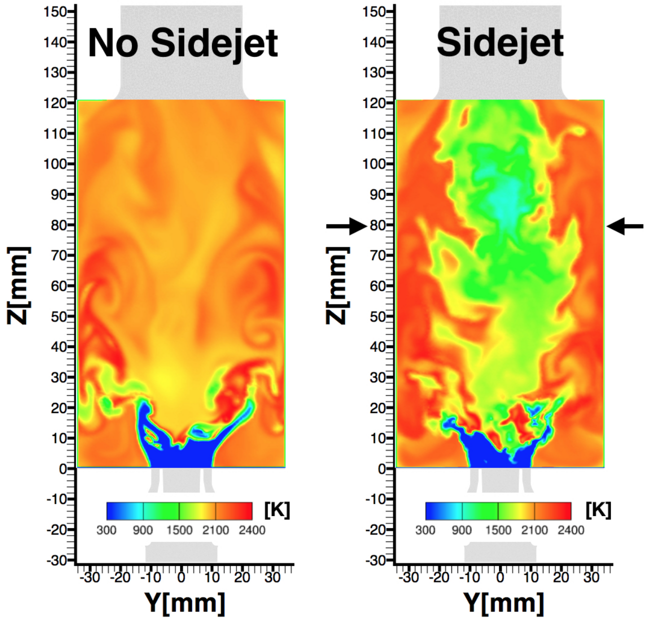

(b) Temperature

Figure 3.4: Instantaneous mixture fraction and temperature contour comparisons for 3 bar case. Arrows indicate location where dilution jet is injected.

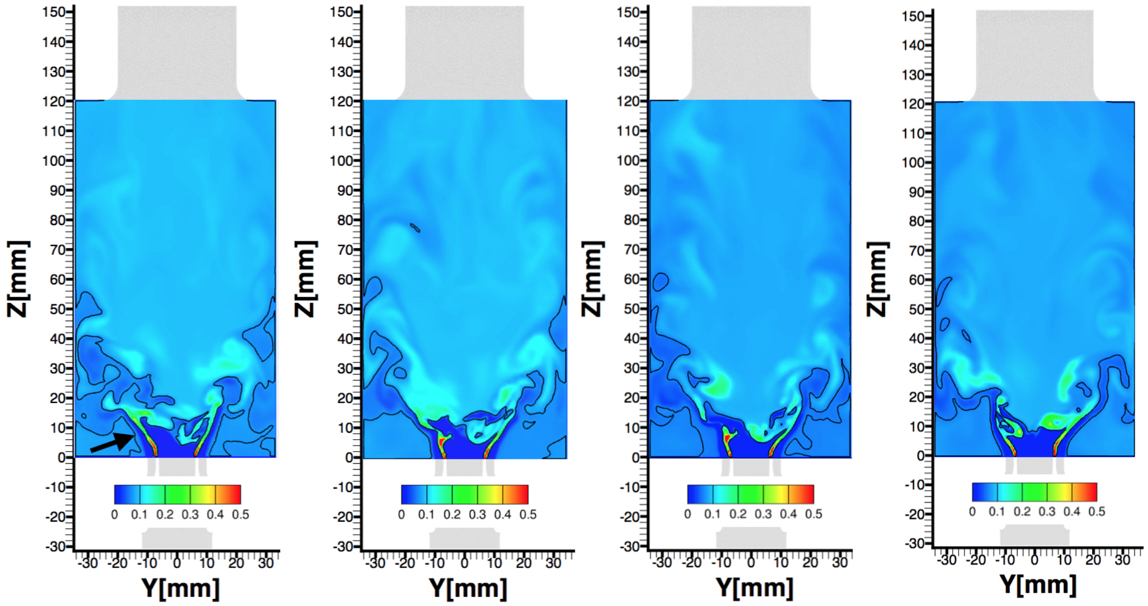

Figure 3.5: Snapshots of mixture fraction for 3 bar case (no sidejet), proceeding from left to right in 5 ms increments. Solid lines show stoichiometric mixture fraction (0.064). Arrow indicates the flapping jet arm.

instantaneous images, the temperature field is nearly uniform downstream of the near-nozzle region, with symmetric mixing shown in the form of a V-shape near the nozzle. In the case with sidejets, this near-nozzle region is preserved, but temperature is reduced in the sidejet interaction region in the center of the combustor. Further, there are clear regions of temperature gradient along the axial distance of the combustor. This is reflected in the instantaneous images of temperature and mixture fraction shown above. Since the time-averaged and instantaneous profiles look similar, it can be concluded that the temperature gradients persist during the entire simulation, and are part of the flow features when sidejets are present.

The differences in the temperature distribution are created by changes in the mixture fraction field (Figure 3.9). The comparisons between four cases show that there are clear differences between cases with and without sidejets, while the change in pressure only affects the distribution of mixture fraction in a more subtle manner.

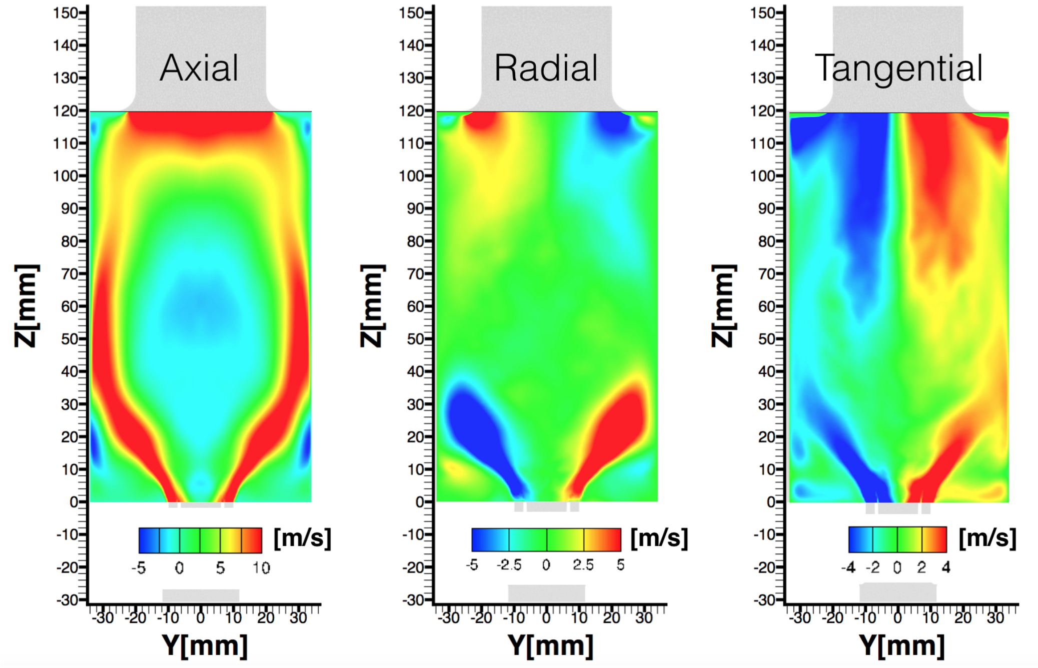

(a) 3 bar

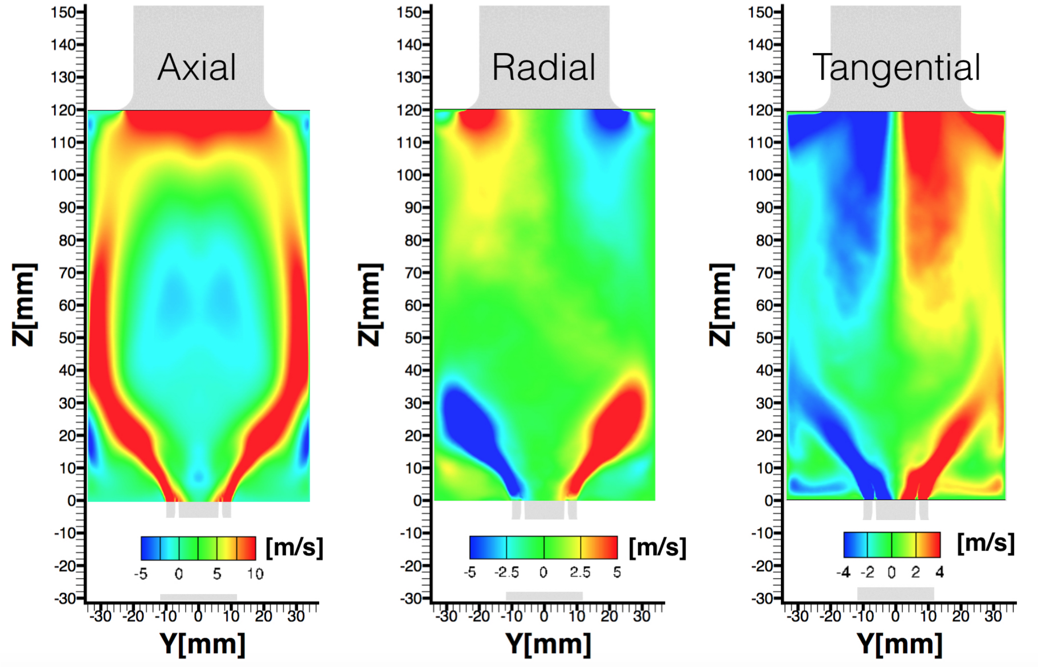

(b) 5 bar

Figure 3.6: Time-averaged velocity contour for 3 and 5 bar cases without sidejet.

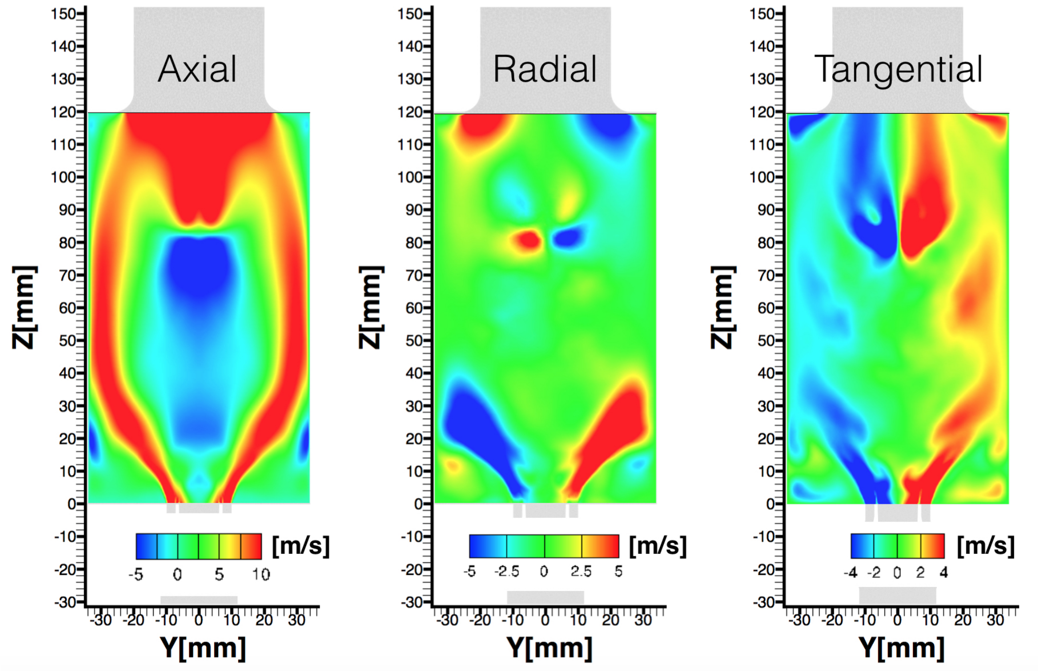

(a) 3 bar

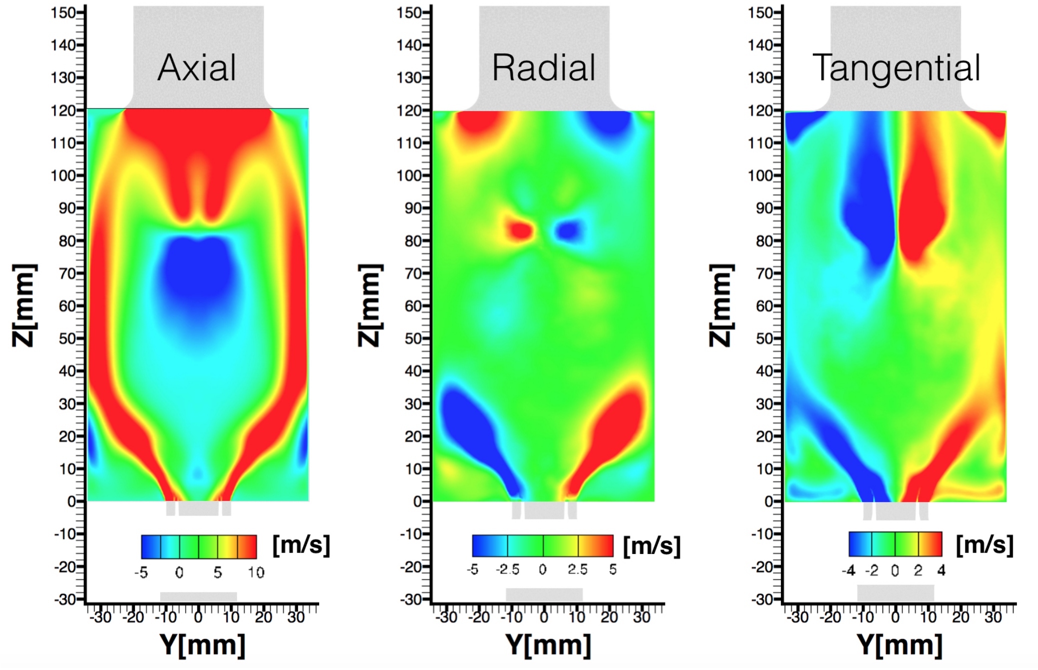

(b) 5 bar

Figure 3.7: Time-averaged velocity contour for 3 and 5 bar cases with sidejet.

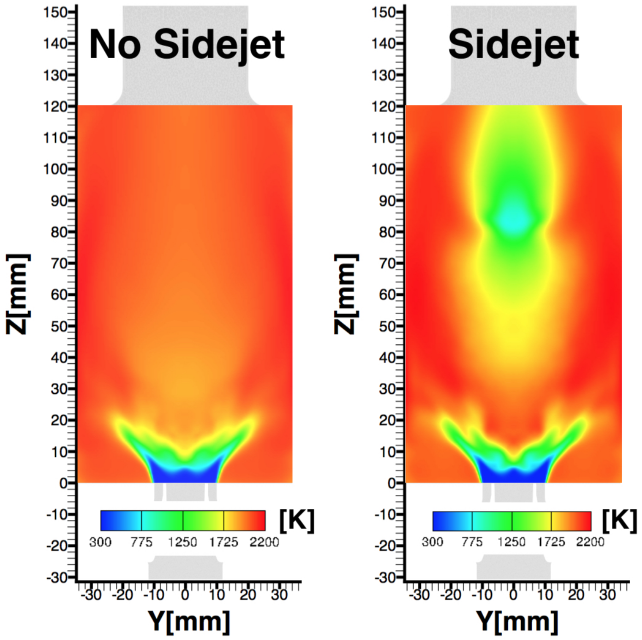

(a) 3 bar

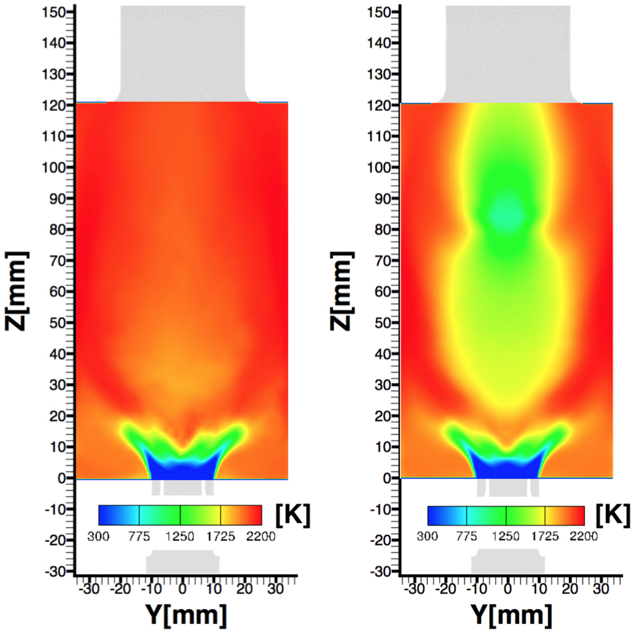

(b) 5 bar

Figure 3.8: Time-averaged temperature contour for 3 and 5 bar cases.

The 3 bar case shows a slightly richer field in the IRZ, in spite of having identical global equivalence ratios. This is due to large scale flow structure differences between the cases at different Reynolds numbers, deflecting more fuel rich pockets into the IRZ at 3 bar. It is seen that the case with sidejet leads to much lower mixture fraction values in the domain, specifically in the IRZ, due to higher oxidizer concentration. Further, the fuel jet is deflected more towards the wall in the sidejet case, leading to higher temperature in the shear layers.

3.4.2 Evolution of soot particles

Soot generation is inherently intermittent, leading to large variations in volume fraction with time (see discussion in *Raman and Fox* (2016); *Qamar et al.* (2009), and references within). As a result, instantaneous snapshots cannot reveal the full picture about the location of peak soot production. Figure 3.10 shows soot volume fraction contour with OH mass fraction and stoichiometric mixture fraction line. For this configuration that is far from extinction limits, the peak reaction rates for gas phase fuel oxidation occur near the stoichiometric line. As expected, soot is generated on the rich side, while OH concentration peaks on the lean side of this stoichiometric contour. It is important to recognize that even though the OH structure is linked to the stoichiometric contour directly through the flamelet table, soot generation is only indirectly affected through the source terms in the population balance (moment) equations. Further, there is almost no soot leakage to the lean side in the sidejet case, indicating complete oxidation of the particulate phase.

In comparing with instantaneous velocity and mixture fraction profiles (Figures 3.2, 3.3 and 3.4), it is seen that soot generation occurs in small fuel-rich pockets located near the shear layers generated by the fuel and oxidizer jets entering the domain. Due to the slow kinetics associated with soot, significant volume fraction is only observed several jet diameters downstream of the fuel nozzle. In particular, much of soot for-

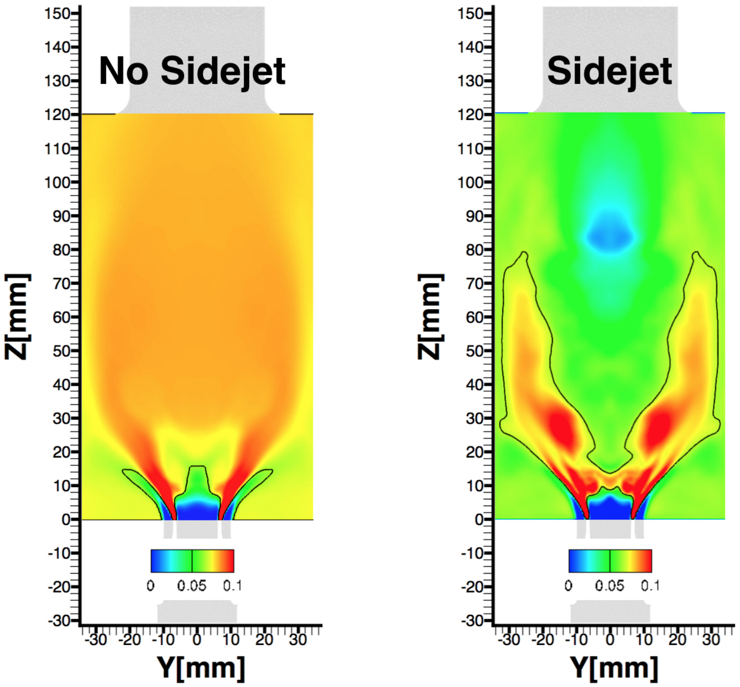

(a) 3 bar

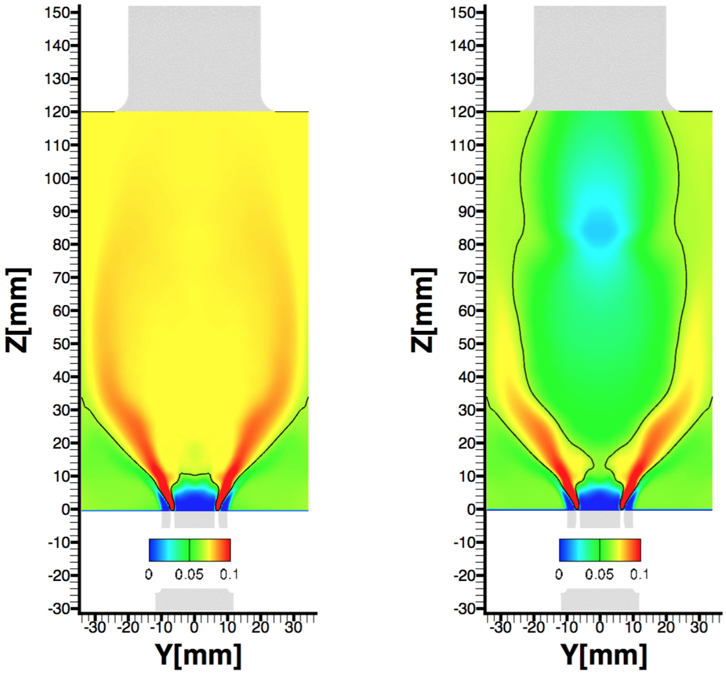

(b) 5 bar

Figure 3.9: Time-averaged mixture fraction contour for 3 and 5 bar cases. Solid lines show the stoichiometric mixture fraction (0.064).

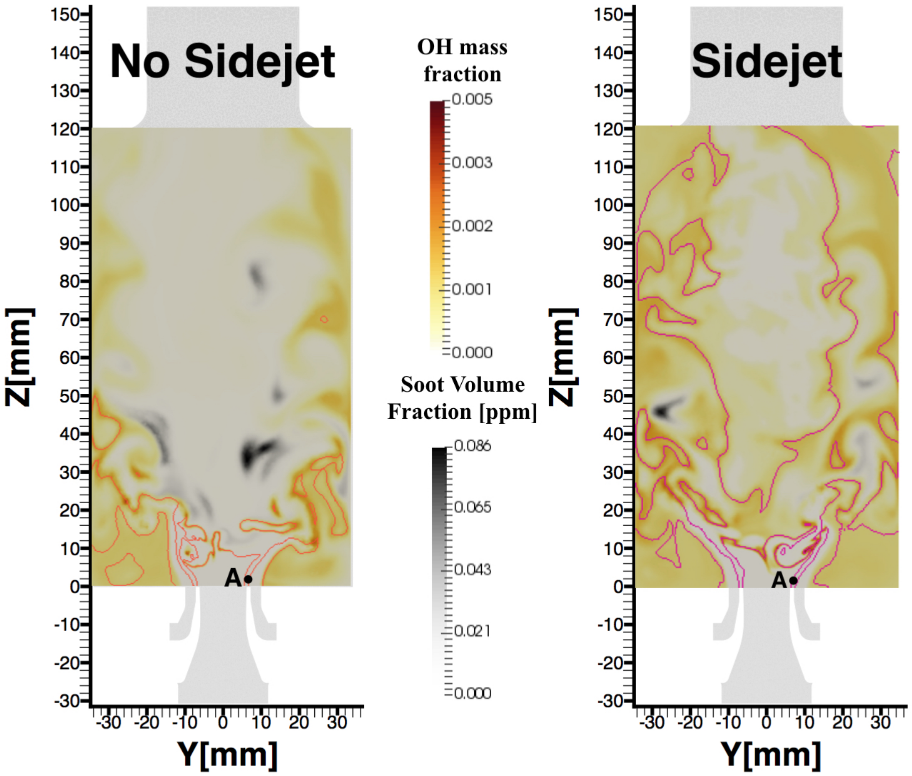

Figure 3.10: Instantaneous soot volume fraction overlaid with isocontour of OH mass fraction for 3 bar cases. Solid lines show the stoichiometric mixture fraction (0.064). Point A is the initial location from which particles are released for Lagrangian analysis.

mation is confined to the arms of the jet. Time sequences (not shown here) confirm that soot production is dominated by this shear region and the soot number density, which is a marker for nucleation, shows peak values also along this shear layer, with significant drop further downstream due to combined effects of agglomeration and oxidation. Comparing the cases with and without sidejets in Figure 3.10, the simulations show that the presence of the sidejet reduces soot formation in the near-nozzle region, especially in the shear layer formed between the IRZ and the fuel/oxidizer jets. Further, sidejets also increase oxidation of soot with increased OH mass fraction downstream.

The intermittency of soot formation can be viewed through snapshots rather than individual images. Figure 3.11 shows soot volume fraction images separated by 2 ms in time. It is seen that soot is distributed sparsely in the domain, with small patches of high soot concentration. Experiments show similar sparse soot presence, albeit with higher soot concentrations in some cases (*Geigle et al.* (2014)). The instantaneous soot volume fraction contours further verify that soot near the bottom of the IRZ occurs through intermittent patches. As a result, even though the fluid from the inlet reaches combustor exit in roughly 12.5 ms, the soot motion within the IRZ is comparatively slower, and will require much longer simulation and averaging time in order to obtain converged statistics (See Appendix 3.4.5 for more details).

This intermittency is driven by the turbulent fluctuations of the gas-phase composition, and the slower response of the soot formation processes. In particular, it is seen that the flapping motion from the fuel jet in Figure 3.5 shows mixture fraction contours near the fuel jet inlet with the jet arm at extreme locations in the radial direction. At certain times, the jet breaks down immediately after entering the combustor, leading to fuel-rich pockets that are entrained by the recirculation zone. This shearing motion is amplified by the highly unsteady transverse motions of the recirculation zone. The jet-flapping is the main source of intermittency in this combustor. Unlike intermittency due to small scales (*Attili et al.* (2014)), soot intermittency in such gas turbines is driven by these large scale hydrodynamic motions. The sporadic soot generation is the result of such large scale motions introducing fluid trajectories that pass through soot-favored regions in composition space. Therefore, capturing unsteadiness especially in the inlet condition is important in soot prediction of this configuration.

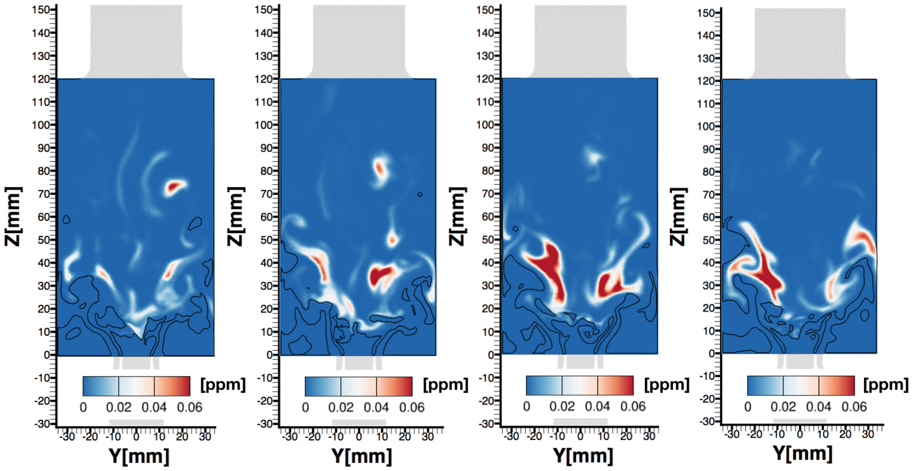

Figure 3.11: Instantaneous soot volume fraction snapshots of 3 bar case without side-jets, separated by 2.0 ms, and overlaid with stoichiometric mixture fraction (0.064) line.

3.4.3 Validation against experimental results

3.4.3.1 Gas phase statistics

Since the soot phase exhibits slow temporal dynamics, statistics of the flow have to be obtained over long averaging times. A discussion of the convergence of these statistical features is provided in Appendix 3.4.5. Further, due to the highly chaotic and unsteady nature of the flow, grid convergence also needs to be established. In theory, grid-filtered LES cannot be grid converged, since any mesh refinement automatically implies a change in filter width (*Pope* (2004)). However, statistics of large scale properties generally converge with resolution as high-gradient regions such as shear layers are better captured. Hence, grid convergence should be used more as a qualitative metric of the reliability of the results, rather than a strict reduction of numerical truncation errors (*Kaul et al.* (2009); *Kaul and Raman* (2011); *Heye et al.* (2011)). Such a grid convergence study is presented in Appendix 3.4.4.

Figures 3.12 to 3.14 show comparisons of gas-phase velocity statistics with experimental data. Note that PIV-based velocity information is available only for the

3 bar case and not all positions are shown for conciseness. Comparisons are only shown for selected locations most pertinent to capturing the mixing region, high velocity shear layer, and recirculation zone. These results show that the simulations are extremely adept at capturing the flow structure, including the details of the recirculation zone and the tangential velocity components. Moreover, Figure 3.14 shows that Root-Mean-Square (RMS) velocity is captured accurately as well. There are no experimental data for comparison of RMS velocity for 3 bar case without sidejet but flow fluctuations are captured well in the more turbulent case with sidejet injection, especially at the sidejet interaction region (80 mm). It is important to recognize that, given the complexity of the flow field and the highly unsteady nature of the turbulent system, such good comparisons throughout the flow path are encouraging. The good prediction of RMS velocity components further shows that the use of the refined grid and the reduced-dissipation numerical approach is well-suited for such complex geometries.

Figure 3.15 shows the mean centerline temperature profiles from experiments and simulations, while Figure 3.16 shows comparisons for mean radial temperature profiles at selected axial locations (and only at 3 bar condition). In general, the simulation profiles are consistent with the experimental results. For the cases with sidejet for both pressures, the model captures the trend but underpredicts the temperature at the centerline. More specifically, the dip in temperature near the sidejet interaction region is captured well in the axial and radial profiles, respectively. The temperature profile peaks in the near-nozzle region, at the base of the recirculation zone where stoichiometric conditions are reached, and decreases (for sidejets) or stays nearly uniform (without sidejets) downstream. Agreement for the radial profiles is satisfying, with reduction in temperature at downstream locations captured well. The experimental data does have some limitations, including the inability to get near-wall readings at the time of this simulation study. Further, it is important to note that the width

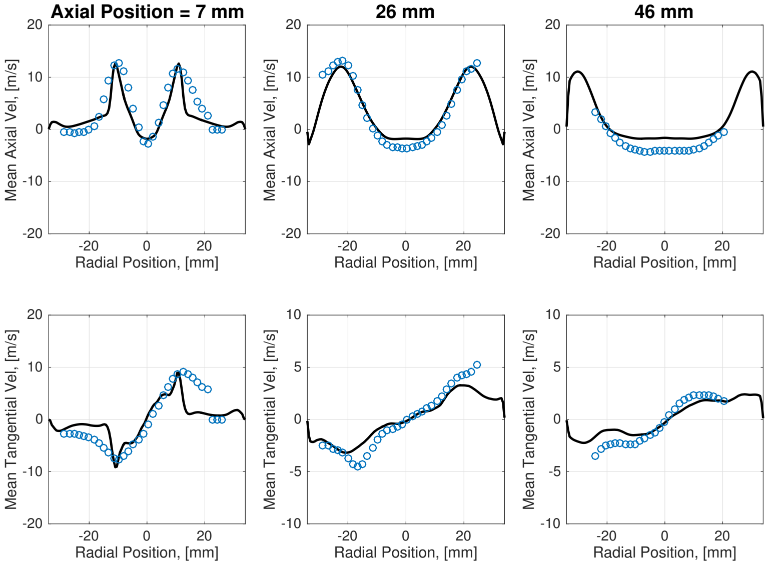
Axial Position = 7 mm
26 mm
46 mm

Figure 3.12: Time-averaged velocity comparison with experimental data for 3 bar case without sidejet.

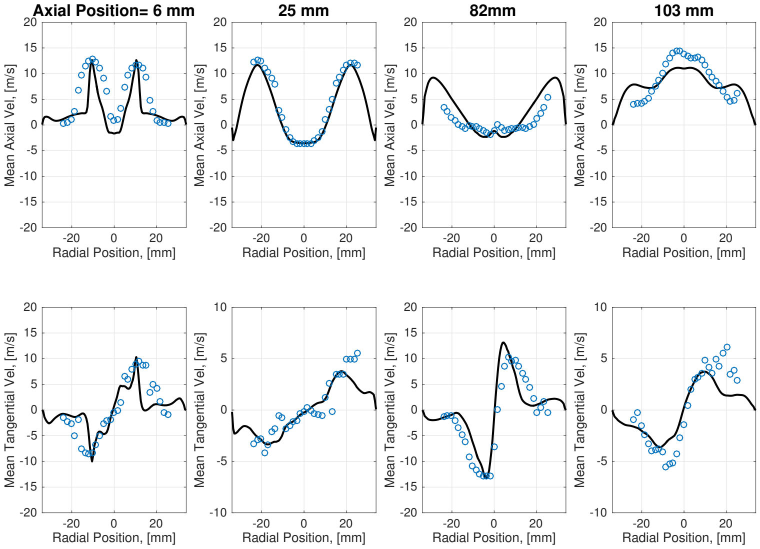
Axial Position= 6 mm
25 mm
82mm
103 mm

Figure 3.13: Time-averaged velocity comparison with experimental data for 3 bar case with sidejet.

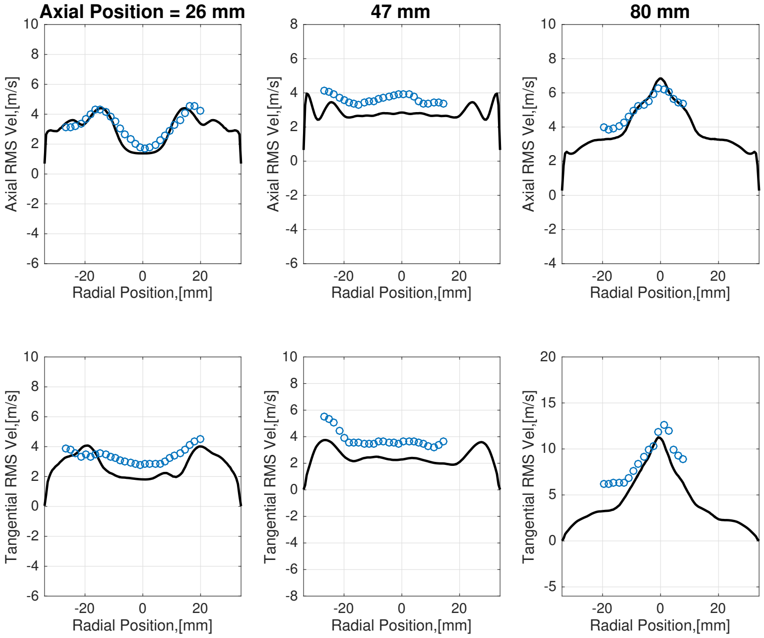

Figure 3.14: RMS velocity comparison with experimental data for 3 bar case with sidejet.

of measured experimental statistics are relatively large, which makes a more refined comparison with simulations not very meaningful. In complex geometries, the lack of fidelity of experiments is well-appreciated, and these results are a demonstration of such challenges.

3.4.3.2 Soot statistics

Figures 3.17 and 3.18 show comparisons of time-averaged LES with experimental soot volume fraction fields for 3 and 5 bar cases respectively. As expected, the higher pressure case contains higher soot volume fractions, especially in the shear layers close to the side walls. The LES computation captures this trend, providing basic verification of the pressure dependence of the chemical source terms. However, the soot volume fraction for 5 bar case is underpredicted by about a factor of 4. Without the sidejets in the 3 bar case, experiments show peak soot concentrations in the

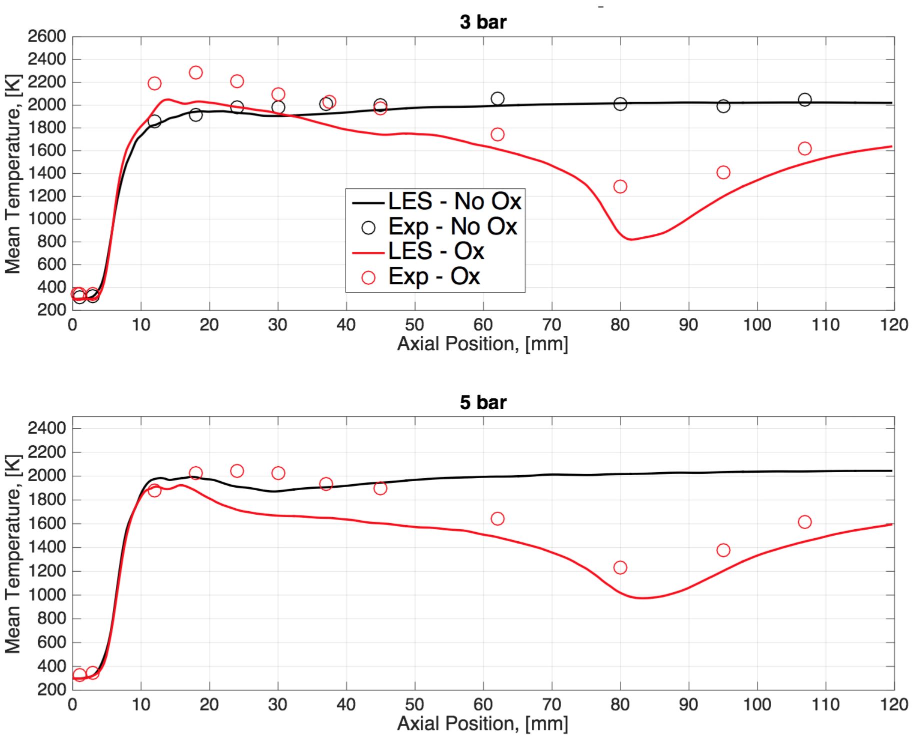

Figure 3.15: Mean centerline temperature comparisons of simulation with available experimental data for all cases. Note that no experimental data is available for the 5 bar case without sidejet.

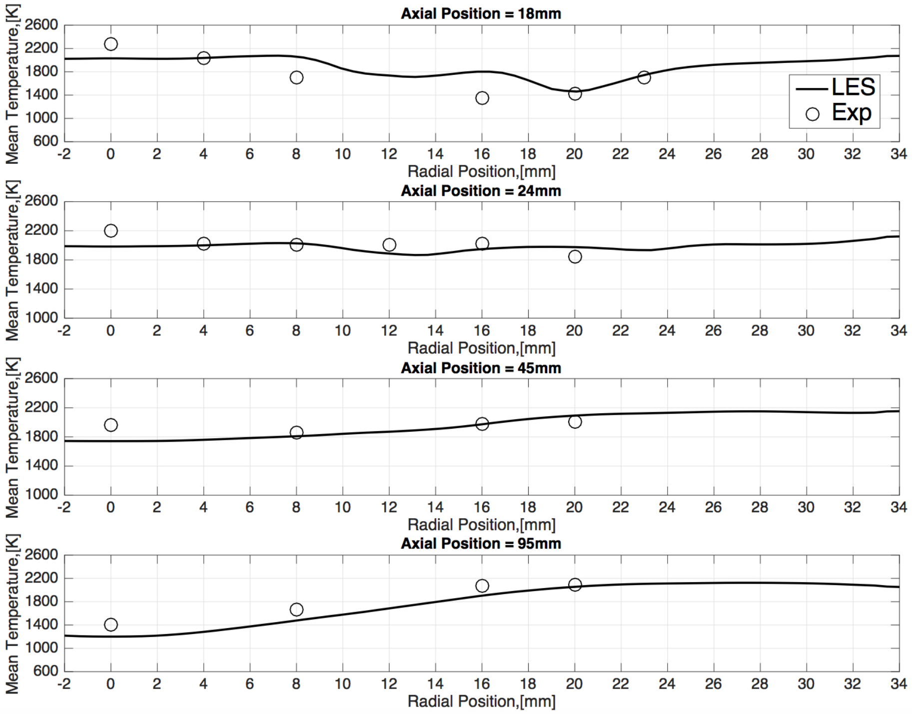

Figure 3.16: Mean radial temperature comparisons of simulation results with experimental data for 3 bar case with sidejet.

IRZ. The simulations show soot locations predominantly in the shear layers, which is consistent with the instantaneous snapshots in Sec. 3.4.2. The presence of the sidejets leads to soot being confined to the shear layers in the experiments, which is consistent with the LES results.

Figures 3.19 and 3.20 show radial plots of experimental and LES results, which provide a more quantitative comparison. As seen, the simulations underpredict experimental data by an order of magnitude, depending on the location and pressure condition. At 5 bar pressure, the model predicts accurately the soot locations but consistently underpredicts soot volume by about a factor of 5. Another prominent deviation is the consistent underprediction of soot volume fraction downstream of the combustor. Soot oxidation rate or OH mass fraction could have been overpredicted to cause such a deviation. As seen in the contour plots (Figures 3.17 and 3.18), soot formation in the recirculation zone is underpredicted in the models, which leads to the

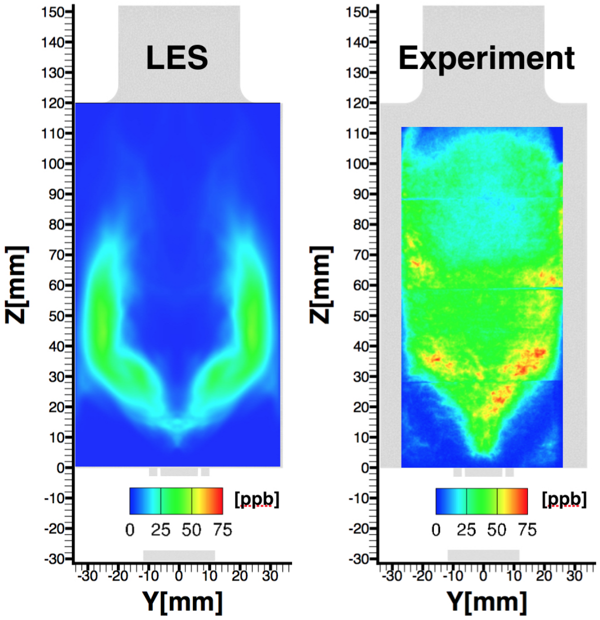

(a) No sidejet

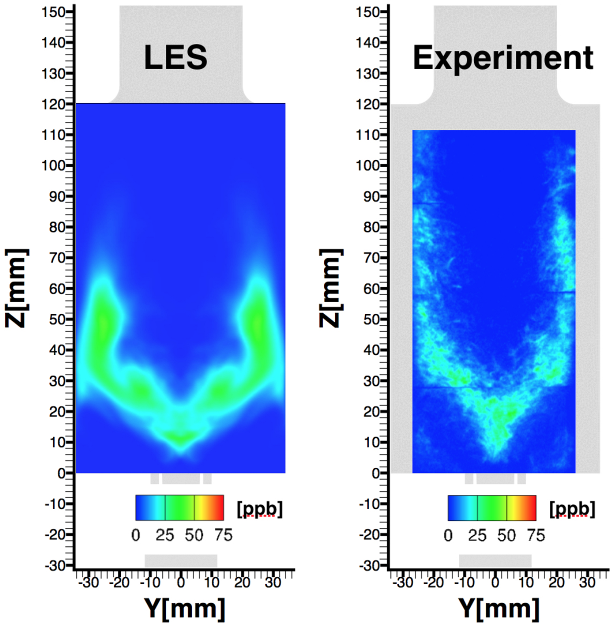

(b) Sidejet

Figure 3.17: Soot volume fraction comparison with experimental data for 3 bar case.

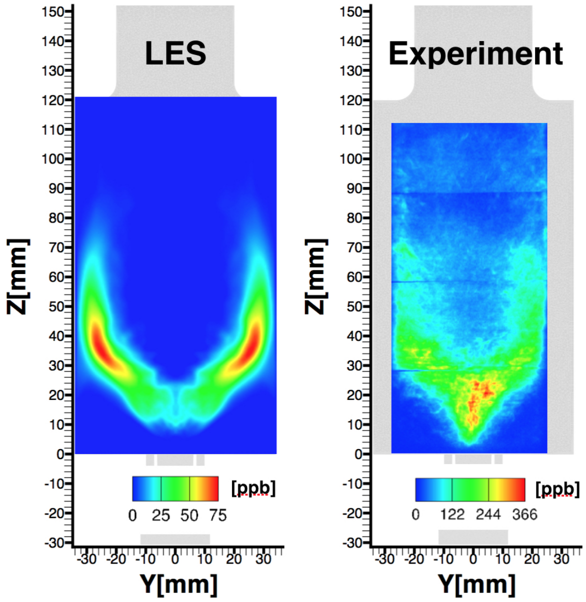

(a) No sidejet

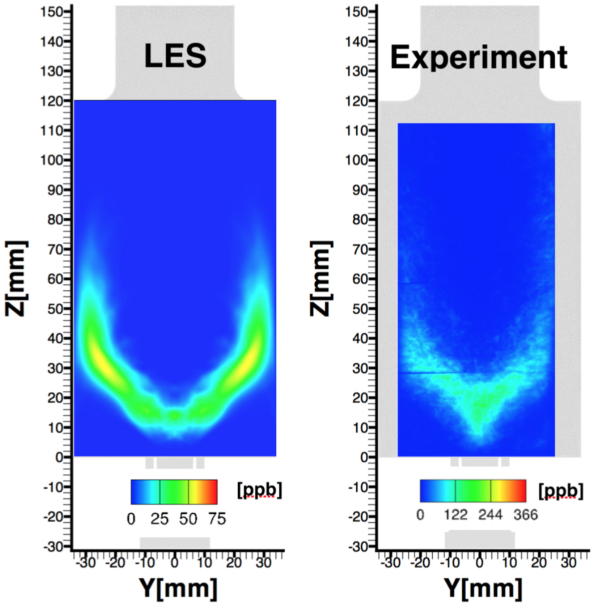

(b) Sidejet

Figure 3.18: Soot volume fraction comparison with experimental data for 5 bar case. Note the difference in contour color limits of approximately a factor of 5.0 between LES and experiment.

lack of a pronounced peak as in the experimental profile at 20 mm axial position. The trajectories of the soot pockets in the simulations do not promote soot mass addition in the IRZ. The presence of the sidejet diminishes this peak in the 3 bar case in the experiment, essentially due to increased oxidation of the entrained fluid, although the reason as to why the soot arm was not shortened by the sidejet at 3 bar when the 5 bar case shows such behavior is still unknown. Compared to other simulation works on the 3 bar case with sidejet (*Eberle et al.* (2015); *Wick et al.* (2017b)), the current model predicts the spatial and magnitude of soot volume fraction more accurately. Using a semi-empirical, PAH-based soot model, *Eberle et al.* (2015) overpredicted the soot volume fraction in the shear layer and underpredicted the soot volume fraction at the central region above the inlet. Simulations with moment based models (current study and *Wick et al.* (2017b)) predict soot at the same location above the inlet. The one similarity across different models is the high oxidation rate above 70 mm in the combustor, leading to underprediction of soot in the downstream region. In the 5 bar case, the model predicts essentially an order of magnitude lower soot volume fraction at the zone right above the nozzle compared to the experiment. This could be caused by a lack of information on the velocity boundary conditions for the 5 bar cases that could help elucidate the overall flow structure of the case.

While these results show qualitative agreement, there are still considerable differences. In particular, the switch from IRZ-based soot formation to shear-layer formation that is observed in experiments without and with sidejets is not fully captured by the simulations. In order to determine the possible reasons for these deviations, it is important to discuss these results in the context of prior studies. As briefly mentioned in Section 3.1, prior results using the models described here have provided disparate conclusions. Simulations of jet flames have generally underpredicted soot volume fractions (*Donde et al.* (2013); *Xuan and Blanquart* (2015); isf (2016)), while bluff-body type recirculation flows have yielded better agreement with simulations

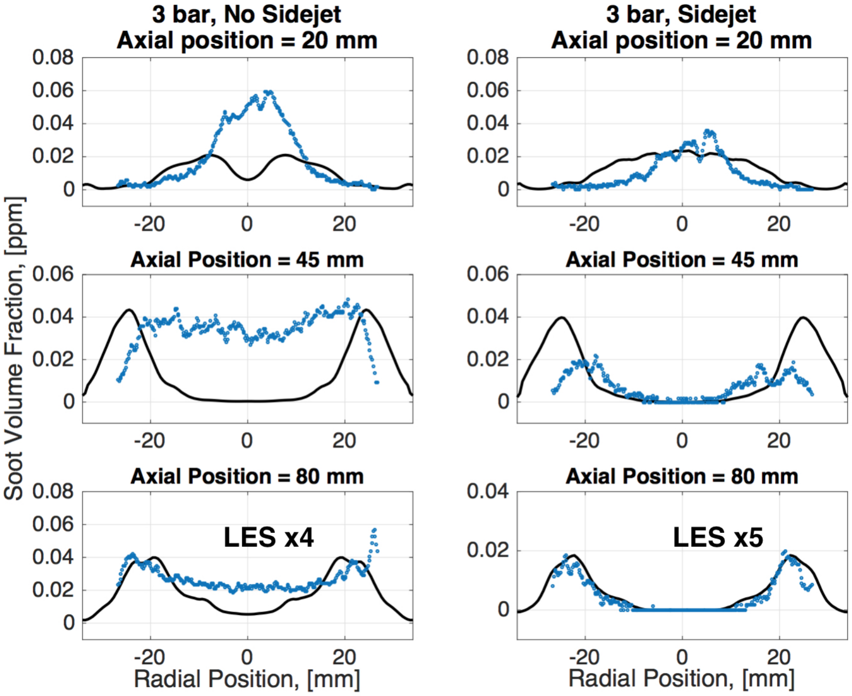

Figure 3.19: Soot volume fraction comparison of LES (line) with experimental data (scatter) for 3 bar case. LES results are multiplied by the corresponding factors as indicated in the figures only for the 80 mm axial position.

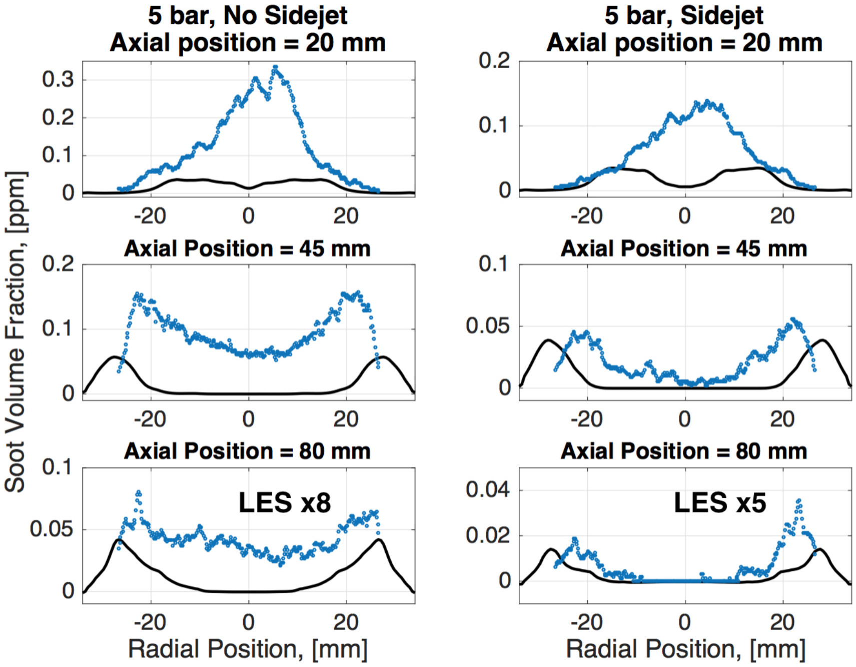

Figure 3.20: Soot volume fraction comparison of LES (line) with experimental data (scatter) for 5 bar case. LES results are multiplied by the corresponding factors as indicated in the figures only for the 80 mm axial position.

(*Mueller et al.* (2013)). Partly, this is due to the nature of the models that are active. In jet flames, PAH-based condensation was found to be responsible for much of the soot growth, while in recirculation-dominated flows, growth through acetylene addition is of more importance (*Mueller et al.* (2013)).

To understand the relative contributions of different physical processes, the source term contributions for the volume moment is plotted in Figure 3.21 for the 5 bar case with and without sidejets. The dominant soot mass generation term is due to acetylene-based surface growth, which is spatially located adjacent to the peak oxidation zone, and separated by the stoichiometric contour line. Unlike bluff-body stabilized flames, there is no clear regions where PAH condensation based growth or nucleation is dominant. In the presence of sidejets, all generation terms are significantly suppressed, mainly due to the entrainment of oxidation air into the IRZ. Regardless, acetylene-based growth is still the dominant contributor to soot volume fraction.

Given this surface-growth based soot formation, a better prediction of soot is to be expected given results from prior studies. We attribute the deviation from experiments to small errors in velocity and mixture fraction fields. It is known that acetylene concentrations are not sensitive to small-scale dissipation rate fluctuations (*Attili et al.* (2014)). Hence, these discrepancies can arise from deficiencies in the soot models themselves and the inability to predict flow fields with high precision. For instance, in regions where the RMS velocity comparisons are good, soot predictions are also equally better. Other studies have also shown similar sensitivity to the flow field (*Wick et al.* (2017b)). In other words, the level of accuracy with which the flow field needs to be captured is significantly higher for predicting soot as compared to gas-phase species.

While the average source terms shown above provide the dominant mechanisms, their relative importance also depend on the particular trajectories that soot particle

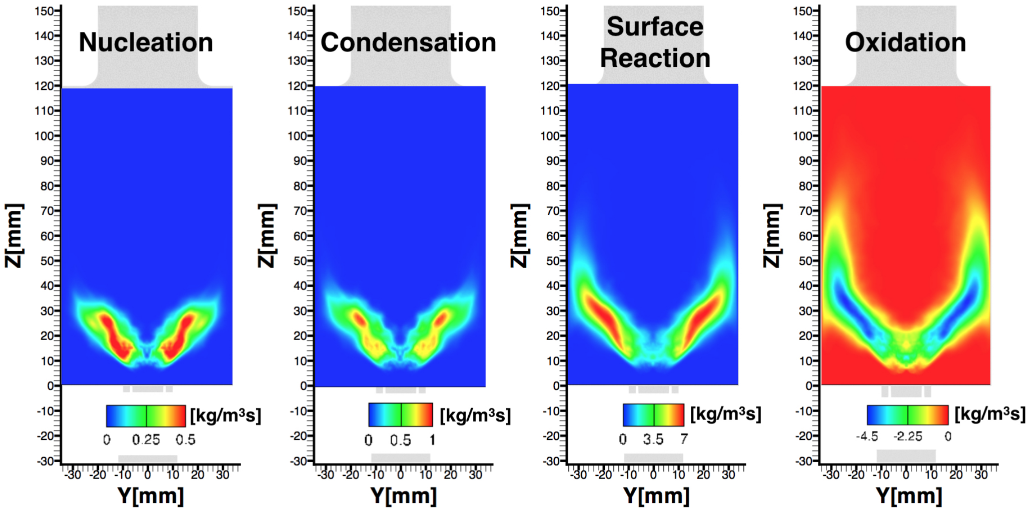

(a) No Sidejet

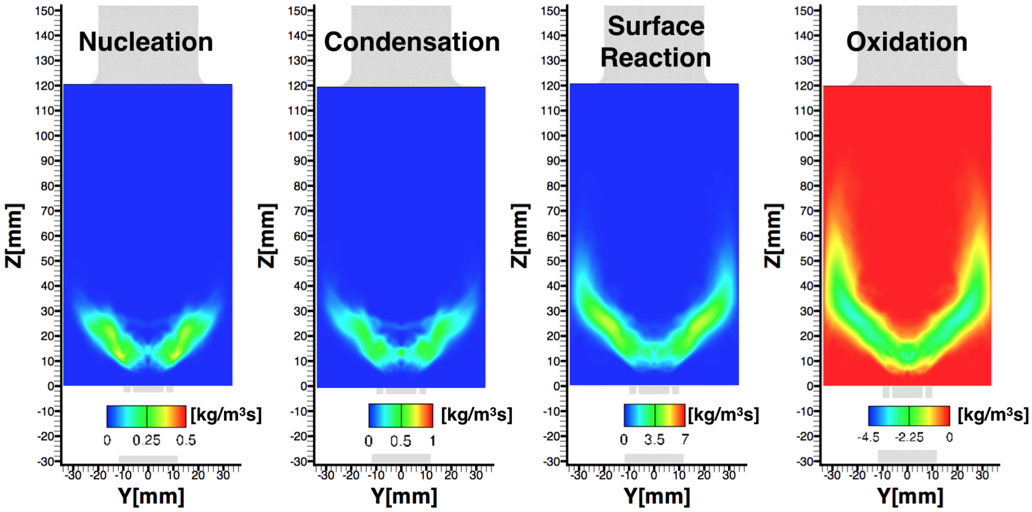

(b) Sidejet

Figure 3.21: Time-averaged soot volume fraction source terms comparison for 5 bar case.

take inside the combustor. To obtain this information, a Lagrangian approach is used to follow particle-like trajectories during the LES calculation. An ensemble of notional particles is released into the domain through the fuel injection ports. In this case, roughly 1000 particles are followed. The injection point is consistent across all four cases and is located directly above the fuel port as shown in Fig. 3.10. The source of the injection point is a sphere of diameter 0.5 mm with the particle positioned at the surface of the sphere. Particles are tracked for a total of 75 ms, sufficiently long to determine soot mass addition behavior. The notional particles are advanced in space using the local fluid velocity. At each time-step, the gas-phase properties and soot source terms associated with the local Eulerian soot field are stored. Time along the particle trajectory is regarded as residence time in the chamber and only the axial position of the particle is of interest whereby any particle having axial position $Z <$ 40 mm after a residence time of 0.01 s is regarded as being in the recirculation zone.

These trajectories can be classified into three dominant classes:: (i) Particle Type 1, where particles are convected downstream following the flow field close to the wall and subsequently exit rapidly through the outlet, (ii) Particle Type 2, particles that remain in the recirculation zone upstream, and (iii) Particle Type 3, particles that are entrained into the IRZ at a downstream location and convected back upstream.

Figure 3.22 shows mass source terms for each kind of particle in the combustor. The intermittency of soot generation can be readily seen from the fluctuating soot source terms encountered along the particle trajectory. Type 1 particles experience high soot production and oxidation fields, but remain inside the combustor only for a short time. Such particles are expected to travel along the arms of the shear layer, and are subject to soot evolution processes akin to a non-premixed jet. Type 2 and 3 particles undergo weaker but multiple soot mass addition events, indicating that they pass through relatively fuel-rich regions of the flow multiple times. Even if the source terms are not very high, the long residence times provide the means for sufficient soot mass addition.

In order to further understand the characteristics of different soot paths, the conditional mean trajectories (based on particle type) of the notional particles in mixture fraction and progress variable space are plotted in Fig. 3.23. It is seen that the Type 1 particles start from the rich side of the jet, and traverse through the high temperature region towards the lean side. On the other hand, Type 3 particles start from the rich side and move to richer parts of the jet, and pass through similar gas-phase compositions multiple times, mostly at the downstream region of the IRZ. Type 2 particles provide the transition from 1 to 3, with slight motion towards the rich side before moving back towards the lean region of the combustor. The percentage of each of these types of particles are highlighted in Table 3.2. It can be seen that Type 1 particles dominate in this combustor, regardless of the operating condition considered. Further, the percentage of Type 1 particles increase as pressure increases. A similar trend is noticed when sidejets are introduced at any given pressure. Hence, air injection not only reduces the global equivalence ratio, but also changes the hydrodynamic structure of soot generation.

Case	Particle Type 1 (%)	Particle Type 2 (%)	Particle Type 3 (%)
3 bar, No sidejet	76.3	21.3	2.4
3 bar, Sidejet	78.6	21.1	0.3
5 bar, No sidejet	83.1	16.5	0.4
5 bar, Sidejet	84.8	14.9	0.3

Table 3.2: Percentage of particle types by trajectory illustrated in Fig 3.22.

It is apparent that the higher pressure case contains higher soot concentrations than the lower pressure case, although the regions of soot formation are similar. Further, the peak soot levels are higher in the 5 bar case compared to the 3 bar case.

The differences in the soot formation process for the 3 and 5 bar cases can be diagnosed using the Lagrangian trajectories as well. Figure 3.24 shows the scatter

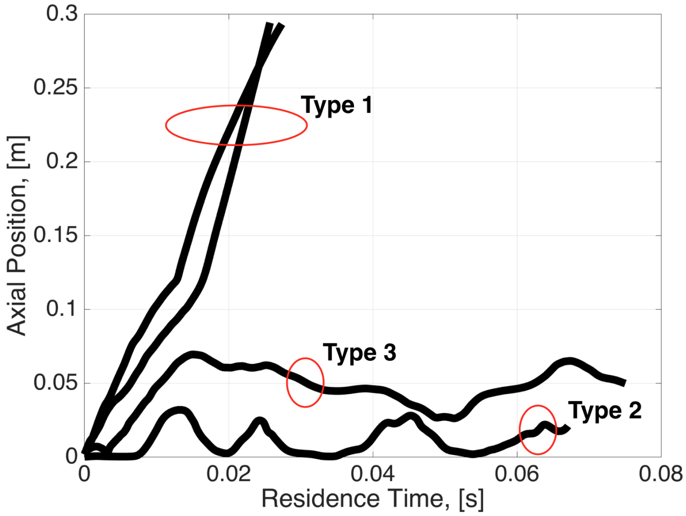

(a) Particle trajectory

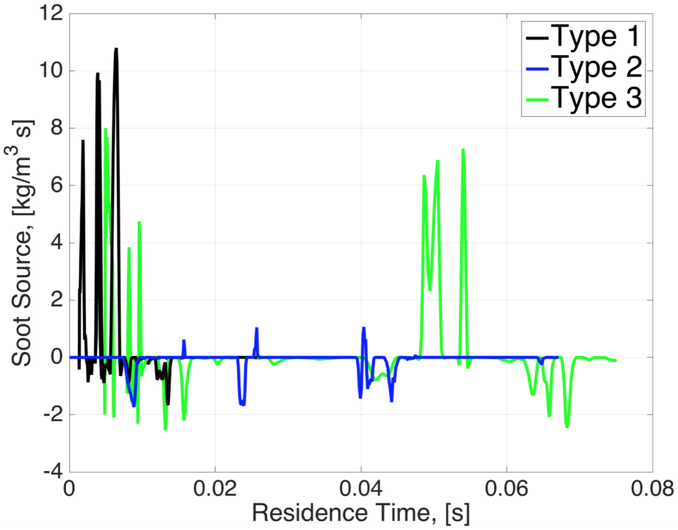

(b) Soot source

Figure 3.22: Lagrangian particle tracking of 4 example particles showing (a) particle trajectory by type, and (b) intermittent soot source, for 3 bar case without sidejet. Soot source includes nucleation, condensation, surface growth, and oxidation reactions.

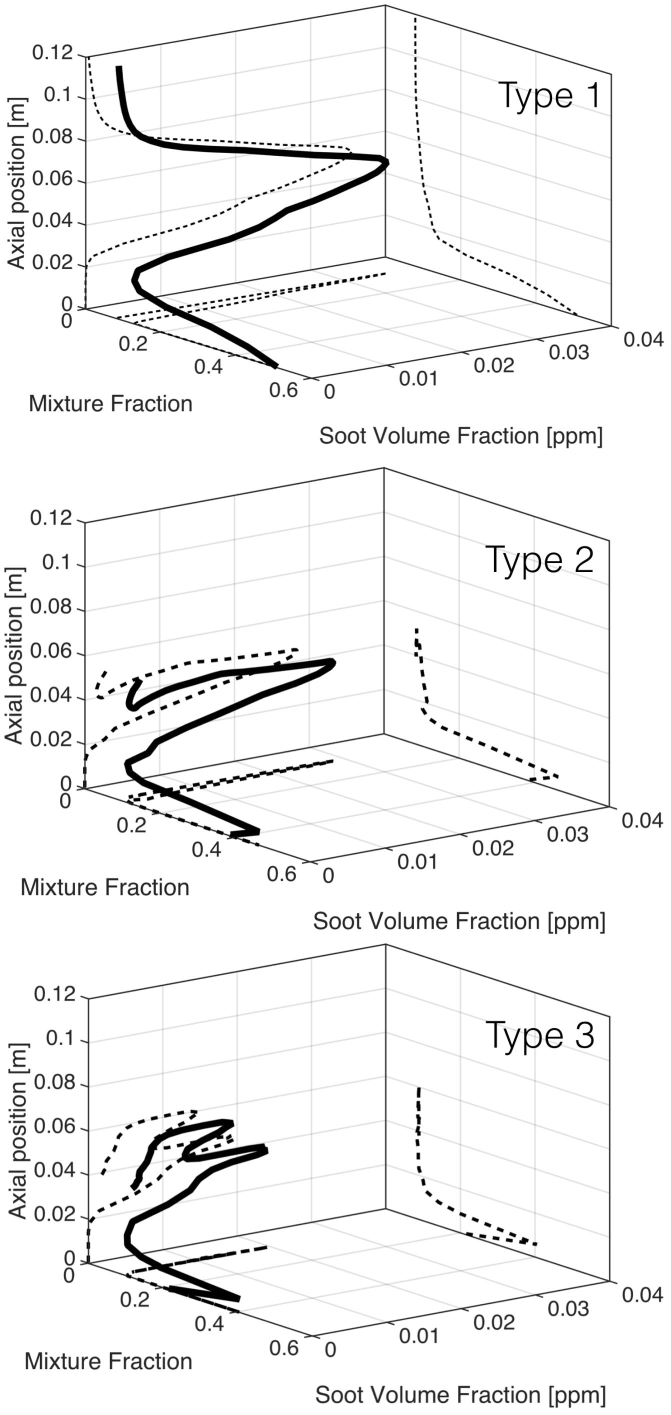

Figure 3.23: Ensemble averaged axial position, mixture fraction and soot volume fraction of lagrangian particles, by particle type, for 3 bar case without sidejet. Particle data was taken over the first 20 ms residence time for clearer visualization of the trajectory of the particle. Dashed line are projected trajectory onto the corresponding plane.

plot of Lagrangian particle locations in phase space superimposed on surface growth rate, for the two different pressure cases and without sidejet injection. It can be seen that in the 3 bar case, the trajectories are such that all particle types traverse to regions of high soot surface growth. On the other hand, the Type 2 and 3 particles in the 5 bar case only rarely reach the high soot production regions, and are in general traversing fuel-lean parts of the phase-space. More importantly, the Type 1 particles in the 5 bar case traverse a greater distance along low temperature zones, as shown by the cluster of data points near the low progress variable region. As a result, even though the soot growth rate is considerably increased due to the pressure (roughly a factor of 2), the lack of sufficient number of fluid trajectories in such regions lead to a suppressed increase in soot formation. Hence, the conventional pressure scaling of $P^{1.7}$ (*McCrain and Roberts* (2005)) is not directly translatable to turbulent combustor. This suggests that there exists a separate hydrodynamic scaling, separated from the kinetic-controlled pressure scaling, which alters the rate of increase of soot with pressure.

3.4.4 Grid Convergence Study

The computational mesh used for this study is shown in Figure 3.25. A fully unstructured mesh with tetrahedral cells is used. Near the walls, five layers of prism-shaped pentahedrons are used to capture the boundary layers. The mesh is refined close to the jet inlet but is coarser further downstream where the gradients are smaller. Three mesh resolutions are tested: 6, 12, and 77 million mesh. On the denser mesh, a refined zone is added close to the inlet where flow experiences high shear from multiple inlet ports. The mesh quality is assessed using Pope's criterion (*Pope* (2001, 2004)) and plotted in Figure 3.25. While further mesh resolution might be needed along the central air passage below the fuel nozzle, the denser 12 million mesh significantly improves the resolution in the primary flame and soot nucleating region. Further

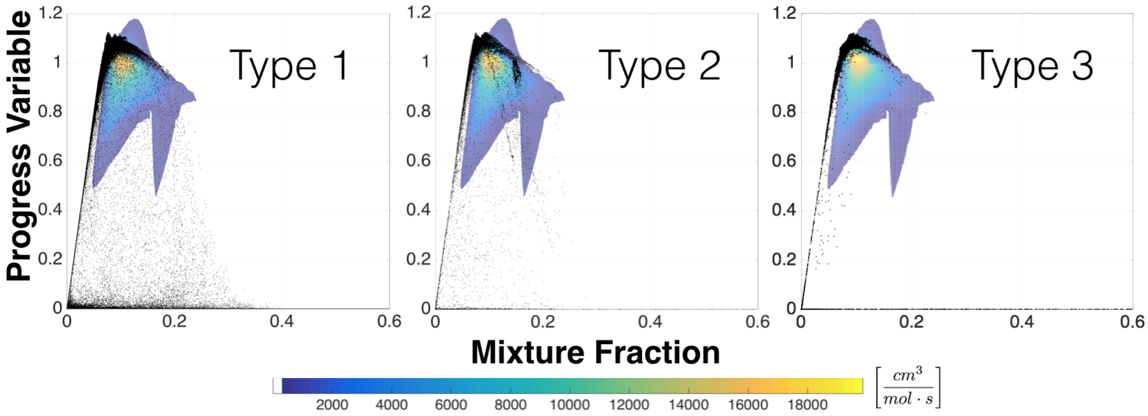

(a) 3 bar

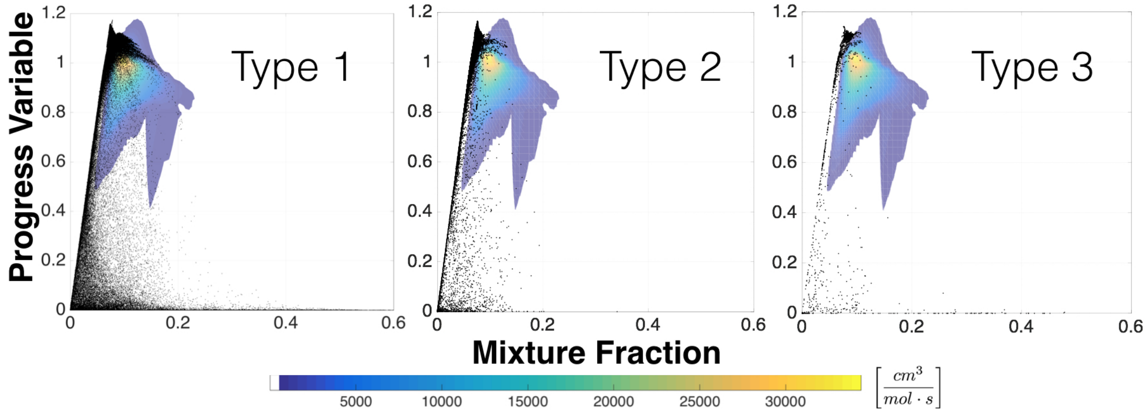

(b) 5 bar

Figure 3.24: Comparisons of lagrangian particle trajectories (scatter) in progress variable-mixture fraction phase space by particle type for 3 and 5 bar cases, without sidejet. Colored contour of soot surface growth rate is shown in the background with corresponding color legend.

refinement to 77 million mesh did not produce significant change in results. For this study, the 12 million cell case is used.

Velocity and soot volume fraction convergence for the 3 different meshes of increasing resolution are also seen in Figure 3.26 and 3.27. From 6 mil to 12 mil mesh, it is clear that the soot volume fraction reduces by a factor of 2. This decrease is attributed to the change in numerical dissipation. With a higher resolution, the dissipation rate captured is higher, which reduces the PAH concentrations that cause soot mass addition.

The LES computations were performed on 1024 cores, with each simulation starting from a non-reacting steady state solution and requiring roughly 100 wall-clock hours to reach sufficient number of flow-through times for averaging and further analysis. Statistics were collected for roughly 20 flow-through times, computed based on the mean axial velocity and length of the domain. It should be noted that this averaging time is sufficient for gas-phase statistics, such as those related to velocity and thermochemical state, but soot fields take much longer to converge as will be shown in the next section.

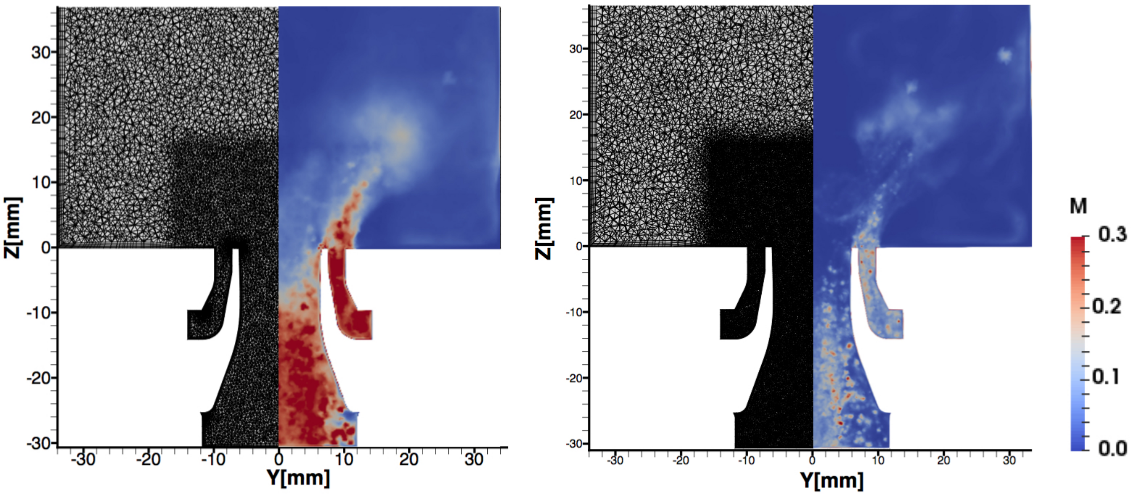

(a) 6 million mesh (b) 12 million mesh

Figure 3.25: Pope's criterion as a fraction of sub-filter kinetic energy over the total kinetic energy for the coarse and dense mesh with refinement at the centerline inlet core.

3.4.5 Temporal convergence of soot statistics

Since soot evolution occurs over longer time scales compared to gas-phase oxidation of fuel, temporal convergence of soot statistics needs to be determined. For this purpose, simulations were carried over a 200 ms time-period, which is approximately equivalent to 8 flow-through times, estimated based on the inflow velocity and the axial length of the combustor. Figure 3.28 show ensemble averages over progressively

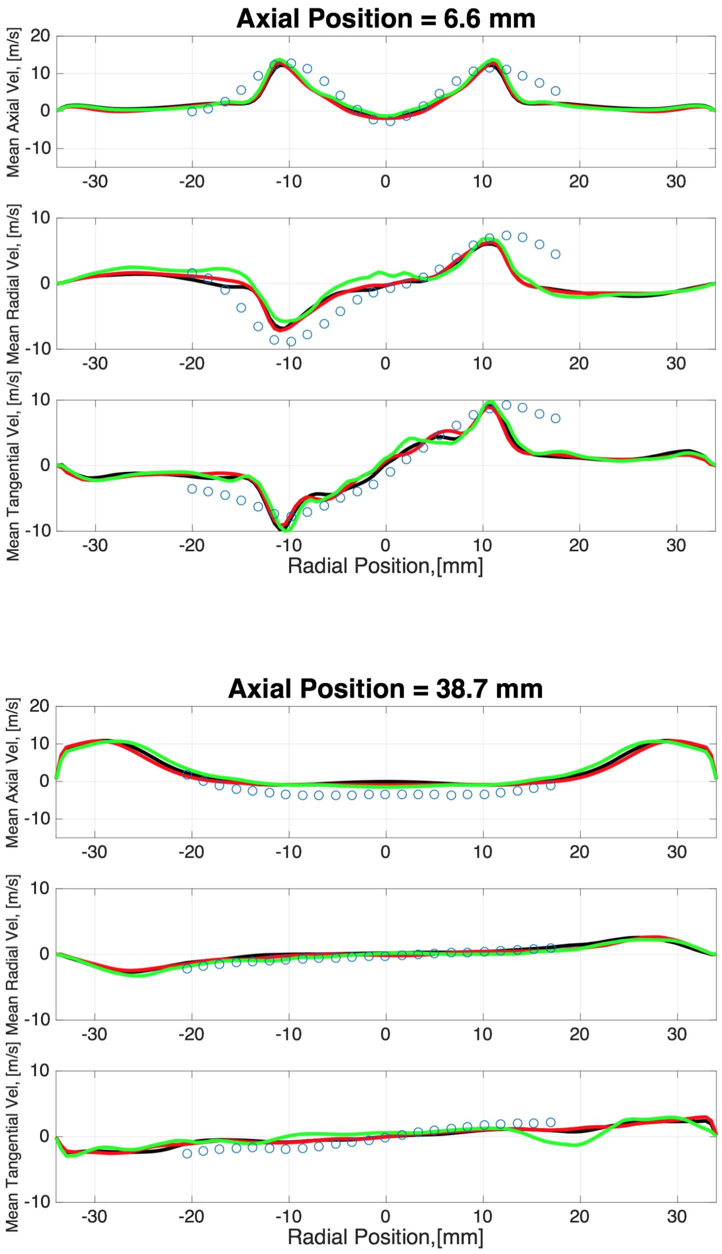

Figure 3.26: Velocity convergence test for the 3 bar case without sidejet at 6 million (black line), 12 million (red line), and 77 million (green line) mesh with experimental data (circle).

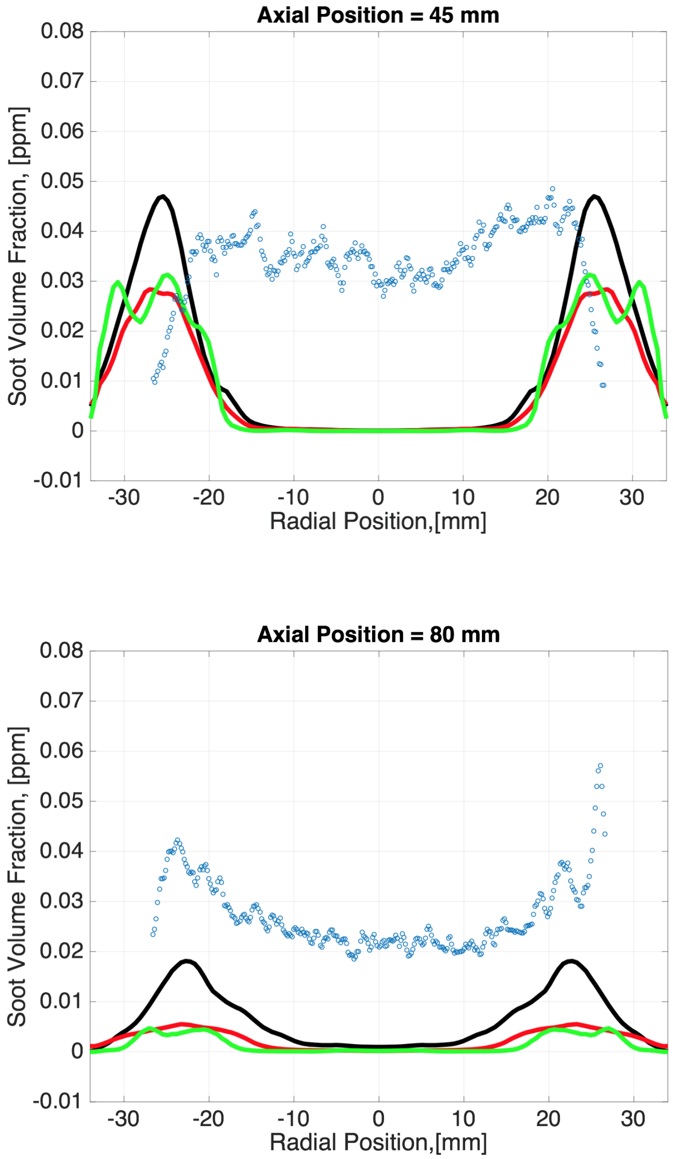

Figure 3.27: Soot volume fraction convergence test for the 3 bar case without sidejet at 6 million (black line), 12 million (red line), and 77 million (green line) mesh with experimental data (circle).

longer simulation times. It is seen that although gas-phase statistics converge within 100 ms, the soot statistics take much longer, and appear statistically converged only after 135 ms.

In Figure 3.29 and Figure 3.30, radial profiles of soot volume fraction converged using different averaging times are plotted. It is seen that soot volume fraction increases in certain regions of the combustor with averaging time, especially over the central air flow region (at the center of the IRZ), where fluid velocities are relatively low. As averaging time increased from 103 ms to 172 ms in Figure 3.28, it is found that the soot volume fraction field becomes more compact (radially), as expected of a stabilized flame and flow field where nucleation at the middle of the chamber accounts for the soot volume fraction increase in the region.

3.5 Summary

LES of soot formation in realistic gas turbine combustors was performed for four different cases, including two pressure conditions, with and without sidejets. From a computational perspective, it was found that soot statistics have to be converged over time-scales much longer than that for the gas-phase flow field. This is predominantly due to the presence of low-frequency unsteady events that generate large soot volume fractions. In other words, if the joint-probability of all states of the combustor are considered, the tails of this distribution influence soot mass inside the system.

The simulations predict gas-phase statistics such as flow-field information quite accurately. While the comparisons with temperature profiles could be better, simulation data is still generally within one sigma standard deviation of experimental measurements. Soot statistics show some interesting trends. First, the spatial structure of soot formation is nearly well-captured, although pockets of high soot mass in the IRZ are not present in the simulations for the 3 bar case without sidejet. The effect of sidejets is also captured, including the reduction in soot concentration as well

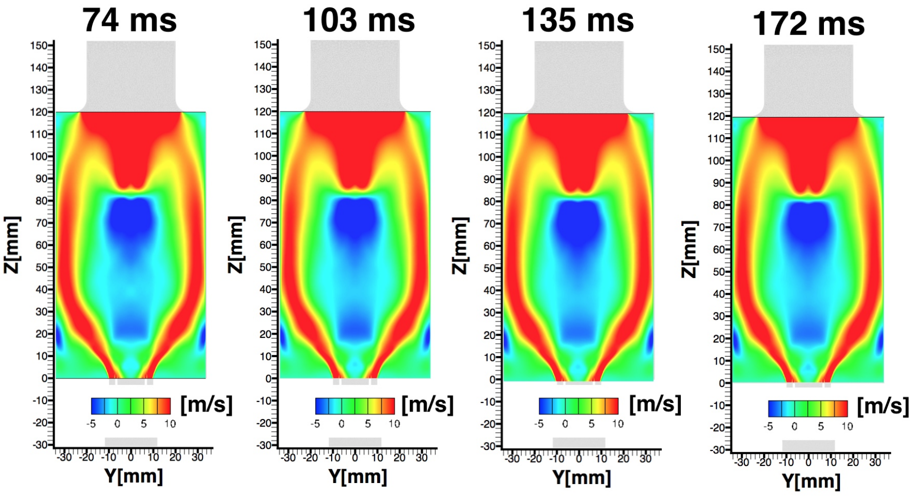

(a) Mean Axial Velocity

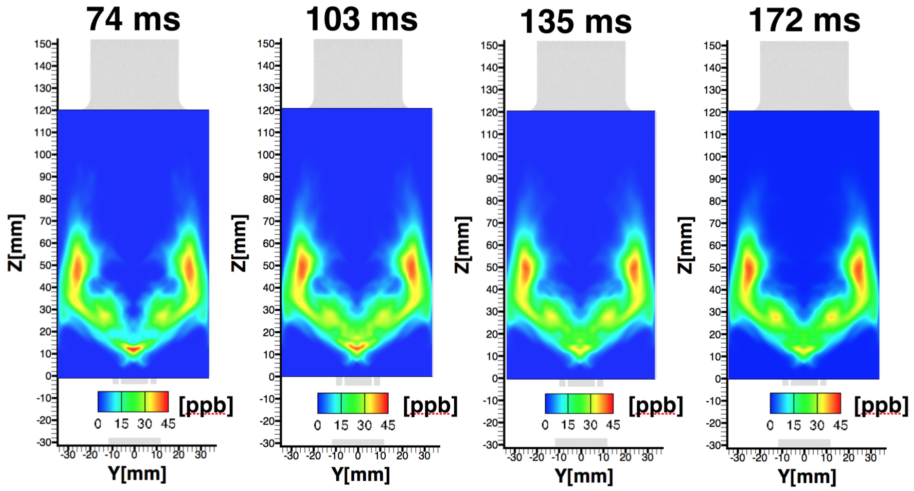

(b) Mean Soot Volume Fraction

Figure 3.28: Timeline of convergence for mean axial velocity and soot volume fraction for 3 bar pressure with sidejet.

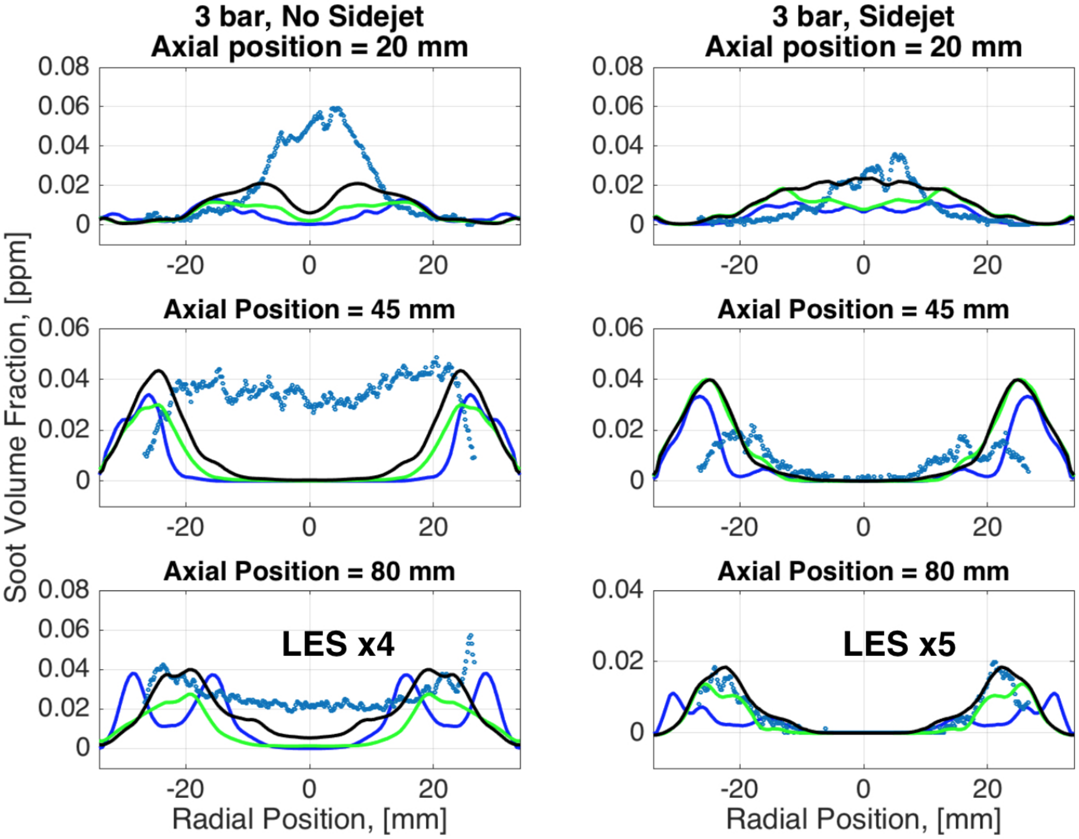

Figure 3.29: Mean soot volume fraction and convergence timeline for 3 bar case compared to experimental data (scatter). LES simulation lines with total averaging times of 70 ms (blue), 140 ms (green), and 200 ms (black) are shown.

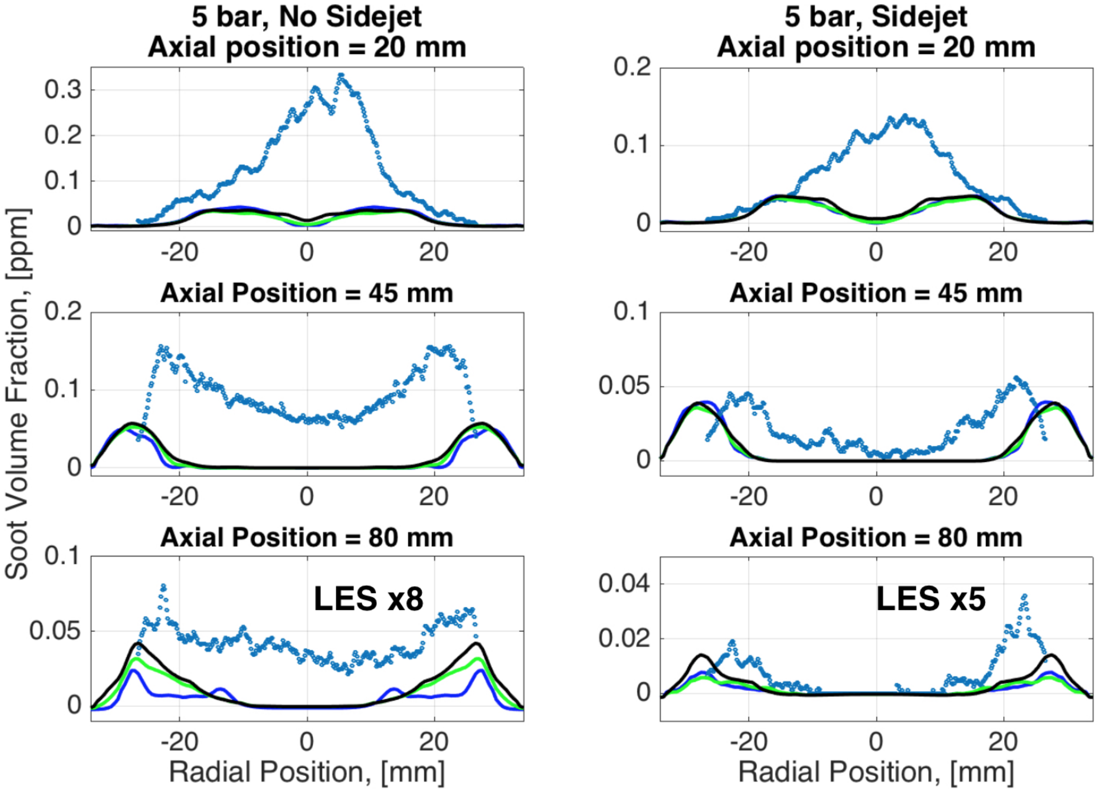

Figure 3.30: Mean soot volume fraction and convergence timeline sequence for 5 bar case compared to experimental data (scatter). LES simulation lines with total averaging times of 70 ms (blue), 140 ms (green), and 200 ms (black) are shown.

as the decrease of soot volume in the shear layer downstream. Second, the quantitative comparisons show that soot is underpredicted, but the values are much better for this configuration compared to simulations using identical models but for canonical jet flames.

These simulations reveal two key features of soot formation in a gas turbine environment. Unlike in canonical jet flames, soot mass addition is driven by acetylene-based growth, which is less sensitive to local strain-rates. Further, swirling flows at high Reynolds numbers exhibit inherent unsteadiness that can lead to sporadic (intermittent) fluid trajectories that promote soot growth. In the configuration studied here, such generation is through the side-to-side motion of the fuel jet, which results in fuel-rich pockets being lobbed-off and transported to low velocity, soot-promoting regions. Interestingly, such intermittency is observed both in the experiments utilized here, as well as in other studies of soot formation (*Qamar et al.* (2009); *Mueller et al.* (2013)).

From lagrangian particle trajectory analysis, it is revealed that without sidejets, a higher percentage of notional particles are entrained into the IRZ (Particle Type 3) at 3 bar pressure. These particles in the recirculation zone experience highly intermittent soot production and oxidation source terms with large residence times. Increasing the pressure changes the hydrodynamic field and behavior of particle trajectories, with less particles being entrained into the IRZ. Thus, at different pressures and flow field, these particles traject a different mixture fraction-progress variable phase space, leading to differences in soot mass addition.

Such unsteady-motion driven soot formation adds a hydrodynamic mode to the scaling laws for soot formation associated with pressure changes. In laminar ethylene flames, $P^{1.7}$ has been observed, with some variation in the exponent based on the metric used. While there is an increase in soot concentration in the gas turbine combustor as well, this increase is also linked to the change in unsteadiness with pressure. In particular, if an increase in pressure (and hence, Reynolds number) reduces the intermittent jet flapping, it might actually lead to a reduction of overall soot formation. Such hydrodynamic causation cannot be observed even in canonical turbulent flames, since large scale unsteadiness is linked directly to the geometry and is not universal in nature. Similar to thermoacoustic instabilities, there is a need to understand the role of such large-scale driven features on soot formation. Perhaps, variations in the configuration including changes to the inflow can be used to assess this feature more systematically. Such investigations are left for future studies.

CHAPTER IV

Fourier Analysis of Turbulent Sooting Flames in Complex Configurations

4.1 Introduction

In aerodynamically-stabilized gas turbine combustors, a swirl-dominated recirculation zone is often used to ensure flame stability. The recirculation zone brings in reacted products at high enthalpy into the fresh mixture of gases injected upstream, leading to combustion stability. Due to their nature, recirculation zones are associated with low velocities, and combined with high gas-phase temperatures can promote the formation of carbonaceous particulates in the form of soot. While this general behavior is intuitive, the exact mechanism of soot generation is not fully understood. Soot particles could be trapped in these recirculation zones with a long residence time, forming larger soot agglomerates, or experience soot oxidation recirculation zones with high OH species concentrations. Prior studies (refer to *Raman and Fox* (2016) for discussion on related studies) show that soot formation is intermittent in nature, driven by the strong coupling between soot precursor formation and the scales of turbulent flow. Similar soot intermittency is observed in the recirculation zones that is not present in the high-strain neck region or downstream jet-like region, consistent with larger time and length scale-type configurations like the combustor.

Understanding the role of recirculation zones in this study can lead to a better understanding of soot intermittency and how this long time-scale, low-frequency event affects soot time-averaging.

The model combustor studied here is the experimental configuration of *Geigle et al.* (2015), which is designed to replicate a rich-quench-lean (RQL) combustor configuration. Previously, *Chong et al.* (2018a) have studied this configuration using the Mueller approach, where different flow conditions including operating pressures were considered. The focus of that study was to determine the predictive capability of the LES approach. It was shown that the simulations reproduce gas phase experimental data reasonably accurately, and captures the qualitative trends in soot distributions. Further, the dominant mode of soot mass generation is shown to be acetylene-based surface growth, with up to almost an order of magnitude higher soot source terms compared to nucleation and condensation processes. It was also discovered that soot formation is driven by the interaction between the fuel jets and the recirculation zones. However, that analysis did not consider the time-scales associated with recirculation, and the particular evolution pathways for soot in this context.

With this background, the goals of this study are as follows: a) identify the time-scales associated with soot formation in swirl-stabilized aircraft combustor-like configurations, b) illustrate the mechanism that causes intermittency of soot formation, and c) determine criteria for temporal convergence of soot statistics. For this purpose, the LES approach with detailed kinetics models will be utilized. Further, a Lagrangian particle tracking approach will be used to determine the path of soot particles inside the recirculation zones. The rest of the sections are laid out as follows. First, the simulation methodology and details of the flow configuration are provided. Then, results from the study of recirculation zones are presented, followed by analysis of temporal spectrum. Next, the issue of time-averaging in such flows is discussed. Finally, conclusions are provided. Note that the novelty of this study lies in investigating the time-scales of soot formation in a combustor. Comparisons of time-averaged simulation results with experimental observations have been conducted and extensively analyzed in Chong et al. *Chong et al.* (2018a) and will not be repeated in this study. Overall good comparison of velocity, temperature, and soot volume fractions has been achieved for this case compared to the experimental data.

4.2 Simulation Methodology

The large eddy simulation (LES) solver used in this study has been previously used in several studies related to soot formation (*Koo et al.* (2015, 2016b, 2017); *Chong et al.* (2018a)). Further, detailed analysis of the numerical properties of the approach has been studied in *Hassanaly et al.* (2018). In this section, only a brief description is provided, in an effort to aid the discussion below.

The LES approach uses a low-Mach number collocated mesh formulation, implemented in OpenFOAM (ope (2017)), a C++ code for solving partial differential equations. This umFlameletFoam (*Hassanaly et al.* (2018)) with soot coupling has been applied to a number of combustion systems, such as a premixed burner (*Tang et al.* (2016)) and studies of the current combustor (*Chong et al.* (2018a); *Koo et al.* (2015, 2016b, 2017)). This solver minimizes dissipation of kinetic energy by using the variable density scheme of *Morinishi* (2010). Consequently, it is useful for inherently unsteady flow problems, where turbulent fluctuations are the dominant physical mechanism that control the evolution of any quantity of interest.

Since LES only resolves the large scales, combustion and soot formation has to be extensively modeled, including the interaction between the chemical processes and the small-scale turbulent flow. For gas-phase combustion, the flamelet/progress variable with radiation coupling (RFPV) method is used as described in Section 1.3. The gas phase combustion and PAH chemistry is described using the detailed mechanism of *Narayanaswamy et al.* (2010).

The soot model used in this study is the Hybrid Method of Moments (HMOM) according to Section 1.2.3.5.

4.3 Combustor Configuration

The DLR model aero-combustor configuration used in this study is based on the high-pressure combustors studied by *Geigle et al.* (2015) and the same combustor used in Chapter 2.5. The combustor geometry is shown in Fig. 4.1 with typical streamlines in the combustor from inlet to outlet. It was designed for operation at 10 kW/bar power and installed with large optical access for simultaneous acquisition of velocity, temperature, species mass fractions and soot volume fraction using laser diagnostics tools. It has a cross-sectional area of 68 x 68 mm^2, with a height of 120 mm. The inflow consists of three concentric nozzles: two room temperature air inlets with swirling velocity and 60 annular straight channel fuel (C_2H_4) inlets in between the two air flows with a size of 0.5 x 0.4 mm^2 each. A single constricted exit of diameter 40 mm removes the combustion products.

In this study, the specific case of 3 bar operating condition, specified in Table 4.1, is simulated. The global equivalence ratio is approximately 1.2, which is below the sooting limit but the slight fuel rich condition could produce high volumes of soot if fuel-air mixing is inefficient. Hence, any soot particle observed is generated due to local inefficiencies in mixing and oxidation of the fuel. Further, an adiabatic boundary condition is used for the case simulated in this study.

P (bar)	Q_{air} (slpm)	Q_{fuel} (slpm)	Q_{ox} (slpm)	ϕ
3	140.8(central)+328.5(ring)	39.3	0	1.2

Table 4.1: Operating condition for the simulated case. ϕ indicates global equivalence ratio. Flow rates are referenced at 1.013 bar and 273 K. Fuel and air inlet temperatures are 300 K.

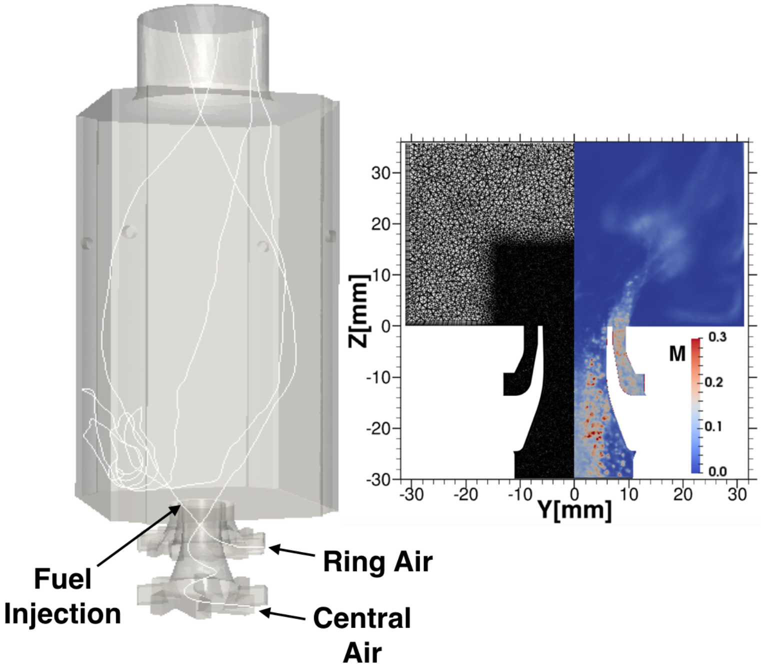

Figure 4.1: DLR combustor geometry with fuel and air inlets marked. White lines are particle trajectories from Lagrangian approach originating from the inlets, showing pathlines of velocity in the combustor. Inset figure shows the unstructured mesh and refinement process at the inlet with the Pope's criterion, M.

The computational domain consists of approximately 12 million tetrahedral cells, with grid refinement applied near the inlets and the near-wall region, as shown in the inset figure in Fig. 4.1. In LES, it is necessary to resolve the smaller-scale structures, and a metric for such refinement is Pope's criterion (*Pope* (2001, 2004)). A fractional energy M, defined as the ratio between the sub-filter kinetic energy and the total kinetic energy is used to determine the resolution adequacy. Since the sub-filter kinetic energy is not directly available from the resolved fields, a model is used to estimate this quantity. The cell-size is refined until this ratio is below 0.30 everywhere in the domain. Further details about the configuration, computational domain and grid refinement process can be found in *Geigle et al.* (2014, 2015, 2017); *Chong et al.* (2018a); *Koo et al.* (2015, 2016b, 2017).

4.4 Results

4.4.1 Soot Source in Recirculation Zones

The main recirculation zones are positioned in the four bottom corners of the combustor and in the center of the combustor. Figure 4.2 shows the recirculation zones in the combustor. The inner recirculation zone (IRZ) is characterized by the large volume of low negative axial velocity in the center of the combustor. The outer recirculation zone (ORZ) is characterized by the compactness and close distance to the bottom and side walls. The two regions are separted by the inflow jets (of fuel), which creates a shear region, with fuel-rich fluid at relatively high temperatures. This shear region is the main source of particle nucleation. However, it is the entrainment of these particles into the IRZ and ORZ that contol the amount of soot generated in the combustor. It should be noted that due to relatively low equivalence ratio (below the sooting limit), the amount of soot exiting the combustor is negligible, since oxidation processes convert the particles to CO_2 downstream of the recirculation zones.

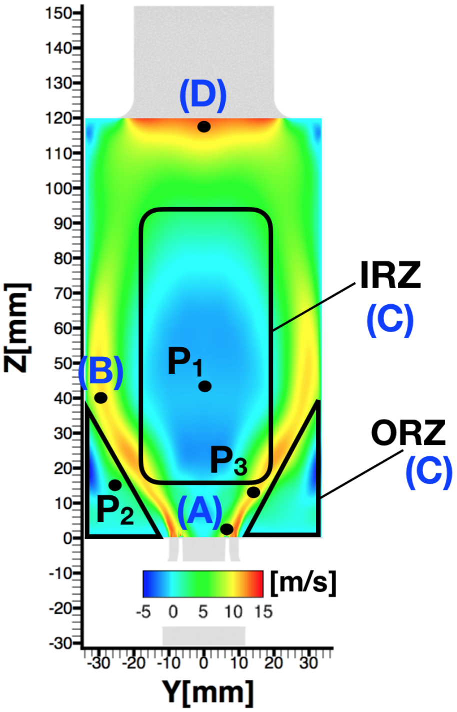

Figure 4.2: Regions of inner and outer recirculation zones specified in midplane slice of the axial velocity field. Point probe for spectral analysis and LPT point source positions are also indicated by P and bracketed (A,B,C,D) labels respectively.

From prior studies (*Chong et al.* (2018a); *Eberle et al.* (2015)), it is known that although these zones are easy to decipher based on time-averaged data, there is large variability in their location, size and strength. This is mainly the result of the chaotic fuel-jet breakdown process, which leads to variations in the main heat release locations. Further, the turbulence introduced through the air inflow ports lead to a highly dynamic environment, where fluid trajectories exhibit strong temporal variations, even when starting from identical spatial locations.

One approach to characterizing this temporal behavior is through the use of particle tracers, which follow the local fluid trajectories. In this study, this Lagrangian particle tracking (LPT) approach is used, whereby 1000 notional particles are introduced into the domain from a fixed location (point A in Fig. 4.2). The injection point is located directly above the fuel port. The source of injection is a sphere of diameter 0.5 mm with the particle positioned at the surface of the sphere. Particles are tracked for approximately 50 ms, sufficient to determine the trajectory of each particles until it reaches the combustor exit. The symmetry of injection in the combustor justifies the use of a point source location instead of a larger coverage across the inlets. The notional particles are advanced in space using local flow velocity and at each time-step, the gas-phase properties and soot quantities associated with the local Eulerian field are stored. Time along the particle trajectory is defined as the residence time. It should be noted that the initial location is very near the fuel inflow port, but the notional particles were found to traverse highly variable trajectories within the combustor.

Figures 4.3 and 4.4 show two extreme trajectories of interest here. Both trajectories spend considerably more time within the combustor as compared to the mean residence time, which is roughly 25 ms. It can be seen that the IRZ trajectory follows a path from the fuel port towards the shear layer close to the sidewall, before being entrained into the IRZ. However, the maximum soot volume fraction is observed as the particle moves towards the sidewall, where the fluid trajectory (which starts on the rich side of the jet) interacts with the hotter recirculating flow. As the particle moves back into the recirculation zone, some level of oxidation appears to reduce the total soot content, possibly driven by the higher OH content in the product mixture.

The soot trajectory in the ORZ follows an even more complex path. It is seen that when the fluid particle is first entrained into this region, the soot volume fraction is quite low, indicating that only nascent particles are being processed by this zone. Firstly, the particle goes through similar trajectory in the fuel-rich shear layer to the sidewalls, experiencing large soot production. Then, the particle undergoes several cycles of recirculation (denoted by cyclical motion in the axial-radial coordinate plane). As the particle moves into the ORZ, there is a large reduction in soot volume fraction, indicating partial oxidation. Finally, the particle is ejected from the zone, and as it crosses the shear layer, it experiences another soot growth event.

These results show that a simplistic view that soot is generated in the recirculation zone is not supported by the simulations. Rather, even when fluid trajectories are entrained into these zones, only sporadic events cause soot growth. Such events are driven predominantly by the presence of fuel-rich zones. However, the presence of the recirculation zones increases the odds of finding such trajectories due to the large total time spent by the fluid particle trapped inside the circulation vortices. Clearly, with richer fuel/air equivalence ratios, different patterns of soot formation will be observed (*Chong et al.* (2018a)). Furthermore, if the recirculation zone mixture fraction is increased, significant soot growth could be detected. The effect of mixture fraction is left for future studies.

4.4.2 Low Frequency Soot Accumulation and Dispersion Events

To understand the LPT results in the context of the flow field, it is useful to consider the evolution of soot pockets within the combustor. Figures 4.5 and 4.6 show

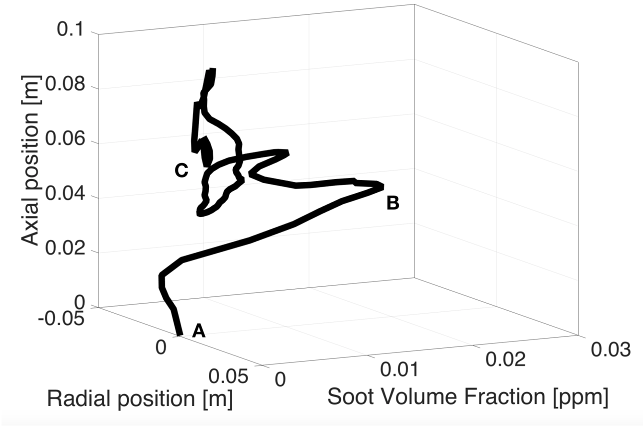

Figure 4.3: Lagrangian particle tracking analysis of mean soot volume fraction for particles entrained into the IRZ for 50 ms total residence time. Labels indicate progression from A (fuel inlet) to B (sidewall shear layer) to C (IRZ). Intermittency of soot growth and oxidation is shown in the IRZ.

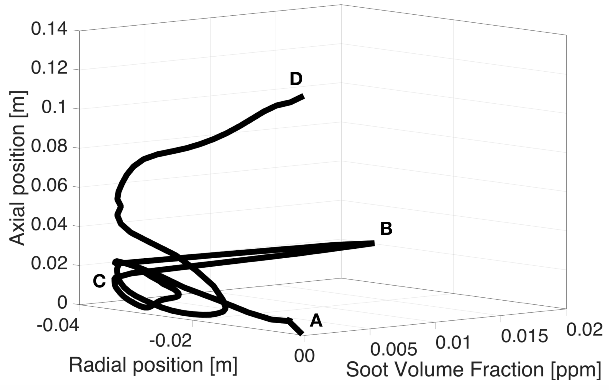

Figure 4.4: Lagrangian particle tracking analysis of mean soot volume fraction for particles entrained into the ORZ for 50 ms total residence time. Labels indicate progression from A (fuel inlet) to B (sidewall) to C (ORZ) to D (outlet). Entrapment of particles in the ORZ for a large residence time and the reduction of soot volume fraction is shown from B to C.

snapshots of soot volume fraction and mixture fraction superimposed by stoichiometric mixture fraction isocontours. The time sequence spreads 51 ms, which is roughly 2.5 times the residence time in the combustor. The soot pockets are highly dynamic, but also spatially intermittent with only small regions of the combustor supporting large soot volume fractions at any given instant.

In line with the LPT analysis, it is seen that soot formation is preferred near the edge of the shear layer, but in the IRZ region rather than the ORZ. This is because intermittent higher mixture fraction regions are more readily available closer to the IRZ compared to the ORZ as shown in Fig. 4.6. However, at certain instances, small pockets of soot are formed in the ORZ (for instance, near the right wall at 20mm height and 51 ms time). This implies that the fluid particles entrained into the IRZ have a higher chance of generating soot mass. In other words, even though the ORZ features very long residence times, and has sufficiently high temperature (not shown here), the lack of access to fuel-rich pockets leads to low amount of soot formation.

Another important feature of this recirculation zone is the accumulation and dispersion cycle. As shown in Fig. 4.5, the ORZ periodically contains very little soot, concentrated essentially at the downstream edge of the recirculation zone. From this point, initial soot growth happens near the upstream edge of the ORZ, followed by convection towards the side walls along the shear layer. Finally, these pockets are entrained again into the upper edge, where higher oxidation rates remove most of the soot particles. The accumulation phase is initiated by the lower edge of ORZ while dispersion or ejection of soot particles occurs at the upper edge. This process is extremely slow compared to the mean residence time, and can occur over 2-3 times longer duration compared to the flow time-scales.

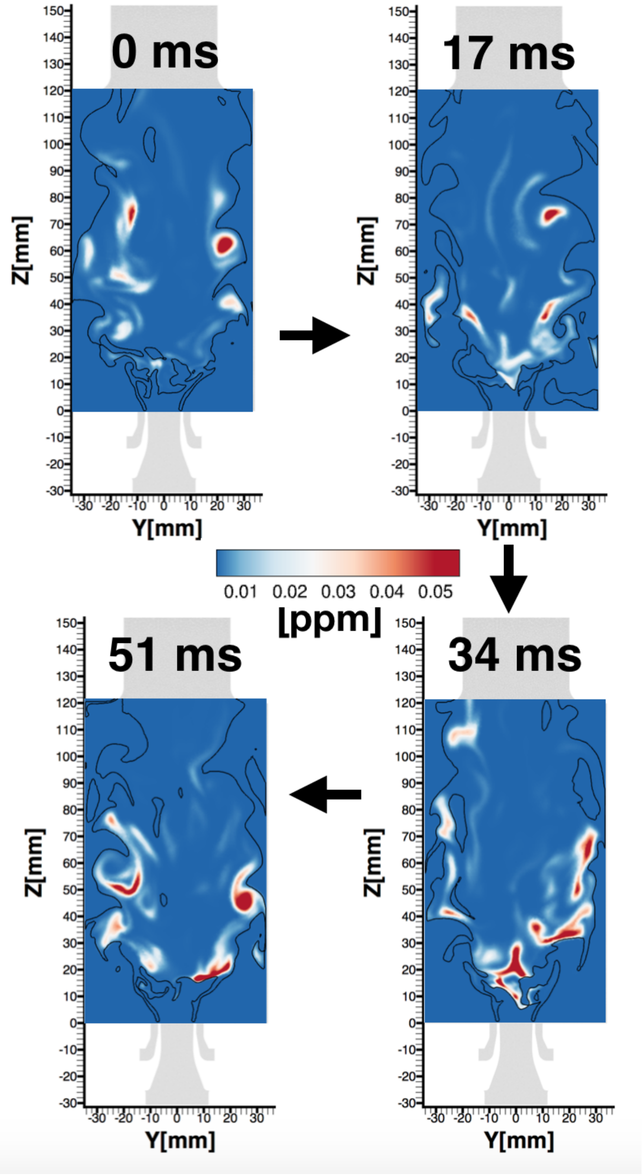

Figure 4.5: Snapshots of soot volume fraction separated by 17 ms showing low-frequency soot transport into IRZ and dispersion event. Stoichiometric mixture fraction line is overlaid.

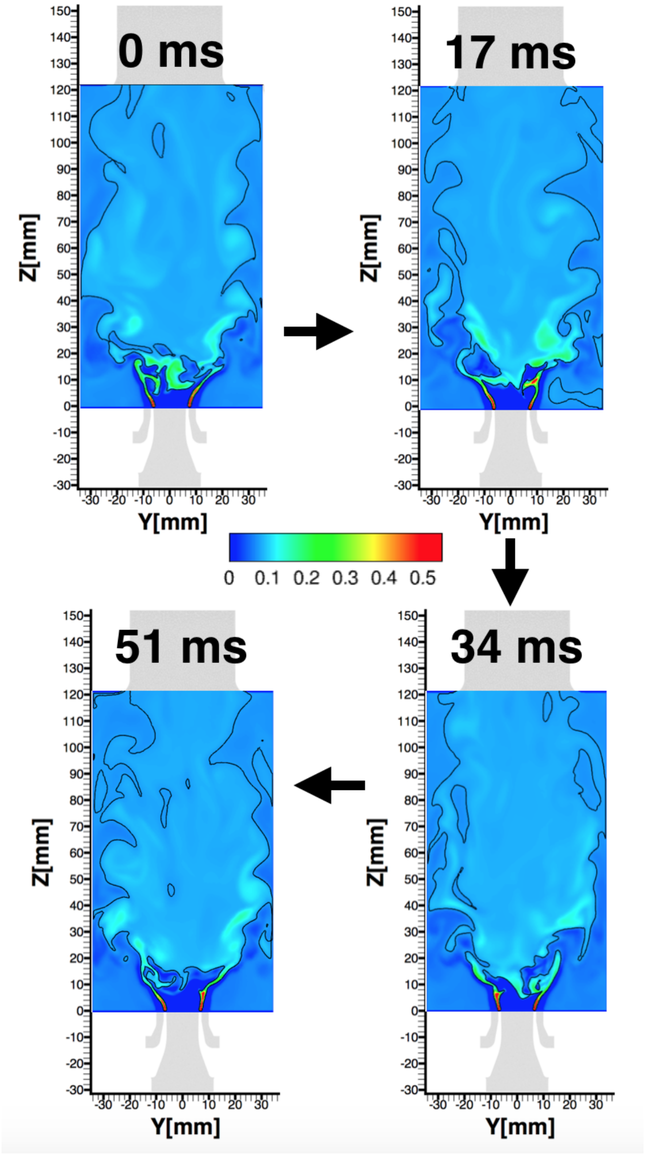

Figure 4.6: Snapshots of mixture fraction separated by 17 ms. Stoichiometric mixture fraction line is overlaid.

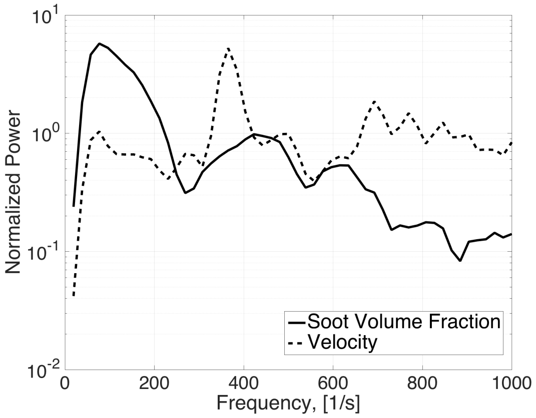

Figure 4.7: Spectral analysis of velocity and soot volume fraction using one point probe time history discrete fourier transform in the IRZ at point P_1 in Figure 4.2.

4.4.3 Spectral Analysis of Combustor

In complex swirling flows, the dynamics of any single process is intricately linked to the overall flow features. To understand this coupling, power spectrum of different quantities are computed. Figures 4.7-4.9 show the power spectrum computed at points P1, P2 and P3 shown in Fig. 4.2. A Windowed Fourier Transform is performed on the single-point data to decompose the data to the frequency space shown in this section.

There are many interesting features found in the power spectra. First, the velocity spectrum shows a dominant frequency of roughly 340 Hz, which is seen both in the IRZ and shear layer spectra, but is absent in the ORZ spectrum. Prior studies of similar combustors operating in the partially-premixed mode (as in this study), have shown that precessing-vortex cores (PVCs) are often present in the system (*Eberle et al.* (2015); *Stöhr et al.* (2009)). This is the first known study of the PVC frequency for the current configuration and at the operating conditions stated in Table 4.1. Visual analysis of axial velocity (not shown here) clearly show a PVC that is bounded by the shear layers seen in Fig. 4.2. As a result, the dominant velocity frequency is observed mainly in the IRZ and shear layer spectra. Further, these spectra also shown other

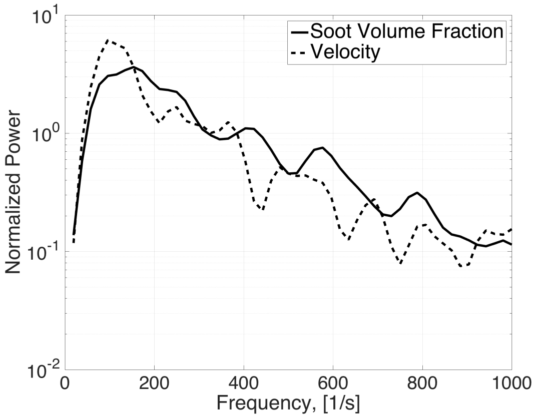

Figure 4.8: Spectral analysis of velocity and soot volume fraction using one point probe time history discrete fourier transform in the ORZ at point P_2 in Figure 4.2.

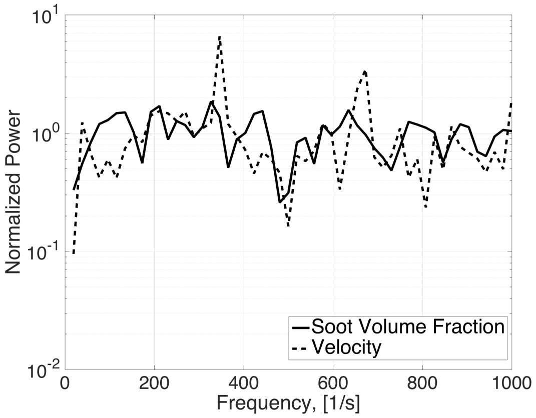

Figure 4.9: Spectral analysis of velocity and soot volume fraction using one point probe time history discrete fourier transform in the shear layer at point P_3 in Figure 4.2. There is no single dominant frequency mode for soot for this location.

harmonics present at higher frequencies. Currently, no experimental data on the temporal evolution of velocity and soot quantities are available for comparison on the PVC frequency. This study aims to bridge this gap in knowledge of the PVC frequency in the combustor by probing and analyzing data not available experimentally.

The soot spectra are markedly different, and show a dominant frequency mainly for the IRZ. However, this frequency is much lower than that of velocity, and peaks at around 77 Hz. This indicates that even when precession is present, soot dynamics are affected both by hydrodynamics and the chemical physics associated to particulate evolution. Further, this dominant mode disappears in the shear layer, where the effect of precession is visible in the velocity spectrum. One reason could be that soot formation in this region is dominated by the strain-rate associated with the shear layer, and soot processes transition to a jet-type mechanism. As a result, the impact of PVC is not seen in the formation processes.

The ORZ presents a different scenario. Here, both the velocity and soot spectra are relatively smooth, with decreasing content with increasing frequency, which is typical of a turbulent flow. Further, the spectra are smoother, with no dominant peaks. This is similar to a stirred-reactor configuration with imperfect mixing. Consequently, soot spectrum scales relatively similar with the velocity spectrum.

If time-averaged statistics are of interest, then such low frequency dynamics will impact the total simulation time. For instance, Fig. 4.10 shows the soot volume fraction field after averaging for various length of simulation times. At around 300 ms, the results appear to be fully converged. However, there are incremental changes the field even up to 280 ms. It was also established that additional time-averaging did not change the results.

This long simulation time is related directly to the accumulation/dispersion cycle and the dominant frequency mode found in the spectral analysis. In other words, to obtain a sufficiently converged statistics, certain total number of such events have to

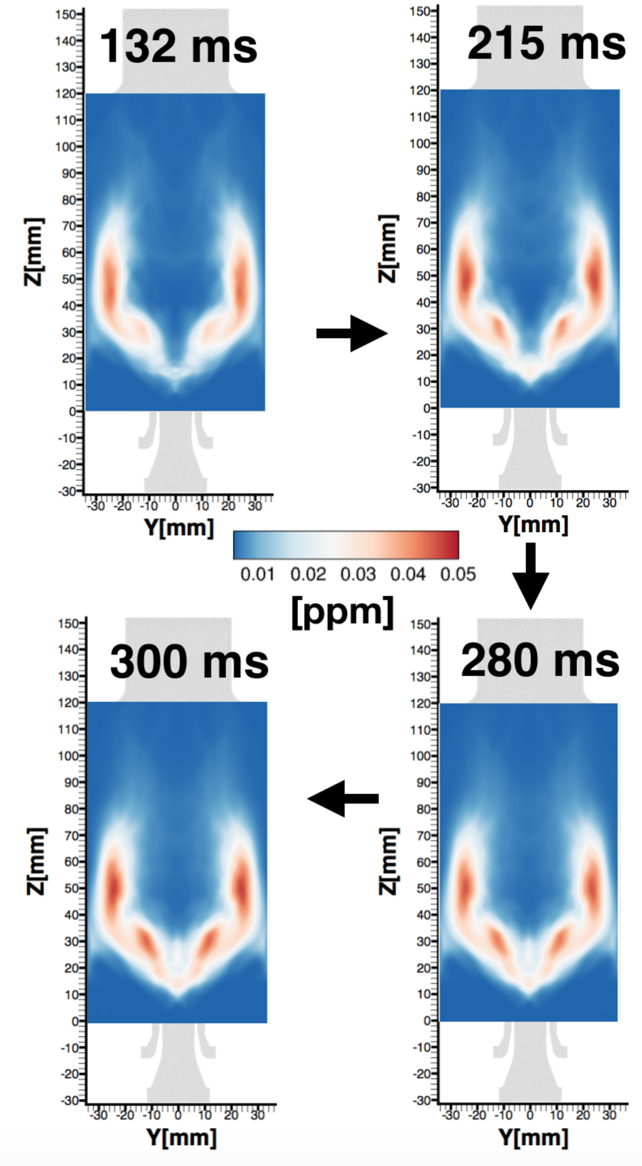

Figure 4.10: Sequence of time-averaged soot volume fraction. 280 ms is regarded as the minimum total time-averaging required for soot quantities.

be captured. For this particular case, where the dominant frequency is $f_{soot} = 77Hz$, the time-scale associated with one event is given by $tau = 1/f_{soot}$, which is around 13 ms. On the other hand, the dominant frequency for the velocity field is roughly 346 Hz, which implies a nearly 4.5 times faster cycle time.

Combining this information with the time-averaging result, it is seen that more than 20 cycles are needed to obtain converged soot statistics. While this quantity is bound to change with combustor geometry and the complexity of the flow field, even this value imposes a significant computational burden, especially when using high-fidelity tools such as LES.

4.5 Summary

LES calculations were used to determine the role of recirculation zones on soot formation. LPT analysis was used to track fluid trajectories originating from the fuel port in an effort to quantify the relative roles of the different fluid zones within the combustor. Statistically converged fields were collected by sampling for long simulation times.

This study provides three main conclusions:

1. While recirculation zones provide long residence times, this is not sufficient to increase soot formation. In fact, even with the recirculation zones, very small regions confined to the jet-like shear layers were needed to form nascent soot particles. Hence, the presence of low velocity high temperature zones is not a direct predictor of soot formation.

2. Due to the inherently slow chemistry, soot formation is decoupled from the dominant flow modes in certain regions of the flow. For instance, in the IRZ, the velocity mode is at much higher frequency than the soot generation mode. On the other hand, soot has no preferential mode in the shear layer region, although the

velocity field shows a dominant frequency. Overall, an accumulation/dispersion cycle in the IRZ is responsible for the bulk of soot mass generated within the combustor.

3. Obtaining statistically converged soot fields is particularly challenging due to the low frequency accumulation/dispersion cycle. In the current configuration, this cycle was found to last roughly 13 ms, which is 4-5 times the fluid time scales. Further, many such cycles (roughly 20) were needed to obtain converged volume fraction profiles. This points to the importance of measuring the dominant low soot frequency mode during the simulation to determine the total amount of simulation time needed to accurately acquire the time-averaged data.

CHAPTER V

Summary

This dissertation has pushed for the advancement in soot modeling and soot evolution in turbulent sooting flames with the end goal of being able to accurately simulate the soot evolution in an aircraft combustor. In Chapter I, the state of the art in soot modeling is briefly described including the advantages and disadvantages of each model. In Chapter 1.2, the soot models and their formulations are described in detail. The soot chemistry from nucleation to coagulation to surface growth to PAH condensation to soot oxidation are also described.

In Chapter II, soot-turbulence-chemistry interactions from small scale to large scale are studied in detail. For small scale interactions, a partially-stirred reactor (PaSR) is developed to represent a single cell in a large computational domain where turbulent time scales like fluid velocity (residence time) and scalar dissipation rate (mixing time) can be enforced. Soot models are easily coupled to the PaSR and effect of soot taken into account in the species mass fraction (sink term for soot precursors). It is found that PAH-based detailed soot statistical models (MOMIC, DQMOM, HMOM and CQMOM) scale similarly to soot quantities, in general with mixing and residence time. Soot statistical model is more important if properties other than soot volume fraction is needed because MOMIC predicts larger particle diameters and lower number density but produces similar volume fraction compared to other statistical models. Comparisons between DQMOM and CQMOM (two quadrature based method of moments) also show CQMOM predicting smaller particle size at the first mode and larger particle size at the accumulation mode compared to DQMOM despite predicting similar soot volume fractions. Further, it is found that chemistry mechanism that produces higher PAH concentrations (soot nucleation agent) also predicts higher soot quantities. In comparing soot models using different soot inception modes, the semi-empirical model (SEMI) that uses acetylene (C_2H_2) as the inception species is less sensitive to fluid flow rate and scalar dissipation rate as C_2H_2 is also less affected by these fluid flow rates. Vice-versa is true for the PAH-based detailed soot statistical models. Among the different mixing models, the interaction by exchange with the mean (IEM) model produces much lower soot volume fraction at stoichiometric mixture fraction as the evolution of mixture fraction with time produces different temperature and species concentrations not conducive for soot formation.

In the second half of Chapter II (Chap. 2.5), soot-turbulence-chemistry interactions in an aircraft combustor is investigated using SEMI, HMOM and CQMOM soot models. This is the first known instance of CQMOM soot model being used in simulating a large scale turbulent combustion device. Differences between the soot models are consistent with the studies in small scale interactions wherein the acetylene-based inception model (SEMI) leads to significantly higher soot volume fraction compared to experimental results and the PAH-based detailed soot statistical models. This large scale simulation complements the small scale PaSR studies in pointing out the difference in the location of soot produced. SEMI predicts large soot mass in the inner recirculation zone (IRZ) of the combustor while the PAH-based detailed models predict most soot mass in the shear layers. Between the two PAH-based models (HMOM and CQMOM), CQMOM predicts higher number density and smaller particle diameter, attributed to a faster coagulation rate in HMOM. In large scale simulations where soot particles reside in the computational domain for a much longer period compared to small scale 0-D simulations, the influence of major mode of soot mass addition (condensation or surface growth) also plays an important role. In this combustor, surface growth via H_2 abstraction C_2H_2 addition (HACA) mechanism dominates and so it accentuates the differences in coagulation rates predicted by the statistical models.

In Chapter III, large eddy simulation (LES) of soot evolution in an aircraft swirl combustor is performed for two pressure and sidejet conditions to understand the soot evolution in a large scale turbulent flame. Unlike in canonical jet flames or bluff body flames, soot mass addition is driven by acetylene-based surface growth, which is less sensitive to local strain rate. From lagrangian particle analysis, it is found that at differnt pressures and flow fields, these particles traject a different mixture fraction-progress variable phase space, leading to differences in soot mass addition. Such unsteady-motion driven soot formatioin adds a hydrodynamic mode to the scaling laws for soot formation associated with pressure changes, in addition to the commonly known chemical reaction effect from pressure. Such hydrodynamic causation is linked directly to the geometry and not universal in nature.

In Chapter IV, it is found from fourier analysis of the soot scalars in the aircraft combustor that soot formation is decoupled from the dominant flow frequency in certain regions of the flow. In the inner recirculation zone, the velocity mode has much higher frequency than the soot mode. On the other hand, soot has no preferential mode in the shear layer or outer recirculation zone, although velocity field shows a dominant frequency. Hence, this lower frequency mode needs to be captured to accurately determine convergence in the soot field.

5.1 Conclusion

In this section, general conclusions and lessons learnt from this dissertation are provided.

- PAH-inception soot statistical models based on the method of moments is the most suited for large scale soot simulations based on numerical efficiency and accuracy of soot quantity predicted. Although different soot models predict soot volume fraction similarly in the numerical sense, soot particle diameter and number density varies depending on the closure model. Hence, when soot quantities other than soot volume fraction is required, the choice of soot model is non-trivial and requires understanding of the flame operating condition (premixed or non-premixed), dominant mode of soot mass addition and the importance of soot oxidation treatment.

- Semi-empirical soot model using acetylene inception is less sensitive to strain rate because acetylene species mass fraction is less affected by strain rate compared to PAH species. Thus, PAH-inception soot models are more strain rate dependent and soot quantities scale accordingly with PAH mass fraction. This difference can be seen in large scale simulations where flow field differences can affect the location of soot formation.

- In a large scale complex configuration like an aircraft combustor, there exists a separate hydrodynamic scaling with pressure that is configuration-dependent. At different pressures and flow fields, lagrangian particles traject a different mixture fraction-progress variable phase space, leading to differences in soot mass addition.

- Last but not least, there exists a separate, lower soot frequency mode that is decoupled from the dominant fluid flow mode in a complex turbulent flame such as an aircraft combustor. The identification of this lower frequency sooting mode is important in simulations where convergence is sought as statistical sooting data is being collected. The dependence on flowthrough times as convergence criteria is less conclusive than using a definitive multiplication of sooting frequency.

5.2 Future Work

This dissertation has advanced the understanding of soot models and the soot-turbulence-chemistry interaction in small and large scale simulations. However, much more work is needed and the few important areas have been identified below.

- Soot oxidation treatment for the soot nuclei has to be present in all models for general use in turbulent sooting flames. The enforcement of the location of the first nuclei mode in HMOM is a promising start to treating oxidation of nuclei particles (sink term for number density of the soot nuclei). Future work could extend the idea to more sophisticated models like CQMOM or ECQMOM although treatment of oxidation negative source term in a kernel function (EC-QMOM) for the soot nuclei will be challenging.

- Implementation of moment method especially in enforcing the minimum weight and abscissas in QMOM-based methods are important and warrants careful investigation e.g. how fluid time step affects moment inversion and subsequently the evolution of these weights and abscissas.

- As pressure increases further and reaches supercritical conditions in combustion devices, soot formation and transport in these extreme pressure, low diffusivity conditions need to be studied. Advancement has been made in the field of supercritical combustion modeling (*Chong et al.* (2017)) and early studies of coupling of real gas equation of state to a combustion model for jet flames has been done by the author and included in Appendix A. Future studies in soot formation and evolution in these extreme conditions is warranted.

APPENDIX

APPENDIX A

Direct Numerical Simulation of Turbulent Supercritical Jet Mixing and Combustion

A.1 Introduction to Supercritical Combustion

Supercritical mixing and combustion is increasingly important to practical combustors, including high-pressure aircraft engines that involve fuel injection at supercritical pressures, rocket combustors that operate at high chamber pressures, and supercritical CO_2 cycle for power generation that involves methane or coal combustion in oxygen (instead of air) but with supercritical CO_2 as the diluent. While much of the benefit from supercritical mixtures comes due to the increased thermodynamic efficiency associated with high operating pressures in the combustion chambers, such fluids also allow efficient transportation. For instance, the high density and low diffusivity reduces the energy loss in pumping the fluid to the combustor.

Prior studies of supercritical mixing and combustion have mainly focused on rocket combustors *Yang* (2000); *Oefelein and Yang* (1998), where fuel is mixed with oxidizer prior to combustion. It has been observed that the high density ratio of the streams combined with the non-ideal thermodynamic relations lead to changes in mixing behavior. Near to the critical point, supercritical fluids surface tension and enthalpy of vaporization approach zero and specific heat increases exponentially along with density. All these phenomena pose an interesting problem for modeling because of the wildly different extremities in length and time scales that need to be resolved. In direct numerical simulation studies by Bellan and co-workers *Masi et al.* (2013); *Borghesi and Bellan* (2015), several anomalous features including uphill diffusion of species have been noted. These studies focused predominantly on temporal shear layers. One-dimensional studies by Oefelein et al.*Lacaze and Oefelein* (2012) have shown significant differences in flame structure at operating pressures close to critical point of the mixture.

The focus of this work is on supercritical CO_2 (s-CO_2) cycles for power generation with direct-fired high pressure combustors. According to McClung et al.*McClung et al.* (2014) , supercritical CO_2 gas turbine power generation cycles are able to reach cycle thermal efficiency target of 64% while cutting down on the turbine size and saving at least two heat exchangers because of the direct-firing of methane and oxygen into the supercritical CO_2 working fluid. In such cycles, oxy-combustion of fuel (typically methane or pulverized coal) heavily diluted with CO_2 ($> 95\%$ by mass) is used to provide the energy source. The operating pressures are expected to be around 200 bar or higher. Under such conditions, many different issues arise regarding the combustion process. Preliminary kinetics studies indicate that combustion processes will proceed rapidly at these conditions once mixing is complete. At the same time, presence of local hot spots can lead to device failure if these fluid pockets reach the combustor walls. Hence, the temperature rise inside the combustor is minimized by dilution with s-CO_2. As will be shown here, at such high dilution levels, the combustion process is rapid such that stable combustion is possible, but is also susceptible to strain-induced extinction. Hence, designing the mixing process is very critical.

In practical combustors, fuel-air mixing and flame structure are of vital importance. In particular, the effect of real gas law on jet evolution, mixing, and subsequent reaction processes needs to be understood in detail. Building on prior DNS studies, the focus here is on two engine-relevant configurations: 1) A coflowing supercritical jet and, 2) an annular configuration with a central fuel jet, an annular oxygen/s-CO_2 stream and an outer s-CO_2 stream. The objective is to determine the turbulence and mixing characteristics in such jets and to study the flame stabilization process.

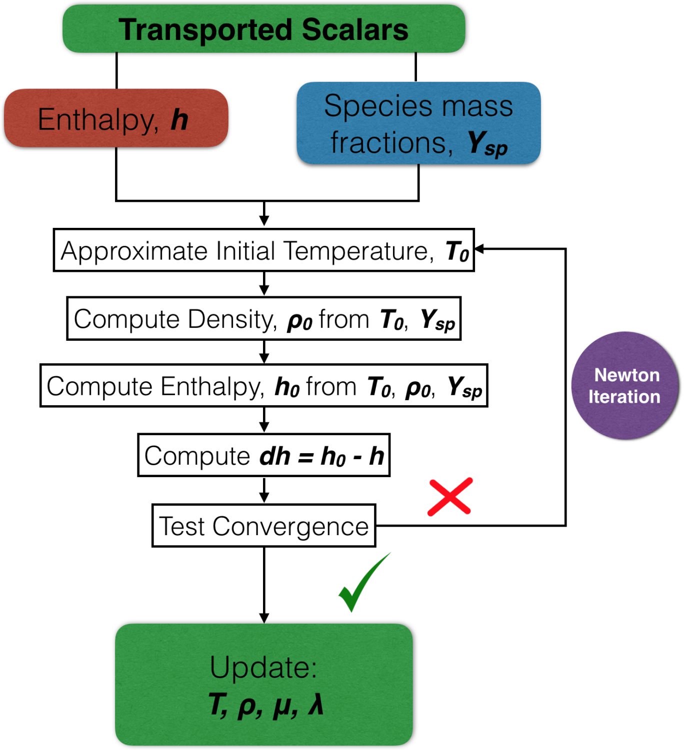

Figure A.1: Newton iteration algorithm to determine the thermodynamic properties given the transported scalars

A.1.1 Computational formulation for supercritical combustion

A.1.1.1 Low-Mach number direct numerical simulation solver for supercritical flows

The flows considered here, as opposed to rocket combustion, involve very low velocities and are generally in the low-Mach number regime. Consequently, significant computational speed-up can be achieved by formulating the numerical approach to remove acoustic components of the flow. This is typically carried out by the Poisson-equation based pressure correction approach *Kim and Moin* (1985); *Desjardins et al.* (2008). Here, at each time-step, a Poisson equation is used to enforce mass continuity, which has the physical implication of adjusting the pressure field at infinite speed. In other words, the acoustic waves are assumed to be removed instantaneously from the domain, leading to the equilibrated velocity field at the next time-step. Low-Mach solvers have been widely used for simulating reacting flows *Lietz et al.* (2014a); *Moureau et al.* (2007); *Kempf et al.* (2006); *Mueller and Pitsch* (2012), including complex geometries such as model aircraft combustors *Koo et al.* (2017). Here, this low-Mach number solver is adapted for supercritical flows by incorporating the real gas thermodynamic properties.

These modifications were implemented in the NGA structured grid solver *Desjardins et al.* (2008). In the simplest implementation of a low-Mach number approach, transport equations for momentum and scalars are first solved to obtain an intermediate solution. A thermochemical density field is then obtained from this solution, which is then used to enforced continuity by adjusting the velocity field. This change to the velocity field is obtained by a Possion equation solution. The low-Mach number approach followed here is a variation of this basic scheme and is explained in detail elsewhere *Desjardins et al.* (2008); *Koo et al.* (2017). In many applications, a conserved or reactive scalar is used to map the gas phase density field. In other words, the density field is obtained directly from an external function.

Here, this approach is not useful for several reasons. Since the gas phase scalars are directly evolved, an *a priori* relation between scalars and density is not readily available. At the same time, since the real gas equation is more complex and would require at least a 5 dimensional table to populate all the parameters, it is not cost-effective to store such a table and perform interpolation at every step. Furthermore, a refined table to store the large density gradient close to the critical region is not computationally tractable. Finally, when the application spans a region in pressure-density space that is close to the critical point, small changes in temperature can lead to large changes in density as mentioned. Consequently, a direct density feedback can cause the solver to become unstable. This has been observed in other contexts previously, for instance when coupling density to momentum equations in transported probability density function (PDF) methods *Han et al.* (2016); *Lietz et al.* (2014a); *Jenny et al.* (2001). Here, to overcome these issues and to take into account the departure function in C_p value in the diffusion term, a sensible enthalpy equation is transported along with the other governing equations. At each time-step, the source term for enthalpy is computed from the chemistry mechanism via chemkin modules (described in Sec. A.2.0.1). The density field is then obtained by inverting the enthalpy relation to temperature, assuming constant thermodynamic pressure (which equivalent to the low-Mach assumption).

The low-Mach number formulation is based on the energy-conservative staggered position-time algorithm using a structured, conservative finite-difference scheme. *Desjardins et al.* (2008). Time advancement is implemented using the semi-implicit second-order Crank-Nicolson scheme while the scalar transport is using the 2nd order BQUICK (Bounded-QUICK) scheme *Herrmann et al.* (2006) to reduce oscillations at lower and upper bounds for critical scalars like species mass fractions used in this study.

The general enthalpy and species mass fraction scalar transport equation is described in the equation below.

$$\frac{d(\rho\phi)}{dt} + \nabla \cdot (\rho u \phi) = \nabla \cdot (\rho D \nabla \phi) + \rho\dot{\omega}, \tag{A.1}$$

where ρ is the density, u is the velocity vector, ϕ represents the scalar quantities, D is the scalar diffusion coefficient described by the ratio of the thermal conductivity and constant pressure heat capacity for the mixture, k/C_p, and $\dot{\omega}$ is the source term of the scalars from combustion. Scalar transport diffusivity and viscosity were calculated based on the Chung et al. method *Chung et al.* (1988) from the Chapman-Enskog theory as explained in section A.1.1.3. Mixing rules from the corresponding method were also used.

To compute the chemical source terms, the enthalpy and species mass fractions are computed from Chemkin 0-D modules based on initial species mass fraction, temperature, and time-step. Enthalpy change from Chemkin is then corrected with Eq.A.11 to account for non-ideal effects and departure functions from heat capacity. The updated sensible enthalpy value is then used to calculate the local temperature using Newton iteration method where a user-defined convergence threshold residual (1e-06) is specified. With the new temperature, the density in each cell can be backed out from the pressure, temperature and local species mass fractions using a form of Eq.A.2. The diagram in Fig.A.1 shows the relationship between the transported scalars, their source terms, and the iterative method used to compute temperature and density.

A.1.1.2 Real Gas Thermodynamic Properties

To incorporate real gas effects, the cubic Peng-Robinson equation of state (EOS) will be used in this study. This EOS takes into account the non-linearity between pressure and density at the supercritical and especially the transcritical region where density gradient with respect to changes in temperature is high. This EOS is robust, accurate, and numerically efficient to implement. The pressure-density-temperature relation can be expressed as:

$$P = \frac{R_{mol}T}{V_m - B_m} - \frac{A_m}{V_m^2 + 2V_mB_m - B_m^2}, \tag{A.2}$$

where R_{mol} is the universal molar gas constant and V_m the molar volume related to the density as

$$V_m = \frac{MW}{\rho}, \tag{A.3}$$

where MW is the molecular weight of the fluid. A_m and B_m are functions of the individual species properties as described below:

$$A_{ij} = \frac{0.457236\alpha_{ij} R_{mol}^2 {T_{c_{ij}}}^2}{P_{c_{ij}}}, \tag{A.4}$$

$$A_m = \sum_i \sum_j X_i X_j A_{ij} \tag{A.5}$$

$$B_i = \frac{0.0777961 R_{mol} T_c}{P_c}, \tag{A.6}$$

$$B_m = \sum_i X_i B_i \tag{A.7}$$

$$\alpha_{ij} = \left[1 + (0.37464 + 1.54226\omega_{ij} - 0.26992{\omega_{ij}}^2)(1 - \sqrt{\frac{T}{T_{c_{ij}}}}) \right]^2 . \tag{A.8}$$

$$\omega_{ij} = \frac{1}{2}(\omega_{ii} + \omega_{jj}) \tag{A.9}$$

In the above relations, the acentric factor ω is a measure of the non-sphericity of the molecules, with this factor being 0.040 for N_2 as an example. T_c and P_c are the critical temperature and pressures of the fluid, which are $126.19K$ and $3.40MPa$ for N_2 as an example. Mixing rules for the application of Peng-Robinson EOS is described in Congiunti et al. *Congiunti et al.* (2003) and Harstad et al. *Harstad et al.* (1997). Mixing rules for the other parameters in the equations above can be found in the next section.

In the low-Mach number solver, the effect of changes to the thermochemical state of the mixture affects the flow field predominantly through changes to the density field. In a practical algorithm, this density change at each time-step is supplied to the solver (based on a combustion or mixing model). This density change then adjusts the velocity field through a pressure-Poisson equation. Due to the large density changes associated with the supercritical-to-subcritical pressure changes, and heat release due to chemical reactions, a direct feedback of the density solver will lead to a divergence of the pressure-Poisson equation. Here, an alternative approach is formulated, based on prior experience with transported probability density function (PDF) approach for combustion modeling *Raman et al.* (2005); *Han et al.* (2016). In this formulation, a sensible enthalpy equation is transported in the low-Mach number solver, and the density change obtained from changes in enthalpy. In the continuous space-time limit, this approach is identical to the density feedback. However, for finite grids, the use of the transport equation is equivalent to a Lagrangian filter that smooths the density change spatially. The sensible enthalpy equation is given by:

$$\rho \frac{Dh}{Dt} = \frac{1}{RePr}\frac{k}{C_p}\nabla^2 h + S_h, \tag{A.10}$$

where S_h is the chemical source term related enthalpy change. This enthalpy is related to the EoS as folows:

$$h = G - T\left(\frac{dG}{dT}\right)_{p,X} = h^0 + pv - RT + K_1\left(A_m - T\frac{dA_m}{dT}\right), \tag{A.11}$$

where G is the Gibbs energy, h^0 denotes the low-pressure reference enthalpy that can be calculated from NASA thermodynamic data coefficients for each species, and K_1 and $\frac{dA_m}{dT}$ are described as

$$K_1 = \frac{1}{2\sqrt{2}B_m} ln \left(\frac{V_m + (1-\sqrt{2})B_m}{V_m + (1+\sqrt{2})B_m} \right), \tag{A.12}$$

and

$$\frac{dA_m}{dT} = \frac{0.457236R^2T_c^2}{P_c} \left(\frac{k^2}{T_c} - \frac{k(1+k)}{\sqrt{TT_c}} \right), \tag{A.13}$$

A.1.1.3 Real Gas Transport Properties

Viscosity, thermal conductivity and mixing rules were computed using the Chung et al. *Chung et al.* (1988) method which is based on the Chapman-Enskog theory. It is selected for its accuracy near the critical point and numerical tractability compared to other corresponding state theory-based methods. Readers are referred to Congiunti et al. *Congiunti et al.* (2003) and Chung et al. *Chung et al.* (1988) for the rigorous calculation of thermodynamic parameters specified in this section. For sake of brevity, only the main idea and equations for calculating viscosity and thermal conductivity are laid out in this section.

For supercritical fluid, the Chung et al. viscosity has a correction term, η^* to the low pressure viscosity term, η^0, and the complete formulation is given by: $[Pa \cdot s]$

$$\eta = \eta^*\eta^0 = 1.0 \times 10^{-7}\left(\frac{1}{G_2} + E_6 y + \frac{\Omega_v}{F_{Cm}\sqrt{T_m}^*}\eta^{**}\right)\left(\frac{40.785F_{Cm}\sqrt{M_m T}}{V_{C_m}^{\frac{2}{3}}\Omega_v}\right) \tag{A.14}$$

$$F_{Cm} = 1 - 0.2756\omega_m + 0.059035\mu_{rm}^4 + k_m \tag{A.15}$$

where M_m is the mixture molecular weight, T is the temperature, V_{C_m} is the mixture critical volume, Ω_v is the collision integral as a function of temperature, F_{C_m} is an empirical factor depending on mixture accentric factor, ω_m, dimensionless dipole moment, μ_{r_m}, and a correction factor for polar substances, k_m, as described in equation A.15. η^{**}, G_2 and E_6 are computed from Chung et al parameters described in Congiunti et al. *Congiunti et al.* (2003) as a function of ω_m, μ_{r_m}, and k_m. T_m and y are computed from equations below.

$$T_m = 1.2593 T_r \tag{A.16}$$

$$y = \frac{\rho_m V_{C_m}}{6} \tag{A.17}$$

where T_r is the reduced temperature and ρ_m is the molecular density.

Similarly, the thermal conductivity is computed using Chung et al. method as shown in Eq A.18 below.

$$\lambda = \frac{31.2\eta^0 \Psi}{M_m}(G_2^{*-1} + B_6 y) + qB_7 y^2 \sqrt{T_r} G_2{}^* \tag{A.18}$$

where η^0 is the low pressure viscosity term, Ψ, $G_2{}^*$, B_6 and B_7 are parameters calculated using the same procedure as in the viscosity calculations. q is defined as in Eq. A.19 below:

$$q = 3.586 \times 10^{-3} \frac{\sqrt{\frac{T_{C_m}}{M_m}}}{V_{C_m}{}^{\frac{2}{3}}} \tag{A.19}$$

where T_{C_m} is the mixture critical temperature.

In terms of mixing rules for calculating thermodynamic and transport properties for mixtures, the following mixing rule is used according to Reid et al. *Reid et al.* (1987). To determine the mixture critical temperature, T_{C_m} and volume, V_{C_m}:

$$T_{C_m} = \frac{1}{V_{C_m}{}^{\frac{1}{4}}} \sum_i \sum_j x_i x_j V_{C_{ij}}{}^{\frac{1}{4}} T_{C_{ij}} \tag{A.20}$$

$$V_{C_m} = \sum_i \sum_j x_i x_j V_{C_{ij}} \tag{A.21}$$

$$T_{C_{ij}} = \sqrt{T_{C_i} T_{C_j}} k_{ij} \tag{A.22}$$

$$V_{C_{ij}} = \frac{1}{8}({V_{C_i}}^{\frac{1}{3}} + {V_{C_j}}^{\frac{1}{3}})^3 \tag{A.23}$$

$$P_{C_{ij}} = Z_{c,ij} R_{mol} \frac{T_{C_{ij}}}{V_{C_{ij}}} \tag{A.24}$$

$$Z_{c,ij} = \frac{1}{2}(Z_{c,ii} + Z_{c,jj}) \tag{A.25}$$

where k_{ij} are empirically determined binary interaction parameters for each species pair in this study while $T_{C_{ij}}$, $V_{C_{ij}}$, and $P_{C_{ij}}$ are binary critical temperature, volume and pressure. $Z_{c,ij}$ is the binary compressibility factor with Z_c for each species i and j obtained empirically.

A.2 Numerical Method

Direct numerical simulations (DNS) of two cylindrical jet configurations were carried out: (1) Premixed coflow of oxidizer with CO_2 diluent, (2) Annular O_2 case with coflowing CO_2 diluent . Both cases are running at conditions and stoichiometry pertinent to a supercritical gas-turbine combustor inlet.

The simulations were run using an in-house code developed in the University of Michigan. Real-gas effects explained above were implemented into a low-Mach number code. The low-Mach number formulation is based on the energy-conservative staggered position-time algorithm using a structured, conservative finite-difference scheme. *Desjardins et al.* (2008). Time advancement is implemented using the semi-implicit second-order Crank-Nicolson scheme while the scalar transport is using the 2nd order BQUICK (Bounded-QUICK) scheme to reduce oscillations at lower and upper bounds for critical scalars like species mass fractions used in this study, as explained in the previous section. The real gas thermodynamic and transport properties explained in the previous section were implemented in the existing solver.

This DNS simulation transports a sensible-enthalpy scalar equation to incorporate non-ideal gas effects and as a transported scalar to invert the temperature. 5x species mass fraction scalars were transported in the reacting cases to accurately compute the mixture density. Scalar transport diffusivity and viscosity were calculated based on the Chung et al. method *Chung et al.* (1988) from the Chapman-Enskog theory as explained in the previous section. Mixing rules from the corresponding method were also used.

A.2.0.1 Chemistry model

This study uses multi-step chemistry combustion model where kinetic mechanism, thermodynamic, and transport parameters are adapted from CH_4-BFER Mechanism *Franzelli et al.* (2012). This mechanism is validated for the conditions in this study except for pressure that is validated only until 12 atm while the operating condition for a high efficiency supercritical gas-turbine combustor is at 200 atm. However, the mechanism is still useful for this study because according to Franzelli et al. *Franzelli et al.* (2012), at high starting temperatures (∼700K), large descrepancies occur only at the low pressures, leaving the pressure dependency coefficient at high pressure to be more accurate for high pressure conditions. The mechanism consists of two global reactions below and 5 species (CH_4, O_2, H_2O, CO, CO_2) with transport properties similar to that of GRI 3.0 mechanism.

$$CH_4 + 1.5O_2 => CO + 2H_2O \tag{A.26}$$

$$CO + 0.5O_2 <=> CO_2 \tag{A.27}$$

A.3 Results

This section is divided into two phases: 1) Numerical validation using existing experimental data to demonstrate the accuracy of the variable density solver to model supercritical regimes, 2) DNS modeling of a supercritical (i) coflowing jet, and (ii) annular jet.

A.3.1 Coflow Jet Validation Study

The main validation study is based on the experimental configuration of Mayer et al. *Mayer et al.* (2003). This configuration injects supercritical nitrogen through a single, axisymmetric cylindrical injector into a chamber with quiescent, ambient temperature nitrogen gas. Table A.1 shows the flow conditions used for this validation study. This experimental condition permits investigation of pressure, temperature, and inflow velocity on the characteristics of the supercritical coflowing jet.

Figure A.2 shows the density contour plot with a large density change across the shear layer. Interestingly, the jet core penetrates nearly ten jet diameters before breaking down due to turbulence interactions. Note that jet penetration is highly dependent on the inflow turbulence levels. Even though the experiments do not provide detailed inflow measurements of velocity, the ability to predict jet penetration indicates that the use of a fully developed pipe flow profile at the inflow is reasonable for this configuration.

The centerline density profile (Figure A.3) and its decay rate is predicted well using the modified EOS and thermodynamic parameters. Dispersion of the supercritical jet at different axial distances from the inlet is very well predicted which points to a large part, an accurate specific heat prediction close to the critical point. As temperature decreases, specific heat, C_p increases exponentially and peaks close to the critical point*Congiunti et al.* (2003); *Yoo* (2013). The accurate location and magnitude of this C_p allows density dissipation to be predicted accurately i.e. denser flow with

Table A.1: Supercritical N_2 injection experimental target conditions for Case 4 in Mayer et al.*Mayer et al.* (2003)

P (MPa)	$U_{jet,builk}$ (m/s)	T_{jet} (K)	T_{co} (K)	D (mm)
4.0	5.0	130.0	298	2.2

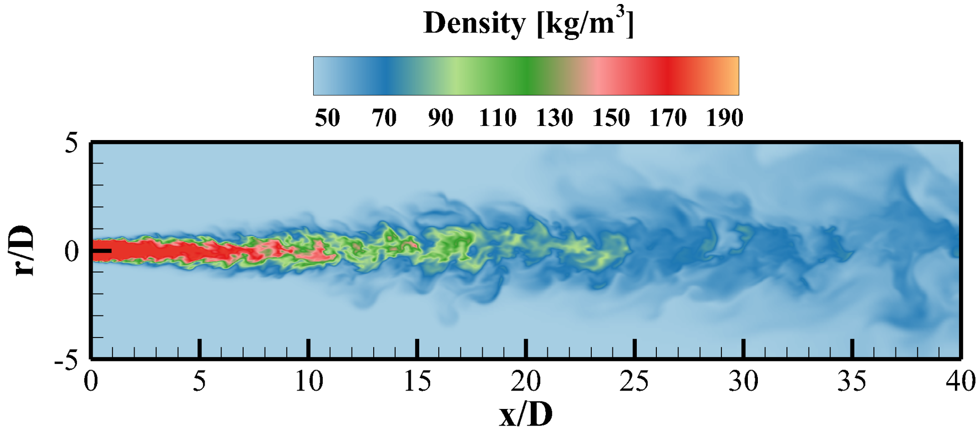

Figure A.2: N_2 Density; Target properties: 4 MPa, 5 m/s, 130 K

temperature close to the critical point will require more heat energy before density is dissipated, resulting in longer core density length and vice versa.

A.3.2 Coflow Reacting Jet

DNS study of a coflow reacting jet pertinent to realistic gas-turbine conditions is studied here. The flow field is characterized by a methane jet at ambient condition being injected into a coflowing supercritical mixture of CO2/O2. Details of the flow conditions are listed in Table A.2. The *Re* w.r.t. the fuel jet diameter is 4,000 with the smallest mesh size at $2.0 \times 10^{-5} m$ to resolve the Kolmogorov length scale. The domain contains 20 million grid points with axial and diameter size selected to be 80D × 20D with D = diameter of jet inlet. Such operating conditions are chosen based on conditions that are commonly encountered in a supercritical gas-turbine combustor with $\phi = 1.1$ and $T_{burnt} = T_{turbine} \sim 1600K$ *McClung et al.* (2014) .

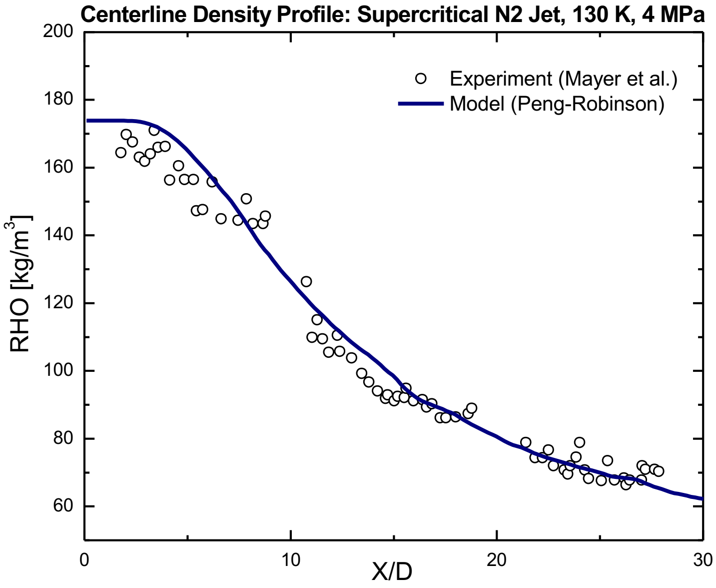

Figure A.3: Centerline N_2 Density: 4 MPa, 5 m/s, 130 K

The chemical reaction is solved using a 5-species 2-step mechanism as explained in section A.2.0.1. Note that the initial conditions here are in the supercritical region, not close to the critical point for any of the species considered. However, the application studied here, a gas-turbine combustor, require transcritical regime to be available as well for the mixture and for calculating departure from ideal gas thermodynamic properties as explained in section A.1.1.2.

From the instantaneous plots of temperature (Fig.A.4) and diffusivity (Fig.A.5), we can see that the jet flow is being enveloped by a thin flame-front that is attached close to the lip of the jet. This low maximum temperature flame ($T_{max} \sim 1490K$) is a result of supercritical CO_2 dilution. The high C_p value of the diluent and well premixed coflow with O_2 results in low temperature at the flame front that falls in between the thin-reaction zone and corrugated flamelet combustion regime. The region of high diffusivity in the downstream location, $X/D > 40$, is also caused by the higher temperature from the flame front and the well premixed coflow that encourages the flame front to react and propagate radially.

DNS data is then studied by comparing to 1-D laminar counterflow diffusion flame solutions obtained from FlameMaster *Pitsch* (1998) . The counterflow diffusion flame solution in mixture fraction space is a well-known topic *Peters* (1984), and details for solving the counterflow diffusion flame is omitted here for brevity. The 1-D diffusion flame calculation is done without using supercritical models for thermodynamic properties, and all thermodynamic properties are obtained using NASA polynomials. *Burcat* (1984) This is to compare the calculations from the original FlameMaster modules to DNS data and to determine if the flamelet method is a good representation of supercritical combustion.

A general layout showing temperature in mixture fraction space is shown in Fig.A.6, where a scatter plot DNS data is overlayed with flamelet solutions colored by the scalar dissipation rate, χ. To distinguish the DNS data from the flamelet results, a different color map is used for the DNS scatter, and scatters are only plotted 1 for each 100 cell index for visualization purposes. The definition of Z_{mix} here is the Bilger mixture fraction *Bilger et al.* (1990). It can be seen from Fig.A.6 that not only does most of the DNS data fall into the regime covered by the flamelet solutions, but also the DNS scatter has shown a certain preference of concentration in $T - Z_{mix}$ space. In the region close to the oxidizer side (Z_{mix}=0), the distribution of DNS scatters are not fully resolved in the plot, however for plot on the fuel size, there can be found a very clear transition of the DNS scatter from the upper branch to the middle branch at around $Z_{mix} = 0.2$, and finally switched to the extinction branch after Z_{mix} goes to 1, indicated by the colored large scalar dissipation rate. Meanwhile unsteady or extinction branch at Z from Z_{st} to 0.2 is rarely encountered in DNS, nor is the flammable solution at where $Z > 0.4$. Such preference is also displayed by the conditional averaged plot on the r.h.s. of Fig.A.6, where it can be seen a distributed temperature dependence on χ near the region $Z = 0.2$. In the region $0 < Z < 0.2$, all conditioned averaged temperature collapse toward the upper-branch value, and in

Table A.2: Operating conditions for reacting jet with annulus case

Inlet	U (m/s)	T (K)	D (mm)	P (MPa)	Species Mass frac (Y_i)
Jet	1.0	300	0.50	20	CH_4 (1.0)
Coflow	0.1854	1100	10.0	20	O_2(0.0457) + CO_2 (0.9543)

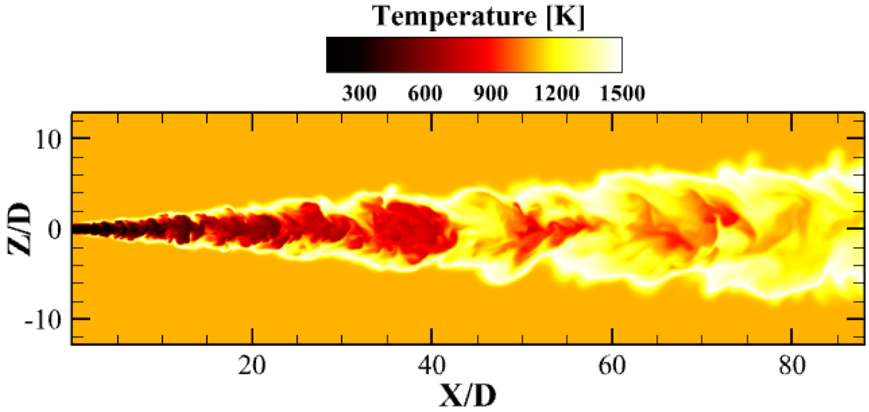

Figure A.4: Temperature instantaneous contour plot of reacting jet with CO_2 diluent

the region $Z > 0.2$, the conditional averaged temperature is converging towards the extinguished solution.

The supercritical coflow jet flame is further studied in terms of the species mass fractions, as shown in Fig.A.7, where Y_{CO} and Y_{H2O} are plotted against Z_{mix} colored by their chemical source term value. Previously, it was mentioned that on the oxidizer size, a lot of information are condensed in a small region of Z from 0 to Z_{st}, and therefore it is not easy to tell which branch are encountered more in the DNS study. Here in Fig.A.7, it is clearer from the CO mass fraction scatter to see that on the oxidizer side of the flame, the DNS covers a lower range of value for Y_{CO} than the flamelet solution, which indicates that the flame on the oxidizer side away from Z_{st} is also expected to show up on the unsteady branch. This can also be confirmed from the source term values indicated by the color, and notice that the range of colormap for the scatter is much smaller than that for the flamelet solutions in Fig.A.7. Therefore, a considerable portion of supercritical coflow jet flame is operating in the transition region between the upper and lower extinguished branch. Such phenomena is also

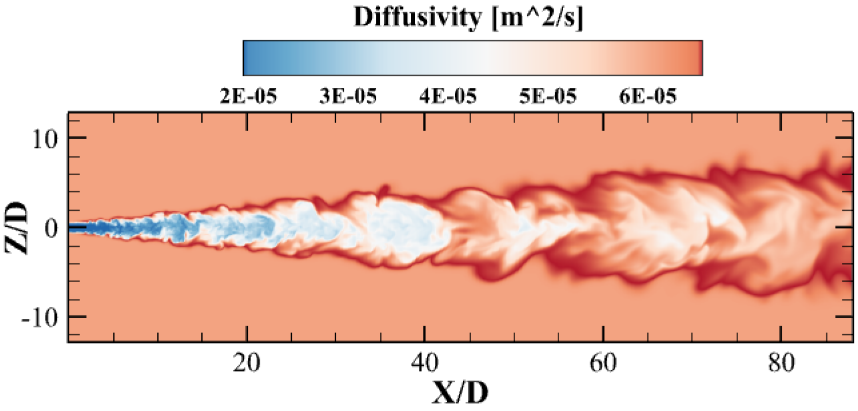

Figure A.5: Diffusivity instantaneous contour plot of reacting jet with CO_2 diluent

revealed by the H_2O mass fraction plot on r.h.s. of Fig.A.7, where it can be seen the scatters are mostly concentrated below the cluster of flamelet solutions that represent the upper branch. One of the reason behind this is due to the dilution of large amount of CO_2, which reduces the reaction rate, resulting in a combustion process that is very sensitive to the flow mixing and strain rate.

In Fig.A.8, heat production rate and CO_2 mass fraction are plotted against Z_{mix}. The peak of heat release is only achieved under very low scalar dissipation rate and is rarely encountered in the DNS data. The reason for DNS data not achieving the same peak value for heat release as flamelet may be due to strainrate effects. However, since the peak region is very narrowed down to near Z_{st}, the peak temperature from the DNS data still ends up being very close to the unstrained flamelet calculation. CO_2 is mainly acting as a diluent in the coflow, and therefore its distribution is mostly linear with relation to the mixture fraction, except for where close to Z_{st}.

Another interesting finding for the coflow jet is that when plotting the DNS averaged scalar dissipation rate in mixture fraction space, the peak is actually achieved near the value of $Z_{mix} = 0.8$, which is not typically seen from a counterflow diffusion flame configuration. In Fig.A.9, the χ for both DNS results and a theoretical solution for a strained 1-D counterflow diffusion flame with infinite fast chemistry are plot-

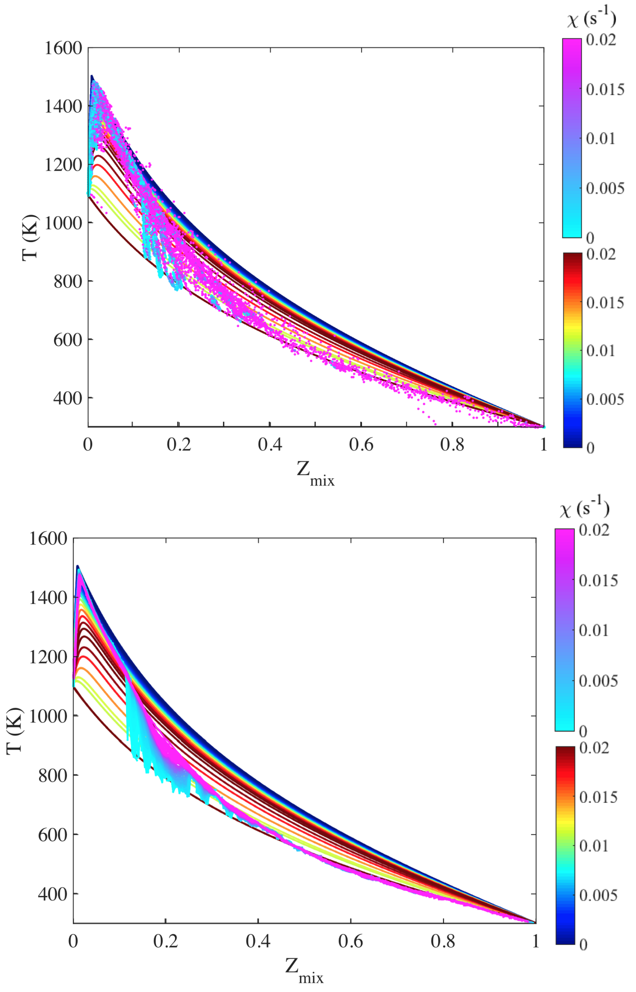

Figure A.6: Temperature-Zmix data in DNS overlayed with flamelet calculations, both DNS and flamelet data are colored by scalar dissipation rate, while using different colormaps. On l.h.s. the DNS data is plotted in terms of instantaneous scatter, and the r.h.s. in terms of conditional averaged valued based on χ

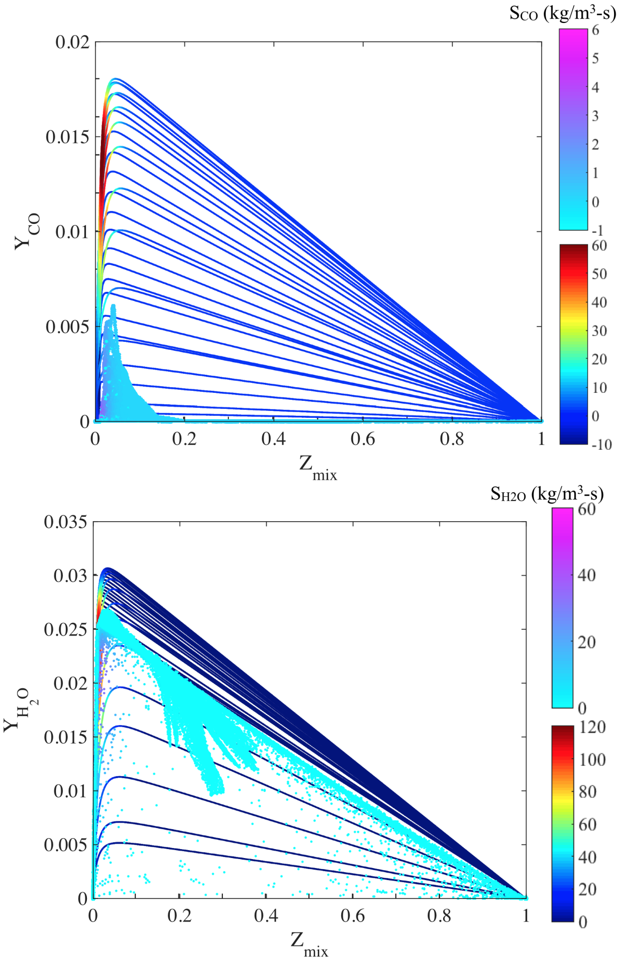

Figure A.7: Species mass fraction-Zmix DNS data scatter plot overlayed with flamelet calculations, both DNS scatter and flamelet curves are colored by the species' chemical source for mixture fraction Z, while using different colormaps.

ted in comparison, where it can be seen that the peak for the DNS data is shifted towards the fuel stream. As a brief explanation, the strained 1-D diffusion flame obtained from solving the mixture fraction equation in 1-D similarity coordinate space assuming infinite fast chemistry and constant density, and the solution profile is the well-known error function relation between χ and Z_{mix} in Eq.A.28.

$$\chi = \frac{a}{\pi} exp\left(-2\left[erf^{-1}\left(1-2Z_{mix}\right)^2\right]\right), \tag{A.28}$$

where a is the global strain rate specified as a boundary condition, and in this case chosen to be $a = 20s^{-1}$ to match the DNS peak. The assumption of constant density is further modified using Eq.A.29

$$\chi = \frac{a}{\pi}\left(\frac{\rho^2 D}{\rho^2(Z_{mix}=0.5)D(Z_{mix}=0.5)}\right) exp\left(-2\left[erf^{-1}\left(1-2Z_{mix}\right)^2\right]\right), \tag{A.29}$$

where the term $\left(\frac{\rho^2 D}{\rho^2(Z_{mix}=0.5)D(Z_{mix}=0.5)}\right)$ is obtained from the flamelet solution solved in mixture fraction space using detailed chemistry. And it turns out the modified peak is only slightly shifted to the left of $Z = 0.5$, which is within expectation as $\rho^2 D = const$ is usually valid and assumed for diffusion flame analysis. Therefore, the cause of the shift of the DNS peak toward $Z = 1$ in this case can be very different from variable density effects, and remains to be seen.

A cause for concern to the operation of a turbine is the concentration of CO species entering the turbine from the combustor. Even a small mass fraction of CO can potentially react with coolant air at the tip of the turbine blade to produce CO_2 which will generate a large amount of heat release and thus reduce the material life-expectancy in the long-run. In this DNS case, the mass fraction of CO species is looked into and the instantaneous as well as time-averaged plots are shown in Fig.A.10. As shown, the mass fraction of CO is mostly concentrated at the flame front and at

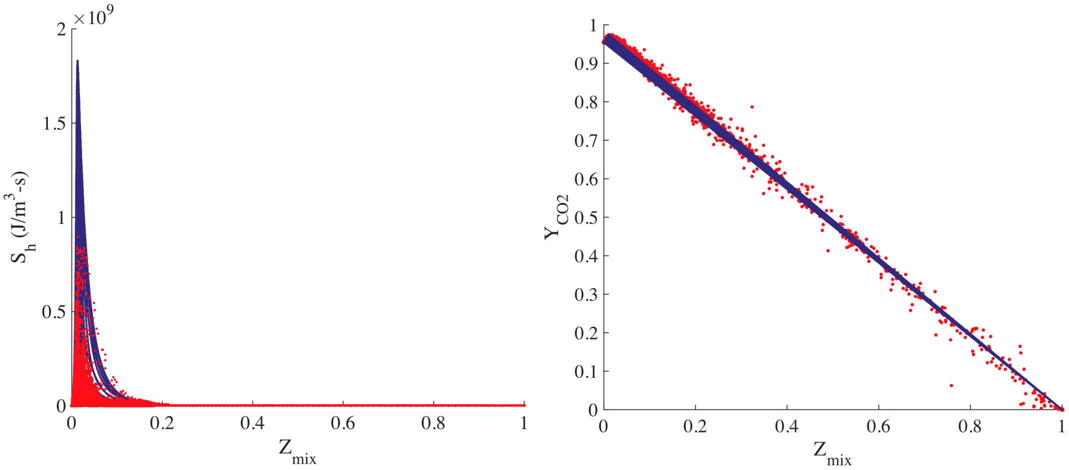

Figure A.8: Enthalpy source (left) and Y_{CO_2} (right) - Zmix DNS data scatter plot overlayed with flamelet calculations.

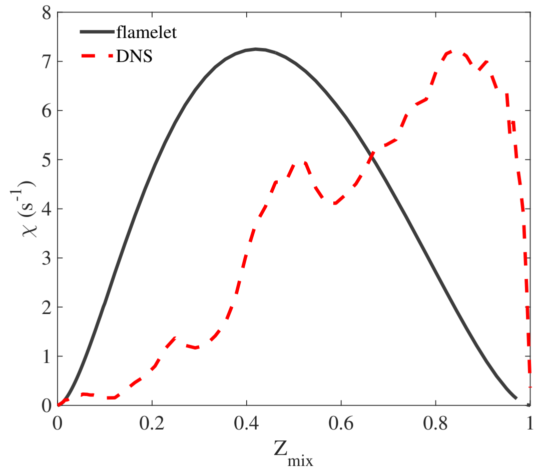

Figure A.9: Scalar disspation rate vs. Z_{mix}. Solid line represents a steady strained 1-D diffusion flame with infinitely fast chemistry, dash line obtained by averaging DNS data based on Z_{mix}

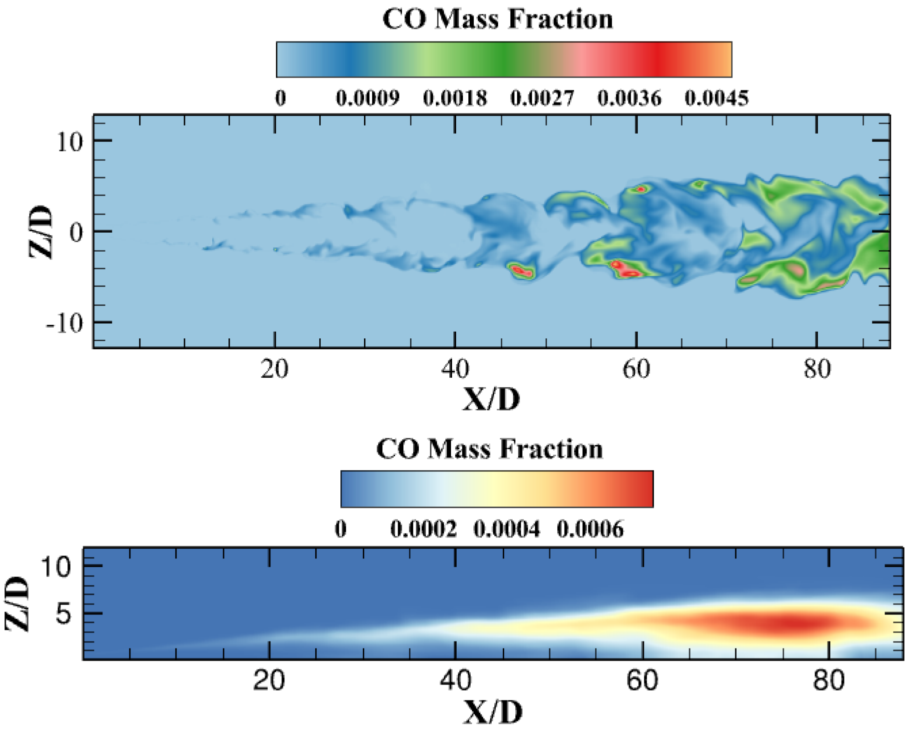

Figure A.10: CO mass fraction instantaneous and time-averaged plot of reacting jet with CO_2 diluent

pockets of fuel rich region as plotted in Fig.A.6. Time-averaged data also shows a moderately high concentration of CO at the downstream region $60 < X/D < 88$. Future design of supercritical direct-fired combustor will have to look into this factor when considering methods for decreasing CO mass fraction from the combustion process. Future work will also concentrate on testing the effect of different scalar dissipation rates and fuel injection methods to decrease the probability of fuel rich regions of high temperature igniting and producing CO.

A.3.3 Annular Reacting Jet

Another configuration that is important to realistic gas-turbine design conditions is a jet in crossflow. Here, oxygen and methane streams enter through seperate nozzles while s-CO_2 serves as the crossflow. In order to replicate the flame physics in this geometry, a simpler annular jet is considered here. Here a diluted O_2 + CO_2

Table A.3: Operating conditions for reacting jet with annulus case

Inlet	U (m/s)	T (K)	D (mm)	P (MPa)	Species Mass frac (Y_i)
Jet	1.0	300	0.50	20	CH_4 (1.0)
Annulus	5.061	1100	1.50	20	O_2(0.1538) + CO_2 (0.8462)
Coflow	0.1854	1100	10.0	20	CO_2 (1.0)

stream flows in parallel to the fuel jet, with a coflow of supercritical CO_2 enveloping the domain. Same general configuration and global stoichiometry are chosen for this case, compared to the coflowing jet case, corresponding to $Re = 4{,}000$ with 20 million grid points and similar mesh configuration as shown in Table A.3.

The aim of this case is to understand the combustion process of a different configuration to the coflowing jet. As expected of an annular case with high annulus velocity compared to the jet velocity, the combustion is highly mixing-controlled and depends on the flow turbulence at the downstream location from the inlet. From Fig.A.11 below, combustion is shown to happen at the $X/D = 20$ location downstream of the inlet, where the flame is lifted and not attached to the lip like in the jet coflow case. This will prevent any damage to the inlet wall but causes difficulties in controlling the flame because of the strong diffusion and strain-rate based flame ignition. Another disadvantage of the annular case is the high maximum temperature ($\sim 1900K$) of the flame compared to the jet case ($\sim 1500K$) which could propagate and result in high local temperature that could damage the turbine blades and result in lowered turbine efficiency.

As there are three different streams in the system of the annular jet case, an additional mixture fraction is introduced, and distinguished using subscript number. Here Z_1 indicates the proportion of mass flow originating from the jet stream, and Z_2 is assigned for the annular jet. Rigorously, there is also a Z_3 for the coflow, however by definition it automatically follows the relation $Z_3 = 1-(Z_1 + Z_2)$, and the domain of mixture fraction space on the $Z_1 - Z_2$ plane should be a unit triangle. An example

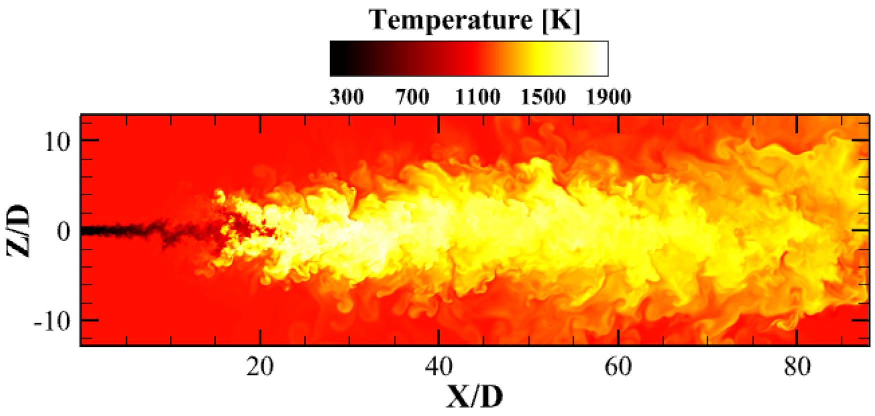

Figure A.11: Temperature instantaneous contour plot of reacting jet with annular and CO_2 diluent

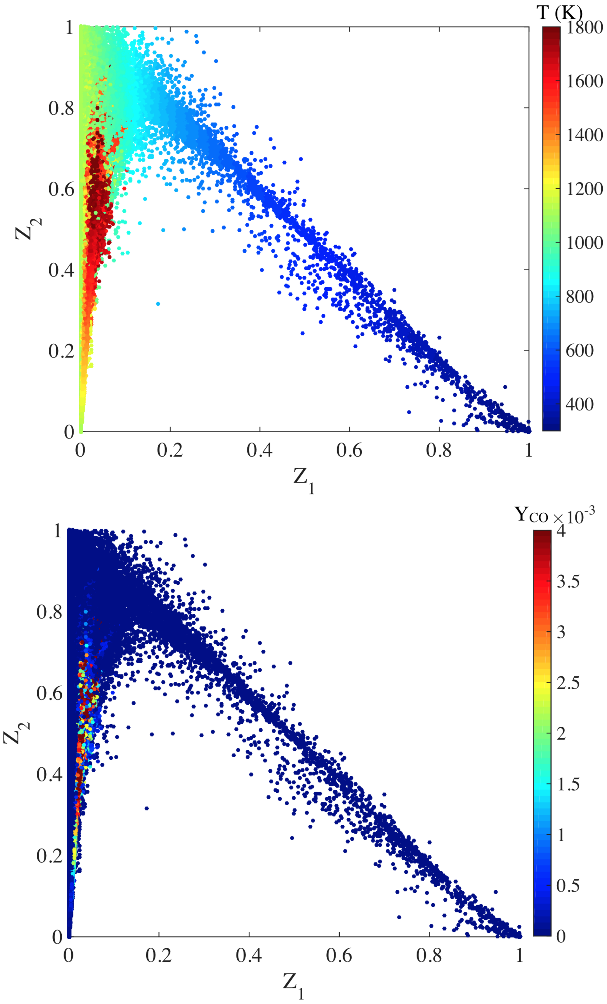

Figure A.12: Instantaneous scatter plot of DNS computational domain in $Z_1 - Z_2$ space, colored by temperature (left) and CO mass fraction (right) of the transformation into the two mixture fraction space can be seen in Fig.A.12, where the DNS data of the original computational domain is plotted in scatter and colored by an extra property in mixture fraction space.

In Fig.A.12 it can be seen that the direction of the most obvious temperature variation is in Z_1, which is because Z_1 indicates the mixing between the fuel jet and the rest of the mixture, plus that the jet stream has the lowest temperature of 300K comparing the rest of the other two. A high concentration of high temperature is achieved in the region of of $Z_1 \sim 0.05$ and $Z_2 \sim 0.6$, and the peak value of temperature 1800K is higher than the previous coflow case of 1500K, which is because the fuel stream is now able to access a higher concentration of oxidizer from the annular jet. The influence of Z_2 comes into place mostly when Z_1 decreases to around 0.1, by changing the proportion of mixture provided for the reaction. For $Z_1 > 0.2$ and $Z_2 > 0.8$, the variation of temperature is mainly driven by mixing. Another distinguishable observation from Fig.A.12 is the triangle-shaped region that is rarely encountered by the DNS data, which shows a pattern of how Z_1 and Z_2 is linearly correlated in the DNS case. As an explanation, such pattern should be governed by the inner and outer mixing layer of the annular jet, where the inner mixing layer should correspond to the left "edge" of the "triangle", and the outer mixing layer the right "edge".

Comparing CO species mass fractions with the jet case, the magnitude of CO mass fraction produced is an order of magnitude higher than the jet case. Furthermore, the location of peak CO mass fraction for both cases are also different with the annular case experiencing a higher CO mass fraction close to the axis at $X/D = 40$. This is predominantly due to the inhomogeneous mixing between the fuel and oxidizer resulting in local regions corresponding to $Z_1 < 0.05$ and $Z_2 \sim 0.6$ on the r.h.s. plot in Fig.A.12. This region where there is less dilution from CO_2 has a high temperature due to the lowered mixture C_p values. The local fuel rich condition in the central axis

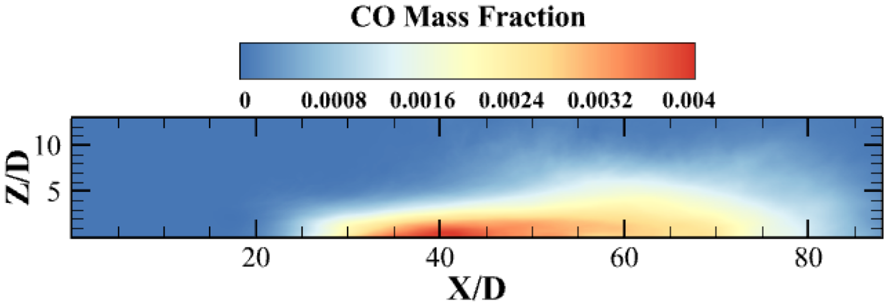

Figure A.13: CO species time-averaged mass fraction contour plot of reacting jet with annular and CO_2 diluent

is due to the enveloping effect of the annular O_2 jets preventing the central fuel jet from diffusing radially downstream. This high strain rate region produces incomplete combustion between the fuel and oxidizer, which produces a high concentration of CO species.

A.4 Conclusions

In this study, two possible configurations of supercritical combustion in a gas-turbine combustor are being simulated and analyzed - (1) jet with coflow, and (2) jet with annular. We also implemented real gas cubic equations and departure functions for thermodynamic and transport properties to a low-Mach solver. Detailed representation of the algorithm and Newton iteration to arrive at the final mixture temperature and density from transported enthalpy and species mass fractions is in Fig. A.1. For reacting DNS simulations, a two-step chemistry approach is being implemented for $CH_4 + O_2$ combustion with CO_2 as diluent. A lower peak temperature is being predicted due to the high concentration of dilution from CO_2, a high C_p species. This work also illustrates the capability of this in-house code to investigate a non-reacting validation case by Mayer et al.*Mayer et al.* (2003) where N_2 mixing in a quiescent chamber close to the critical point compares favorably with the experimental results. The simulation result shows accurate diffusivity calculations from comparisons to the centerline density.

From analysis of the DNS data for both reacting cases, a clear distinction between the configuration at supercritical conditions is seen. A simple fuel jet with premixed (oxidizer+diluent) coflow case shows an attached flame at the lip of the fuel jet inlet with low maximum flame temperature mainly due to the high rate of dilution by CO_2. This condition is advantageous to the operating condition of a direct-fired supercritical combustor where fuel and oxidizer is being injected into a supercritical flow to heat up the working fluid because the maximum possible temperature for optimum efficiency of the turbine expansion phase is $\sim 1500K$. Furthermore, formation of CO in the jet configuration is at the flame front further downstream of the jet inlet and shows a low amount of CO being produced, indicating a close to complete combustion process in this configuration.

For the jet with annular case, the approximately 85% CO_2 and 15% O_2 (by mass) annular jet produces a highly turbulent region downstream at $X/D = 20$, producing a highly lifted flame with high flame temperatures approaching 1900K. Moreover, an order of magnitude higher CO mass fractions is also observed in the annular case compared to the jet case mainly due to the high temperature at the central axis region increasing the reaction rate of CO formation. Fuel rich conditions at the central mixing zone due to inhomogeneous mixing also decreases the rate of CO being turned into CO_2, thus forming an accumulation of CO species at the central region. This combination of higher maximum temperature and higher CO mass fraction will inevitably lead to unfavorable conditions for the operation of the turbine where CO species will react with dilution air at the tip of the turbine blade to complete the combustion process and produce large amounts of heat release that will decrease the life-cycle expectancy of the turbine blades.

In the future, the authors plan to conduct more studies into a different configuration that is still pertinent to normal combustor operations to determine if these conditions are conducive to a supercritical environment. An example of such configuration is the Jet-In-Crossflow configuration where high strain rate crossjet mixing is expected to enhance the combustion process that could further reduce CO species production perhaps to a level even lower than that of the jet case studied here. Furthermore, the DNS data obtained here can be a good yardstick for future development of algorithms and combustion models for the supercritical regime. This work also pushes for more simulation work on transcritical combustion where large density gradient with small temperature gradient is especially important in the mixing region prior to combustion.

BIBLIOGRAPHY

BIBLIOGRAPHY

(2011), Chemical-Kinetic Mechanisms for Combustion Applications, San Diego Mechanism web page, Mechanical and Aerospace Engineering (Combustion Research), University of California at San Diego (http://combustion.ucsd.edu).

(2016), International sooting flame workshop 3, https://www.adelaide.edu.au/cet/isfworkshop.

(2017), The open source cfd toolbox, openCFD Inc. http://www.openfoam.com.

Attili, A., F. Bisetti, M. E. Mueller, and H. Pitsch (2014), Formation, growth, and transport of soot in a three-dimensional turbulent non-premixed jet flame, *Combust. Flame*, *171*(7), 1849–1865.

Balthasar, M., and M. Kraft (2003), A stochastic approach to calculate the particle size distribution function of soot particles in laminar premixed flames, *Combustion and Flame*, *133*(3), 289–298.

Bilger, R., S. Stårner, and R. Kee (1990), On reduced mechanisms for methane air combustion in nonpremixed flames, *Combustion and Flame*, *80*(2), 135–149.

Bisetti, F., G. Blanquart, M. E. Mueller, and H. Pitsch (2012), On the formation and early evolution of soot in turbulent nonpremixed flames, *Combust. Flame*, *159*(1), 317–335.

Blanquart, G., and H. Pitsch (2009a), Analyzing the effects of temperature on soot formation with a joint volume-surface-hydrogen model, *Combust. Flame*, *156*(8), 1614–1626.

Blanquart, G., and H. Pitsch (2009b), A joint volume-surface-hydrogen multi-variate model for soot formation, *Combustion Generated Fine Carbonaceous Particles*, pp. 437–463.

Blanquart, G., P. Pepiot-Desjardins, and H. Pitsch (2009), Chemical mechanism for high temperature combustion of engine relevant fuels with emphasis on soot precursors, *Combust. Flame*, *156*(3), 588–607.

Borghesi, G., and J. Bellan (2015), Irreversible entropy production rate in high-pressure turbulent reactive flows, *Proceedings of the Combustion Institute*, *35*(2), 1537–1547.

Burcat, A. (1984), *Thermochemical Data for Combustion Calculations*, pp. 455–473, Springer US, New York, NY.

Celnik, M., R. Patterson, M. Kraft, and W. Wagner (2007), Coupling a stochastic soot population balance to gas-phase chemistry using operator splitting, *Combustion and Flame*, *148*(3), 158–176.

Chapuis, M., E. Fedina, C. Fureby, K. Hannemann, S. Karl, and J. M. Schramm (2013), A computational study of the HyShot II combustor performance, *Proc. Combust. Inst.*, *34*, 2101–2109.

Charest, M. R., C. P. Groth, and Ö. L. Gülder (2011a), A numerical study on the effects of pressure and gravity in laminar ethylene diffusion flames, *Combust. Flame*, *158*(10), 1933–1945.

Charest, M. R. J., H. I. Joo, Ö. L. Gülder, and C. P. T. Groth (2011b), Experimental and numerical study of soot formation in laminar ethylene diffusion flames at elevated pressures from 10 to 35 atm, *Proc. Combust. Inst.*, *33*(1), 549–557.

Chen, J.-Y. (1997), Stochastic modeling of partially stirred reactors, *Combust. Sci. Technol.*, *122*(1-6), 63–94.

Chong, S. T., Y. Tang, M. Hassanaly, and V. Raman (2017), Turbulent mixing and combustion of supercritical jets, in *55th AIAA Aerospace Sciences Meeting*, p. 0141.

Chong, S. T., M. Hassanaly, H. Koo, M. E. Mueller, V. Raman, and K.-P. Geigle (2018a), Large eddy simulation of pressure and dilution-jet effects on soot formation in a model aircraft swirl combustor, *Combust. Flame*, *192*, 452–472.

Chong, S. T., V. Raman, M. E. Mueller, and H. G. Im (2018b), The role of recirculation zones in soot formation in aircraft combustors, in *ASME Turbo Expo 2018*, GT2018-76217.

Chong, S. T., V. Raman, M. E. Mueller, P. Selvaraj, and H. G. Im (2018c), Effect of soot model, moment method, and chemical kinetics on soot formation in a model aircraft combustor, *Proceedings of the Combustion Institute*.

Chung, T. H., M. Ajlan, L. L. Lee, and K. E. Starling (1988), Generalized multiparameter correlation for nonpolar and polar fluid transport properties, *Industrial & Engineering Chemistry Research*, *27*, 671–679.

Congiunti, A., C. Bruno, and E. Giacomazzi (2003), Supercritical Combustion Properties, *AIAA Aerospace Sciences Meeting and Exhibit*, *41*(January), 1–20.

Correa, S. M. (1993), Turbulence-chemistry interactions in the intermediate regime of premixed combustion, *Combust. Flame*, *93*(1-2), 41–60.

Deng, S., M. E. Mueller, Q. N. Chan, N. H. Qamar, B. B. Dally, Z. T. Alwahabi, and G. J. Nathan (2017), Hydrodynamic and chemical effects of hydrogen addition on soot evolution in turbulent nonpremixed bluff body ethylene flames, *Proc. Combust. Inst.*, *36*(1), 807–814.

Desjardins, O., G. Blanquart, G. Balarac, and H. Pitsch (2008), High order conservative finite difference scheme for variable density low Mach number turbulent flows, *Journal of Computational Physics*, *227*, 7125–7159.

Dobbins, R., R. A. Fletcher, and H.-C. Chang (1998), The evolution of soot precursor particles in a diffusion flame, *Combustion and flame*, *115*(3), 285–298.

Donaldson, K., L. Tran, L. A. Jimenez, R. Duffin, D. E. Newby, N. Mills, W. MacNee, and V. Stone (2005), Combustion-derived nanoparticles: a review of their toxicology following inhalation exposure, *Particle and fibre toxicology*, *2*(1), 10.

Donde, P., V. Raman, M. E. Mueller, and H. Pitsch (2013), LES/PDF based modeling of soot-turbulence interactions in turbulent flames, *Proc. Combust. Inst.*, *34*, 1183–1192.

Dopazo, C. (1975), Probability density function approach for a turbulent axisymmetric heated jet. centerline evolution, *Phys. Fluids*, *18*(4), 397–404.

Dopazo, C., and E. E. O'Brien (1974), An approach to the autoignition of a turbulent mixture, *Acta Astronautica*, *1*, 1239–1266.

Eberle, C., P. Gerlinger, K. P. Geigle, and M. Aigner (2014), Soot predictions in an aero-engine model combustor at elevated pressure using URANS and finite-rate chemistry, in *50th AIAA/ASME/SAE/ASEE Joint Propulsion Conference*, AIAA 2014-3472.

Eberle, C., P. Gerlinger, K. P. Geigle, and M. Aigner (2015), Numerical investigation of transient soot evolution processes in an aero-engine model combustor, *Combust. Sci. Technol.*, *187*(12), 1841–1866.

El-Asrag, H., and S. Menon (2009), Large eddy simulation of soot formation in a turbulent non-premixed jet flame, *Combust. Flame*, *156*(2), 385–395.

Ferziger, J. H., and M. Peric (2002), *Computational Methods for Fluid Dynamics*, 3rd ed., Springer.

Franzelli, B., E. Riber, L. Y. M. Gicquel, and T. Poinsot (2012), Large Eddy Simulation of combustion instabilities in a lean partially premixed swirled flame, *Combustion and Flame*, *159*(2), 621–637.

Frenklach, M. (2002), Method of moments with interpolative closure, *Chem. Eng. Sci.*, *57*(12), 2229–2239.

Frenklach, M., and S. Harrris (1986), Aerosol dynamics modeling using the method of moments, *J. Colloid and Interface Sci.*, *118*(1), 252–262.

Frenklach, M., and H. Wang (1991a), Detailed modeling of soot particle nucleation and growth, in *Symposium (International) on Combustion*, vol. 23, pp. 1559–1566, Elsevier.

Frenklach, M., and H. Wang (1991b), Detailed modeling of soot particle nucleation and growth, *Symp. (Int.) Combust.*, *23*, 1559–1566.

Friedlander, S. K. (2000), Smoke, Dust, and Haze: Fundamentals of Aerosol Dynamics, *Oxford University Press, New York*.

Geigle, K. P., R. Hadef, and W. Meier (2014), Soot formation and flame characterization of an aero-engine model combustor burning ethylene at elevated pressure, *J. Eng. Gas Turbines and Power*, *136*, 021,505–021,505–7.

Geigle, K. P., M. Köhler, W. OLoughlin, and W. Meier (2015), Investigation of soot formation in pressurized swirl flames by laser measurements of temperature, flame structures and soot concentrations, *Proc. Combust. Inst.*, *35*(3), 3373–3380.

Geigle, K. P., R. Hadef, M. Stöhr, and W. Meier (2017), Flow field characterization of pressurized sooting swirl flames and relation to soot distributions, *Proc. Combust. Inst.*, *36*(3), 3917–3924.

Gelbard, F., and J. H. Seinfeld (1980), Simulation of multicomponent aerosol dynamics, *Journal of colloid and Interface Science*, *78*(2), 485–501.

Germano, M., U. Piomelli, P. Moin, and W. H. Cabot (1991), A dynamic subgrid-scale eddy viscosity model, *Physics of Fluids*, *7*, 1760–1765.

Hall, R., M. Smooke, and M. Colket (1997), Predictions of soot dynamics in opposed jet diffusion flames, *Physical and Chemical Aspects of Combustion: A Tribute to Irvin Glassman*, *4*, 189–229.

Ham, F., S. Apte, G. Iaccarino, X. Wu, M. Herrmann, G. Constantinescu, K. Mahesh, and P. Moin (2003), Unstructured les of reacting multiphase flows in realistics gas turbine combustors, in *CTR Annual Research Briefs*, pp. 139–160, Center for Turbulence Research, CTR, Stanford University.

Han, W., V. Raman, and Z. Chen (2016), LES/PDF modeling of autoignition in a lifted turbulent flame: Analysis of flame sensitivity to differential diffusion and scalar mixing time-scale, *Combustion and Flame*, *171*, 69–86.

Harris, S. J., and I. M. Kennedy (1988), The coagulation of soot particles with van der waals forces, *Combustion science and technology*, *59*(4-6), 443–454.

Harris, S. J., and A. M. Weiner (1983), Surface growth of soot particles in premixed ethylene/air flames, *Combustion Science and Technology*, *31*(3-4), 155–167.

Harstad, K. G., R. S. Miller, and J. Bellan (1997), Efficient high-pressure state equations, *AIChE Journal*, *43*(6), 1605–1610.

Hassanaly, M., H. Koo, C. F. Lietz, S. T. Chong, and V. Raman (2018), A minimally-dissipative low-mach number solver for complex reacting flows in openfoam, *Computer and Fluids*, *162*, 11–25.

Herrmann, M., G. Blanquart, and V. Raman (2006), Flux Corrected Finite Volume Scheme for Preserving Scalar Boundedness in Reacting Large-Eddy Simulations, *AIAA Journal*, *44*(12), 2879–2886.

Heye, C., C. M. Kaul, and V. Raman (2011), Analysis of scalar variance modeling for large eddy simulation of combustion using explicit filtering, in *Proceedings of Turbulence and Shear Flow Phenomena Conferences 2011*.

Ihme, M., and H. Pitsch (2008), Modeling of radiation and nitric oxide formation in turbulent nonpremixed flames using a flamelet/progress variable formulation, *Physics of Fluids*, *20*(5), doi:DOI 10.1063/1.2911047.

Issa, R. I. (1985), Solution of the implicitly discretised fluid flow equations by operator-splitting, *Journal of Computational Physics*, *62*, 40–65.

Janicka, J., W. Kolbe, and W. Kollmann (1979), Closure of the transport equation for the probability density funcfion of turbulent scalar fields, *Journal of Non-Equilibrium Thermodynamics*, *4*(1), 47–66.

Jenny, P., S. Pope, M. Muradoglu, and D. Caughey (2001), A Hybrid Algorithm for the Joint PDF Equation of Turbulent Reactive Flows, *Journal of Computational Physics*, *166*(2), 218–252.

Kailasanathan, R. K. A., E. K. Book, T. Fang, and W. L. Roberts (2013), Hydrocarbon species concentrations in nitrogen diluted ethylene-air laminar jet diffusion flames at elevated pressures, *Proc. Combust. Inst.*, *34*(1), 1035–1043.

Karatas, A. E., and Ö. L. Gülder (2012), Soot formation in high pressure laminar diffusion flames, *Prog. Energ. Combust. Sci.*, *38*(2), 818–845.

Katta, V. R., T. R. Meyer, C. Montgomery, and W. M. Roquemore (2005), Studies on soot formation in a model gas-turbine combustor, in *41th AIAA/ASME/SAE/ASEE Joint Propulsion Conference and Exhibit*, 2005-3777.

Kaul, C. M., and V. Raman (2011), A posteriori analysis of numerical errors in subfilter scalar variance modeling for large eddy simulation, *Physics of Fluids*, *23*(3).

Kaul, C. M., V. Raman, G. Balarac, and H. Pitsch (2009), Numerical errors in the computation of subfilter scalar variance in large eddy simulations, *Phys. Fluids*, *21*(5), 055,102.

Kazakov, A., and M. Frenklach (1998), Dynamic modeling of soot particle coagulation and aggregation: Implementation with the method of moments and application to high-pressure laminar premixed flames, *Combustion and Flame*, *114*(3-4), 484–501.

Kazakov, A., H. Wang, and M. Frenklach (1995), Detailed modeling of soot formation in laminar premixed ethylene flames at a pressure of 10 bar, *Combustion and Flame*, *100*(1-2), 111–120.

Kempf, A., R. P. Lindstedt, and J. Janicka (2006), Large-eddy simulation of bluff-body stabilized nonpremixed flame, *Combust. Flame*, *144*(1-2), 170–189.

Kim, J., and P. Moin (1985), Application of a fractional-step method to incompressible Navier-Stokes equations, *Journal of Computational Physics*, *59*(2), 308–323.

Kim, J., P. Moin, and R. D. Moser (1987), Turbulence statistics in fully developed channel flow at low Reynolds number, *Journal of Fluid Mechanics*, *177*, 133–166.

Koo, H., V. Raman, M. E. Mueller, and K. P. Geigle (2015), Large-eddy simulation of a turbulent sooting flame in a swirling combustor, in *53rd AIAA Aerospace Sciences Meeting*, p. 0167.

Koo, H., M. Hassanaly, V. Raman, M. E. Mueller, and K. P. Geigle (2016a), Large-eddy simulation of soot formation in a model gas turbine combustor, in *ASME Turbo Expo 2016*, GT2016-57952.

Koo, H., V. Raman, M. E. Mueller, and K.-P. Geigle (2016b), LES of a sooting flame in a pressurized swirl combustor, in *54th AIAA Aerospace Sciences Meeting*, p. 2123.

Koo, H., M. Hassanaly, V. Raman, M. E. Mueller, and K. P. Geigle (2017), Large-eddy simulation of soot formation in a model gas turbine combustor, *J. Eng. Gas Turbines and Power*, *139*(3), 031,503.

Lacaze, G., and J. C. Oefelein (2012), A non-premixed combustion model based on flame structure analysis at supercritical pressures, *Combustion and Flame*, *159*(6), 2087–2103.

Leung, K. M., R. P. Lindstedt, and W. Jones (1991), A simplified reaction mechanism for soot formation in nonpremixed flames, *Combust. Flame*, *87*(3-4), 289–305.

Lietz, C., and V. Raman (2015), Large eddy simulation of flame flashback in swirling premixed CH_4/H_2-air flames, in *53rd AIAA Aerospace Science Meeting*, AIAA 2015-0844.

Lietz, C., M. Hassanaly, V. Raman, H. Kolla, J. Chen, and A. Gruber (2014a), LES of Premixed Flame Flashback in a Turbulent Channel, *52nd Aerospace Sciences Meeting*, (January), 1–11.

Lietz, C., C. Heye, V. Raman, and D. Blunck (2014b), Flame stability analysis in an ultra compact combustor using large-eddy simulation, in *52nd AIAA Aerospace Science Meeting*, AIAA 2014-1022.

Lighty, J. S., J. M. Veranth, and A. F. Sarofim (2000), Combustion aerosols: factors governing their size and composition and implications to human health, *Journal of the Air & Waste Management Association*, *50*(9), 1565–1618.

Lignell, D. O., J. H. Chen, P. J. Smith, T. Lu, and C. K. Law (2007), The effect of flame structure on soot formation and transport in turbulent nonpremixed flames using direct numerical simulation, *Combustion and Flame*, *151*(1-2), 2–28.

Lignell, D. O., J. H. Chen, and P. J. Smith (2008), Three-dimensional direct numerical simulation of soot formation and transport in a temporally evolving nonpremixed ethylene jet flame, *Combustion and flame*, *155*(1-2), 316–333.

Lindstedt, R., and S. Louloudi (2005), Joint-scalar transported pdf modeling of soot formation and oxidation, *Proc. Combust. Inst.*, *30*(1), 775–783.

Mahesh, K., G. Constantinescu, and P. Moin (2004), A numerical method for large-eddy simulation in complex geometries, *Journal of Computational Physics*, *197*, 215–240.

Marchisio, D. L., and R. O. Fox (2005), Solution of population balance equations using the direct quadrature method of moments, *J. Aerosol Sci.*, *36*, 43–73.

Marchisio, D. L., and R. O. Fox (2013), *Computational models for polydisperse particulate and multiphase systems*, Cambridge University Press.

Mare, F. D., W. P. Jones, and K. R. Menzies (2004), Large eddy simulation of a model gas turbine combustor, *Combust. Flame*, *137*(3), 278–294.

Masi, E., J. Bellan, K. G. , and N. a. Okong'o (2013), Multi-species turbulent mixing under supercritical-pressure conditions: modelling, direct numerical simulation and analysis revealing species spinodal decomposition, *Journal of Fluid Mechanics*, *721*, 578–626.

Mayer, W., J. Telaar, R. Branam, G. Schneider, and J. Hussong (2003), Raman measurements of cryogenic injection at supercritical pressure, *Heat and Mass Transfer/Waerme- und Stoffuebertragung*, *39*(8-9), 709–719.

McClung, A., K. Brun, and L. Chordia (2014), Technical and economic evaluation of supercritical oxy-combustion for power generation, *The 4th International Symposium - Supercritical CO2 Power Cycles*, (1), 1–5.

McCrain, L. L., and W. L. Roberts (2005), Measurements of the soot volume field in laminar diffusion flames at elevated pressures, *Combust. Flame*, *140*, 60–69.

McGraw, R. (1997), Description of aerosol dynamics by the quadrature method of moments, *Aerosol Science and Technology*, *27*(2), 255–265.

Mebel, A., M. Lin, T. Yu, and K. Morokuma (1997), Theoretical study of potential energy surface and thermal rate constants for the c6h5+ h2 and c6h6+ h reactions, *The Journal of Physical Chemistry A*, *101*(17), 3189–3196.

Metcalfe, W. K., S. M. Burke, S. S. Ahmed, and H. J. Curran (2013), A hierarchical and comparative kinetic modeling study of c1- c2 hydrocarbon and oxygenated fuels, *Int. J. Chem. Kinetics*, *45*(10), 638–675.

Moin, P., K. Squires, W. Cabot, and S. Lee (1991), A dynamic subgrid-scale model for compressible turbulence and scalar transport, *Physics of Fluids A*, *3*, 2746–2757.

Morinishi, Y. (2010), Skew-symmetric form of convective terms and fully conservative finite difference schemes for variable density low-mach number flows, *Journal of Computational Physics*, *229*, 276–300.

Morinishi, Y., T. S. Lund, O. V. Vasilyev, and P. Moin (1998), Fully conservative higher order finite difference schemes for incompressible flow, *Journal of Computational Physics*, *143*(1), 90–124.

Moureau, V., P. Minot, H. Pitsch, and C. Berat (2007), A ghost-fluid method for large-eddy simulations of premixed combustion in complex geometries, *Journal of Computational Physics*, *221*(2), 600–614, doi:10.1016/j.jcp.2006.06.031.

Mueller, M. E. (2012), Large eddy simulation of soot evolution in turbulent reacting flows, Ph.D. thesis, Stanford University.

Mueller, M. E., and H. Pitsch (2012), LES models for sooting turbulent nonpremixed flames, *Combust. Flame*, *159*, 2166–2180.

Mueller, M. E., and H. Pitsch (2013), Large eddy simulation of soot evolution in an aircraft combustor, *Physics of Fluids*, *25*.

Mueller, M. E., and V. Raman (2014), Effects of turbulent combustion modeling errors on soot evolution in a turbulent nonpremixed jet flame, *Combust. Flame*, *161*(7), 1842–1848.

Mueller, M. E., G. Blanquart, and H. Pitsch (2009), Hybrid method of moments for modeling soot formation and growth, *Combust. Flame*, *156*, 1143–1155.

Mueller, M. E., Q. N. Chan, N. H. Qamar, B. B. Dally, H. Pitsch, Z. T. Alwahabi, and G. J. Nathan (2013), Experimental and computational study of soot evolution in a turbulent nonpremixed bluff body ethylene flame, *Combust. Flame*, *160*(7), 1298–1309.

Mueller, M. E., G. Blanquart, and H. Pitsch (2009), A joint volume-surface model of soot aggregation with the method of moments, *Proc. Combust. Inst.*, *32*, 785–792.

Narayanaswamy, K., G. Blanquart, and H. Pitsch (2010), A consistent chemical mechanism for oxidation of substituted aromatic species, *Combust. Flame*, *157*(10), 1879–1898.

Neoh, K., J. Howard, and A. Sarofim (1981), Soot oxidation in flames, in *Particulate Carbon*, pp. 261–282, Springer.

Oefelein, J. C., and V. Yang (1998), Modeling High-Pressure Mixing and Combustion Processes in Liquid Rocket Engines, *Journal of Propulsion and Power*, *14*(5), 843–857.

Pepiot-Desjardins, P., and H. Pitsch (2008), An efficient error-propagation-based reduction method for large chemical kinetic mechanisms, *Combust. Flame*, *154*(1), 67–81.

Peters, N. (1984), Laminar diffusion flamelet models in non-premixed turbulent combustion, *Progress in energy and combustion science*, *10*(3), 319–339.

Peters, N. (2000), *Turbulent Combustion*, Cambridge University Press.

Pierce, C. D. (2001), Progress-variable approach for large-eddy simulation of turbulence combustion, Ph.D. thesis, Stanford University.

Pierce, C. D., and P. Moin (2004), Progress-variable approach for large-eddy simulation of non-premixed turbulent combustion, *J. Fluid Mech*, *504*, 73–97.

Pitsch, H. (1998), FlameMaster: A C++ computer program for 0-d and 1-d laminar flame calculations, RWTH Aachen.

Pitsch, H. (2006), Large-eddy simulation of turbulent combustion, *Annual Review of Fluid Mechanics*, *38*, 453–482.

Poinsot, T., and D. Veynante (2001), *Theoretical and Numerical Combustion*, R. T. Edwards, Philadelphia, USA.

Pope, S. B. (1985), PDF methods for turbulent reactive flows, *Prog. Energ. Combust. Sci.*, *11*, 119.

Pope, S. B. (2001), Turbulent flows.

Pope, S. B. (2004), Ten questions concerning the large-eddy simulation of turbulent flows, *New Journal of Physics*, *6*(1), 35.

Qamar, N., Z. Alwahabi, Q. Chan, G. Nathan, D. Roekaerts, and K. King (2009), Soot volume fraction in a piloted turbulent jet non-premixed flame of natural gas, *Combust. Flame*, *156*(7), 1339–1347.

Raman, V., and R. O. Fox (2016), Modeling of fine-particle formation in turbulent flames, *Ann. Rev. Fluid Mech.*, *48*, 159–190.

Raman, V., and H. Pitsch (2005), Large-eddy simulation of a bluff-body stabilized non-premixed flame using a recursive-refinement procedure, *Combust. Flame*, *142*(4), 329–347.

Raman, V., and H. Pitsch (2006), A consistent LES/filtered-density function formulation for the simulation of turbulent flames with detailed chemistry, *Proc. Combust. Inst.*, *31*, 1711–1719.

Raman, V., H. Pitsch, and R. O. Fox (2005), Hybrid large-eddy simulation/Lagrangian filtered-density-function approach for simulating turbulent combustion, *Combustion and Flame*, *143*, 56–78.

Reid, R., J. Prausnitz, and B. Polling (1987), Molecular theory of gases and liquids.

Ren, Z., and S. B. Pope (2004), An investigation of the performance of turbulent mixing models, *Combust. Flame*, *136*(1), 208–216.

Sagaut, P. (2006), *Large eddy simulation for incompressible flows: an introduction*, Springer Science & Business Media.

Salenbauch, S., A. Cuoci, A. Frassoldati, C. Saggese, T. Faravelli, and C. Hasse (2015), Modeling soot formation in premixed flames using an extended conditional quadrature method of moments, *Combust. Flame*, *162*(6), 2529–2543.

Schuetz, C. A., and M. Frenklach (2002), Nucleation of soot: molecular dynamics simulations of pyrene dimerization, *Proceedings of the Combustion Institute*, *29*(2), 2307–2314.

Selvaraj, P., et al. (2016), A computational study of ethylene–air sooting flames: Effects of large polycyclic aromatic hydrocarbons, *Combust. Flame*, *163*, 427–436.

Sewerin, F., and S. Rigopoulos (2017), An les-pbe-pdf approach for modeling particle formation in turbulent reacting flows, *Phys. Fluids*, *29*(10), 105,105.

Smith, G. P., et al. (2012), Grimech 3.0 reaction mechanism, berkeley.

Smooke, M., M. Long, B. Connelly, M. Colket, and R. Hall (2005), Soot formation in laminar diffusion flames, *Combustion and Flame*, *143*(4), 613–628.

Smyth, K. C., J. H. Miller, R. C. Dorfman, W. G. Mallard, and R. J. Santoro (1985), Soot inception in a methane/air diffusion flame as characterized by detailed species profiles, *Combustion and flame*, *62*(2), 157–181.

Stöhr, M., R. Sadanandan, and W. Meier (2009), Experimental study of unsteady flame structures of an oscillating swirl flame in a gas turbine model combustor, *Proc. Combust. Inst.*, *32*(2), 2925–2932.

Subramaniam, S., and S. Pope (1998), A mixing model for turbulent reactive flows based on euclidean minimum spanning trees, *Combustion and Flame*, *115*(4), 487–514.

Sung, Y. (2011), Large eddy simulation of TiO_2 nanoparticle evolution in turbulent flames, Ph.D. thesis, The University of Texas at Austin.

Sung, Y., V. Raman, H. Koo, M. Mehta, and R. O. Fox (2014), Large-eddy simulation modeling of turbulent flame synthesis of titania nanoparticles using a bivariate particle description, *AIChE Journal*, *60*(2), 459–472.

Tang, Y., H. Koo, C. Lietz, and V. Raman (2016), Numerical study on flame stabilization mechanism of a multi-jet burner with les flamelet approach, in *54th AIAA Aerospace Sciences Meeting*, 2016-1395.

Tesner, P., T. Smegiriova, and V. Knorre (1971), Kinetics of dispersed carbon formation, *Combustion and flame*, *17*(2), 253–260.

Tokmakov, I., and M. Lin (2004), Combined quantum chemical/rrkm-me computational study of the phenyl+ ethylene, vinyl+ benzene, and h+ styrene reactions, *The Journal of Physical Chemistry A*, *108*(45), 9697–9714.

UNION, P., et al. (2008), Directive 2008/50/ec of the european parliament and of the council of 21 may 2008 on ambient air quality and cleaner air for europe, *Official Journal of the European Union.*

Vandsburger, U., I. Kennedy, and I. Glassman (1984), Sooting counterflow diffusion flames with varying oxygen index, *Combustion Science and Technology*, *39*(1-6), 263–285.

Vargas, A. M., and Ö. L. Gülder (2017), Pressure dependence of primary soot particle size determined using thermophoretic sampling in laminar methane-air diffusion flames, *Proc. Combust. Inst.*, *36*(1), 975–984.

Von Smoluchowski, M. (1917), M. von smoluchowski, z. phys. chem. 92, 129 (1917)., *Z. Phys. Chem.*, *92*, 129.

Wall, C., B. Boersma, and P. Moin (2000), An evaluation of the assumed beta probability density function sub-grid scale model for large eddy simulation of nonpremixed turbulent combustion with heat release, *Physics of Fluids*, *7*, 2522.

Wang, H. (2011), Formation of nascent soot and other condensed-phase materials in flames, *Proc. Combust. Inst.*, *33*(1), 41–67.

Wang, H., and M. Frenklach (1997), A detailed kinetic modeling study of aromatics formation in laminar premixed acetylene and ethylene flames, *Combust. flame*, *110*(1), 173–221.

Wang, H., X. You, A. V. Joshi, S. G. Davis, A. Laskin, F. Egolfopoulos, C. K. Law, and U. M. Version II (2007), High-temperature combustion reaction model of h2, *Tech. rep.*, CO/C1-C4 Compounds. http://ignis. usc. edu/USC_Mech_II. htm.

Wick, A., T.-T. Nguyen, F. Laurent, R. O. Fox, and H. Pitsch (2017a), Modeling soot oxidation with the extended quadrature method of moments, *Proceedings of the Combustion Institute*, *36*(1), 789–797.

Wick, A., F. Priesack, and H. Pitsch (2017b), Large-eddy simulation and detailed modeling of soot evolution in a model aero engine combustor, in *ASME Turbo Expo 2017: Turbomachinery Technical Conference and Exposition*, pp. 1–10, American Society of Mechanical Engineers.

Xu, F., P. Sunderland, and G. Faeth (1997), Soot formation in laminar premixed ethylene/air flames at atmospheric pressure, *Combust. Flame*, *108*(4), 471–493.

Xuan, Y., and G. Blanquart (2015), Effects of aromatic chemistry-turbulence interactions on soot formation in a turbulent non-premixed flame, *Proc. Combust. Inst.*, *35*(2), 1911–1919.

Yang, V. (2000), Modeling of supercritical vaporization, mixing, and combustion processes in liquid-fueled propulsion systems, *Proceedings of the Combustion Institute*, *28*(1), 925–941.

Yoo, J. Y. (2013), The turbulent flows of supercritical fluids with heat transfer, *Annual Review of Fluid Mechanics*, *45*(1), 495–525.

Yuan, C., and R. O. Fox (2011), Conditional quadrature method of moments for kinetic equations, *J. Comput. Phys.*, *230*(22), 8216–8246.

Yuan, C., F. Laurent, and R. Fox (2012), An extended quadrature method of moments for population balance equations, *J. Aerosol Sci.*, *51*, 1–23.

Zhang, H. R., E. G. Eddings, and A. F. Sarofim (2007), Criteria for selection of components for surrogates of natural gas and transportation fuels, *Proceedings of the Combustion Institute*, *31*(1), 401–409.

Zhang, J., C. R. Shaddix, and R. W. Schefer (2011), Design of model-friendly turbulent non-premixed jet burners for c2+ hydrocarbon fuels, *Review of Scientific Instruments*, *82*(7), 074,101.

Zhao, B., Z. Yang, Z. Li, M. V. Johnston, and H. Wang (2005), Particle size distribution function of incipient soot in laminar premixed ethylene flames: effect of flame temperature, *Proceedings of the Combustion Institute*, *30*(1), 1441–1448.

Zucca, A., D. L. Marchisio, M. Vanni, and A. A. Barresi (2007), Validation of bivariate dqmom for nanoparticle processes simulation, *AIChE Journal*, *53*(4), 918–931.